Fracture strength of micro- and nano-scale silicon components

Frank W. DelRio, Robert F. Cook, and Brad L. Boyce

Articles you may be interested in

Dopant-induced stress in microfabricated silicon devices
J. Appl. Phys. **114**, 043512 (2013); 10.1063/1.4816568

Effect of surface stress on the stiffness of micro/nanocantilevers: Nanowire elastic modulus measured by nano-scale tensile and vibrational techniques
J. Appl. Phys. **113**, 013508 (2013); 10.1063/1.4772649

Effects of anisotropic elasticity on stress concentration in micro mechanical structures fabricated on (001) single-crystal silicon films
J. Appl. Phys. **105**, 093524 (2009); 10.1063/1.3124368

Elasticity, strength, and toughness of single crystal silicon carbide, ultrananocrystalline diamond, and hydrogen-free tetrahedral amorphous carbon
Appl. Phys. Lett. **89**, 073111 (2006); 10.1063/1.2336220

Fracture toughness of polycrystalline silicon carbide thin films
Appl. Phys. Lett. **86**, 071920 (2005); 10.1063/1.1864246

CrossMark
click for updates

APPLIED PHYSICS REVIEWS

Fracture strength of micro- and nano-scale silicon components

Frank W. DelRio,[1,a)] Robert F. Cook,[2,b)] and Brad L. Boyce[3,c)]
[1]*Applied Chemicals and Materials Division, Material Measurement Laboratory,
National Institute of Standards and Technology, Boulder, Colorado 80305, USA*
[2]*Materials Measurement Science Division, Material Measurement Laboratory, National Institute of Standards
and Technology, Gaithersburg, Maryland 20899, USA*
[3]*Materials Science and Engineering Center, Sandia National Laboratories, Albuquerque, New Mexico 87185,
USA*

Silicon devices are ubiquitous in many micro- and nano-scale technological applications, most notably microelectronics and microelectromechanical systems (MEMS). Despite their widespread usage, however, issues related to uncertain mechanical reliability remain a major factor inhibiting the further advancement of device commercialization. In particular, reliability issues related to the fracture of MEMS components have become increasingly important given continued reductions in critical feature sizes coupled with recent escalations in both MEMS device actuation forces and harsh usage conditions. In this review, the fracture strength of micro- and nano-scale silicon components in the context of MEMS is considered. An overview of the crystal structure and elastic and fracture properties of both single-crystal silicon (SCS) and polycrystalline silicon (polysilicon) is presented. Experimental methods for the deposition of SCS and polysilicon films, fabrication of fracture-strength test components, and analysis of strength data are also summarized. SCS and polysilicon fracture strength results as a function of processing conditions, component size and geometry, and test temperature, environment, and loading rate are then surveyed and analyzed to form overarching processing-structure-property-performance relationships. Future studies are suggested to advance our current view of these relationships and their impacts on the manufacturing yield, device performance, and operational reliability of micro- and nano-scale silicon devices. [http://dx.doi.org/10.1063/1.4919540]

TABLE OF CONTENTS

a)frank.delrio@nist.gov
b)robert.cook@nist.gov
c)blboyce@sandia.gov

I. INTRODUCTION

Silicon (Si) microfabrication techniques, derived from the microelectronics industry, have enabled the development and commercialization of microelectromechanical systems (MEMS). MEMS have been employed in a wide range of micro-scale applications, including the transmission and conversion of electrical and mechanical energy, in particular, but also optical, chemical, and thermal energy. An example of an advanced MEMS device is shown in Fig. 1, which is a scanning electron microscope (SEM) image of a microchain drive fabricated in polycrystalline silicon (polysilicon). Power for the drive originates from electrical sources that use another MEMS device (not visible in the image) to rotate a small gear (visible in top left of the image) that provides power to the microchain drive via larger gears. The drive is clearly a mechanical device, consisting of components under common engineering loading modes: bars in tension (e.g., the links of the chain), beams in bending (the spurs of the gears), columns in compression (the spokes of the gears),
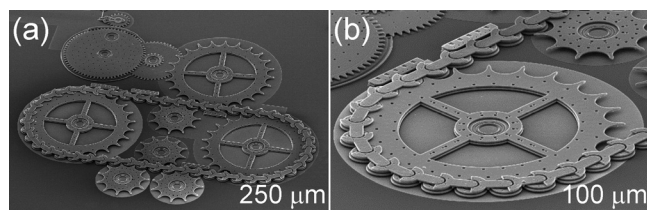

FIG. 1. SEM images of a microchain drive fabricated with the SUMMiT V process. The drive is a mechanical MEMS device, consisting of components under common engineering loading modes. The reliability of the device depends on these components performing as required over the device lifetime. Courtesy of Sandia National Laboratories, SUMMiT™ Technologies, www.mems.sandia.gov.

and shafts in torsion (the axles for the gears), along with small-scale contacts and friction at the contacting, moving interfaces between the components (between the gear spurs and chain links, or the gear hubs and axles). The reliability of this device clearly depends on these components performing as required over the device lifetime. Reliability is taken here as a time-related, extensive performance measure of a manufactured component: For the microchain drive, the performance measure might be a minimum delivered torque, whereas for the drive components, it might be the minimum load to be supported during operation. In the latter case, the performance measure can be expressed in terms of *intensive* quantities such that reliable device operation requires the *strengths* of the components to exceed the (perhaps variable) *stress* applied to the component during the device lifetime. It is the strengths of micro- and nano-scale single-crystal silicon (SCS) and polysilicon components that are the focus of this review.

At room temperature, both SCS and polysilicon are brittle and thus the strengths of such micro- and nano-scale components are brittle *fracture* strengths (i.e., all deformation is elastic prior to and during fracture); strength here is taken to be the applied stress required to propagate a crack completely across a component so as to reduce the load-carrying capacity to zero. In broad terms, such strengths depend on both the resistance of the component material to fracture *and* the size and nature of flaws in the component from which cracks can grow. The first of these depends on the structure and microstructure of the material and thus in this case is determined by the selected crystal orientation for SCS and the processing method for polysilicon. The second depends on the component fabrication method and the mechanical environment. These aspects can be used to engineer component reliability by manipulating one or both sides of the applied stress-component strength relation: (i) expose components only to small stresses, by either limiting the mechanical environment to impose small loads or increasing the component scale to have large sections (stress is proportional to load/cross-sectional area); (ii) form components with large strengths, by either modifying the material to have large fracture resistance or modifying the flaws to have weak propensity to cracking (strength is proportional to fracture resistance/flaw potency). The vast majority of commercial MEMS devices (e.g., accelerometers, pressure sensors, high brightness display mirror arrays) have pursued the small applied stress route to reliability, with limited deformation and no, or little, contact of components during device operation. This route is ruled out for achieving reliability and hence commercial success for MEMS devices such as those shown in Fig. 1. The entire point of such devices is to generate large deformations via linked mechanisms to create useful large torques or loads at small scales; there is no choice but for the included components to support large stresses. Hence, for devices such as those in Fig. 1, reliability can only be achieved via the large component strength route. Such a route is characterized by engineering control of the structure of components by the selection of processing variables and use of scientific knowledge of the linkages between structure and strength.
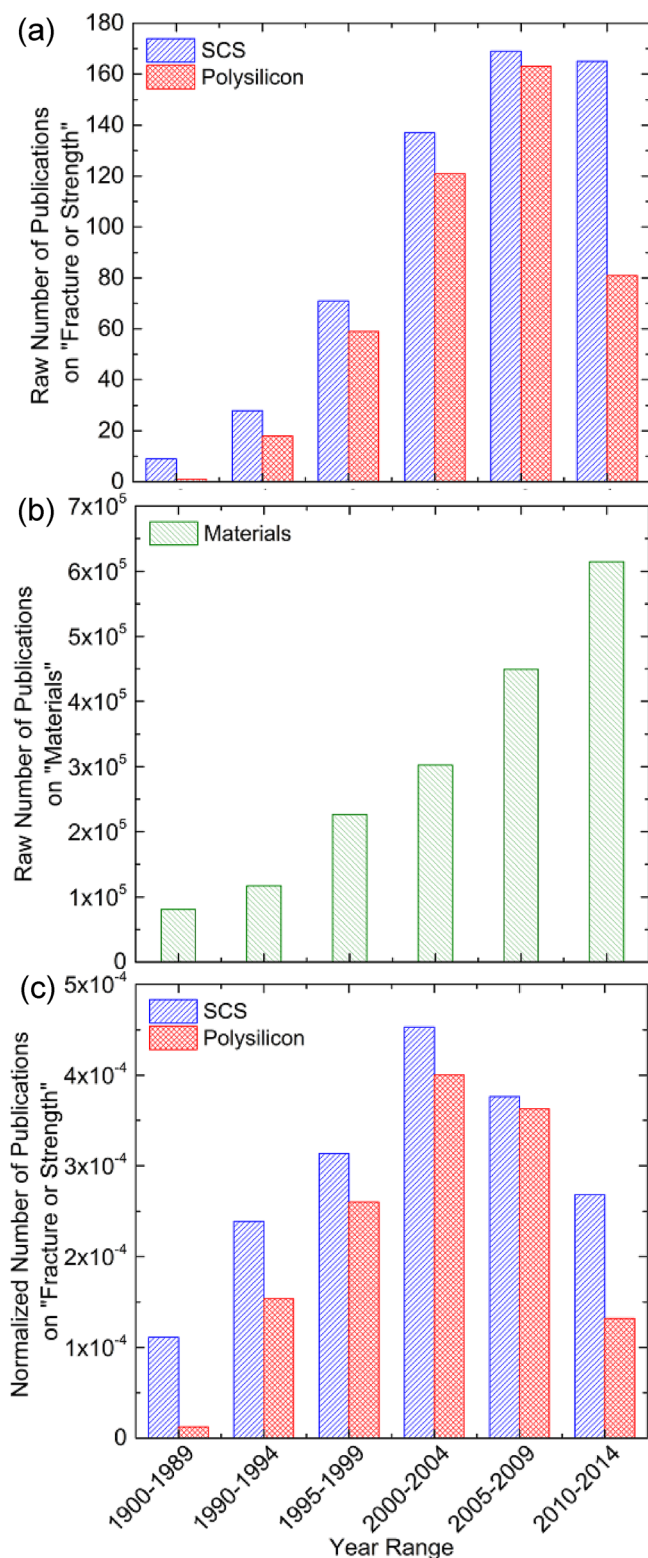
FIG. 2. Raw number of journal publications on the topics of (a) SCS and polysilicon "fracture" or "strength" and (b) "materials." The normalized number of journal publications in (c) indicates that the focus of the materials community begun to shift away from fracture and strength of Si beginning about 2000, when the relative number peaked. Data from Thompson Reuters Web of Science™.

This review will focus on the fracture strengths of micro- and nano-scale components as they are used in MEMS or nanoelectromechanical systems (NEMS). The

review will largely exclude microelectronic devices with their millimeter-scale Si dies, but will include nano-scale wires and whiskers as (i) the natural end point for continued decreased dimensions in MEMS, NEMS, and microelectronic devices and (ii) have obvious future applications in such devices. It will also be seen that this restriction is based on a physical difference: The fracture strengths of these larger-scale devices are usually controlled by the *propagation* of well-defined cracks generated at micro-scale contact events with well-defined plastic deformation zones. Such contacts occur during whole device fabrication (e.g., in Si wafer grinding and dicing), and the consequent strengths and strength-controlling flaws have been previously covered in a review by Cook.[1] By contrast, the strengths of the micro- and nano-scale components under consideration here are controlled by either surface features intrinsic to the fabrication of the material or the component, such as grain-boundary grooves or etch pits (e.g., in thin-film growth or micromachining, respectively), or nano-scale contact events with limited plastic deformation (e.g., at contacting interfaces during component actuation). In both of these cases, the strength-controlling flaw often has only nascent cracks and strength is associated with crack *initiation*. Once cracks have been initiated in Si under stress, they are typically in an over-driven state and propagate unstably leading to component failure.

The review will also strictly consider "strength" behavior, that is, in which a component is exposed only to monotonically increasing applied loading as the condition for crack extension and component failure. Hence, detailed consideration will not be made of "fatigue" loading, in which material properties degrade and a crack may extend prior to component failure. What is considered are failure conditions in which the component is exposed to variations in applied loading prior to the condition for crack extension and component failure. In this case, component strength plays a central role in determining failure or otherwise during device operation and it is the applied loading kinetics or spectrum that determines component lifetime and lifetime distribution. It is this spectrum that is most important in determining MEMS and NEMS reliability and a large motivation for considerations of micro- and nano-scale strength and strength distributions.

In many ways, Petersen's seminal 1982 article on "Silicon as a mechanical material,"[2] now cited over 3000 times, empowered a generation of engineers to design structural devices with a material that had rarely been used in such a capacity before. In that article, a somewhat simplistic and misleading comparison is made between the mechanical properties of Si and other more conventional structural materials such as steel. Specifically, the concept of "strength" was used in a deterministic sense, with little conveyance of the implications of a rather small Si fracture resistance and the intolerance for processing-induced flaws with the ensuing stochastic nature of failure. These issues will be seen to be central in this review. The broader historical context of this review, and the progress in materials science and engineering required to generate reliable devices such as that in Fig. 1 through strength control, may be observed in the history of

publications on this subject. Figure 2 shows histograms of the number of publications taken from an abstract and citation database for "fracture" or "strength" of SCS and polysilicon, along with that for "materials" since 1900. Figure 2(a) shows that there was a significant increase in the number of publications regarding fracture or strength of Si beginning about 1990. At that time, the microelectronics industry was moving towards significantly larger wafers and dies, with attendant focus on greater numbers of fracture-related fabrication yield limitations, and microelectronics-based fabrication methods were beginning to be implemented in the nascent MEMS industry. By 2009, the number of publications regarding fracture or strength of Si had increased by about a factor of ten, at which time the number began to decline. Conversely, publications regarding materials increased substantially over that same time period, by about a factor of five, Fig. 2(b), albeit in much greater numbers. As a consequence, the focus of the materials community, as measured by the relative number of (fracture or strength)/materials publications, begun to shift away from fracture and strength of Si beginning about 2000, when the relative number peaked, Fig. 2(c). As will be seen in the following review, the peak indicates a maturation of the field of Si strength in terms of relating the underpinning material elastic and fracture properties via the fundamentals of solid and fracture mechanics to the atomistic structure, and in terms of the emergence of consistent, widely accessible foundries available for MEMS. Unless otherwise noted, the experimental uncertainties throughout this review are one standard deviation of the population mean.

II. FRACTURE MECHANICS AND PROPERTIES OVERVIEW

This section reviews measurements of the fundamental fracture properties of SCS and polysilicon materials that underlie the strength of SCS and polysilicon components. The section also provides the analytical fracture mechanics framework required to interpret these strengths. The section builds in a sequential manner, starting with material properties and ending with component behavior. Brief overviews of the structure and elastic properties of Si are given, before consideration of fracture energy and toughness based on the structural and elastic characteristics (a review of the elastic properties of Si is given in the Appendix). Measurements of SCS and polysilicon fracture energy and toughness are then reviewed, followed by the fracture mechanics required to relate component strength to material toughness via the size and nature of the strength-controlling flaw. Finally, analyses commonly used to characterize strength distributions of Si components are briefly reviewed.

A. Crystal structure and polysilicon microstructure

Under ambient temperatures and pressures, SCS exhibits a diamond cubic crystal structure, consisting of a face-centered cubic lattice with a two-atom basis of (0, 0, 0) and (1/4, 1/4, 1/4).[3] The atoms are four-fold coordinated into hybridized sp^3-bonded regular tetrahedrons with the three-fold tetrahedral axes parallel to $\langle 111 \rangle$ directions in the cubic

lattice. The {111} planes are close packed with an interatomic spacing of 0.235 nm. Figure 3(a) shows a schematic diagram of the crystal structure set in a $[110] - [\bar{1}10] - [001]$ tetragonal sub-cell of the cubic lattice. The tetragonal axes in Fig. 3(a) are more useful for consideration of deformation and fracture properties than the conventional $\langle 100 \rangle$ cubic cell coordinates as the $(\bar{1}10)$ plane contains the four primary low-index directions, [001], [112], [111], and [110], and the $[\bar{1}10]$ direction is a zone axis for the (001), (111), and (110) planes. As will be seen, these symmetry directions and planes exhibit extrema in elastic and fracture properties. The relationship between the tetragonal sub-cell and the cubic cell is shown in Fig. 3(b).

Under typical processing conditions, polysilicon used in micro- and nano-structures is formed as a thin film with a columnar grain structure perpendicular to the plane of the
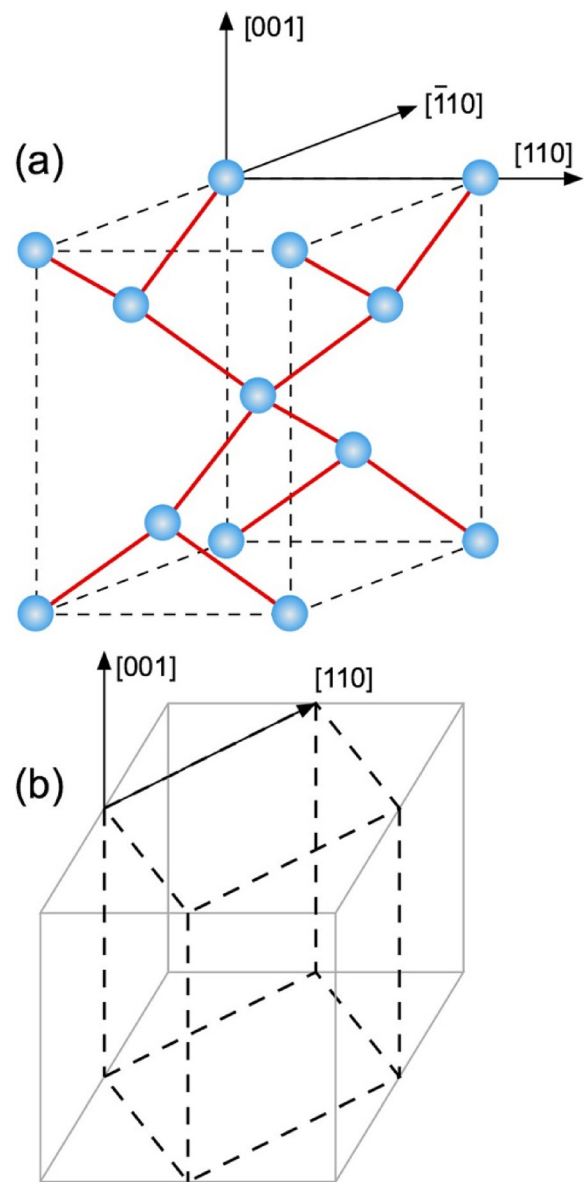

FIG. 3. (a) Schematic diagram of the crystal structure of Si set in a $[110] - [\bar{1}10] - [001]$ tetragonal sub-cell of the cubic lattice; atom positions are shown as spheres and bonds as solid lines. (b) Schematic diagram of the crystal structure of Si, showing the relationship between the tetragonal sub-cell and the cubic cell.
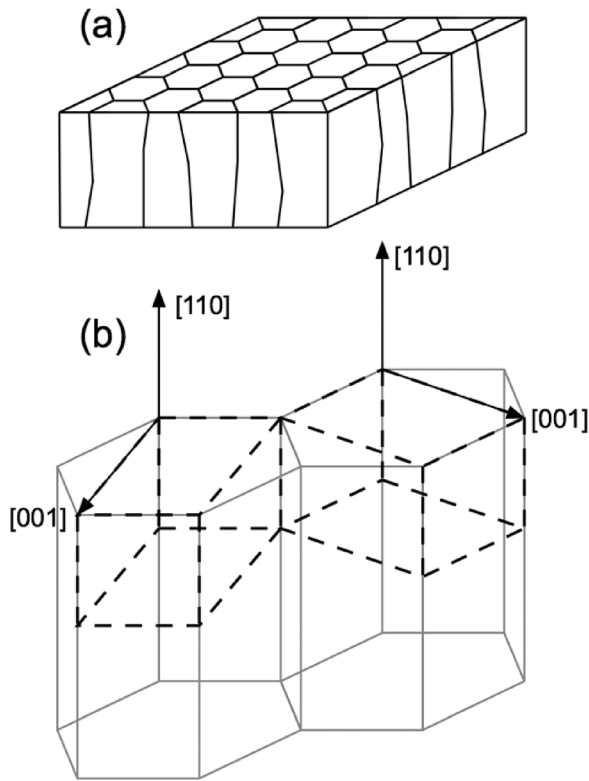
FIG. 4. (a) Schematic diagram of a thin film of polysilicon, with a columnar grain structure perpendicular to the plane of the film. (b) In some cases, the Si crystals forming the columnar grains are preferentially aligned such that SCS [110] directions are parallel to the column axes with random rotation of crystal axes around these directions (shown). In other cases, although the grains are columnar, there is no preferential crystal alignment (not shown).

film,[4–7] shown in the schematic diagram of Fig. 4(a). In some cases,[4,5] the Si crystals forming the columnar grains are preferentially aligned such that SCS [110] directions are parallel to the column axes with random rotation of crystal axes around these directions. The relationship between the tetragonal sub-cell and the columnar grains in this case is shown in the schematic diagram of Fig. 4(b). In other cases, although the grains are columnar, there is no preferential crystal alignment.[6,7]

B. Elastic properties

The elastic properties of SCS reflect the underlying cubic anisotropy of the bonding with three independent values in the elastic compliance matrix:[8] $s_{11} = 7.68$ TPa^{-1}, $s_{12} = -2.14$ TPa^{-1}, and $s_{44} = 12.56$ TPa^{-1}, as measured first by McSkimin et al. and later by Hall.[9–12] These values may be used to calculate the variation of elastic constants as a function of direction in the crystal, and in particular, the variation of Young's modulus E, relating longitudinal stress to normal strain, and Poisson's ratio ν, relating (negative) transverse strain to normal strain under longitudinal stress conditions. Figure 5(a) shows the orientation variation in E for SCS in the $(\bar{1}10)$ plane and Fig. 5(b) does likewise for ν, using equations given in the Appendix: the two-fold symmetry in this plane is obvious. E varies from a maximum of $E_{[111]} = 187$ GPa in the $\langle 111 \rangle$ directions to a minimum of
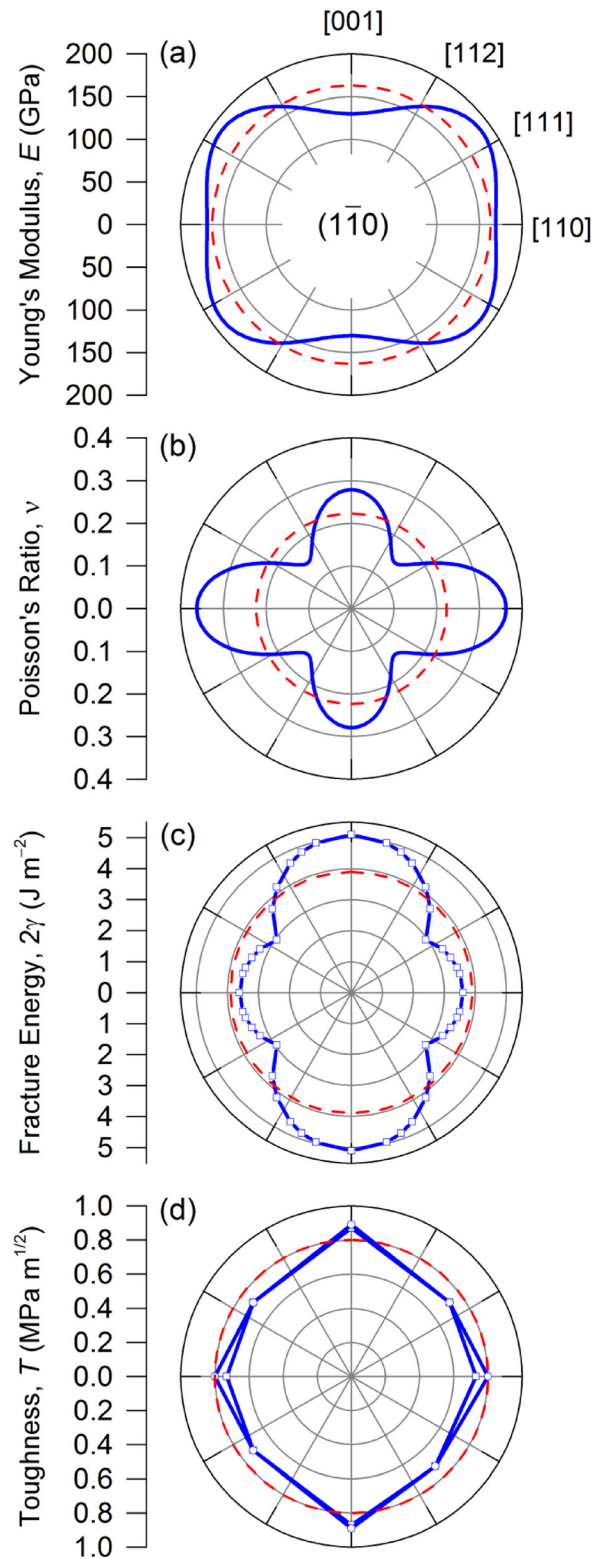
FIG. 5. (a) Young's modulus, (b) Poisson's ratio, (c) fracture energy, and (d) toughness of Si projected onto the $(1\bar{1}0)$ plane. The solid lines represent the values for SCS as a function of crystallographic orientation, whereas the dashed lines represent the values for polysilicon assuming a random, uniform, three-dimensional distribution of grain orientations.

$E_{[100]} = 130$ GPa in the $\langle 100 \rangle$ directions, with an intermediate value of $E_{[110]} = 169$ GPa in the $\langle 110 \rangle$ directions. The variation in ν is somewhat reversed, from a maximum of 0.362 in the $\langle 110 \rangle$ directions to a minimum of 0.167 in the

$\langle 111 \rangle$ directions, with an intermediate value of 0.279 in the $\langle 100 \rangle$ directions. As also shown in the Appendix, the compliance values provide a means of estimating the elastic constants of an isotropic polycrystal, $E_{(poly)} = 163$ GPa and $\nu_{(poly)} = 0.223$, and these are shown as the circular dashed lines in Figs. 5(a) and 5(b). A [110] textured polycrystalline film has an out-of-plane modulus $E_{[110]}$ and in-plane modulus and Poisson's ratio given by the angular averages of the variations shown in Figs. 5(a) and 5(b): $\bar{E}_{(110)} = 165$ GPa and $\bar{\nu}_{(110)} = 0.24$.

As reviewed in the Appendix, the engineering elastic constants, E and ν, of small-scale SCS and polysilicon components, measured under quasi-static deformation conditions, are in agreement with predictions from crystallography and microstructural averaging using elements of the elastic compliance tensor s_{ij} measured under dynamic ultrasonic conditions. For SCS, considering all orientations and test geometries, measurements of E and ν vary between 85% and 110% of the predicted values. Importantly, there is considerable consensus that the most common loading configuration for SCS, tension in [110], exhibits an $E_{[110]}$ very close to the predicted value of 169 GPa. The most precise measurements by Banks-Sills et al., using direct interferometric strain measurements,[13] give this value with an uncertainty of about $\pm 2\%$, comparable to the uncertainty inherent in the predictions from the s_{ij} values. For polysilicon, considering all microstructures and test geometries, measurements of E and ν vary between 85% and 115% of the predicted values, with most measurements of $E_{(poly)}$ or $\bar{E}_{(110)}$ within 5% of the predicted values of 163 GPa and 165 GPa, respectively. Once again, the most precise measurements using direct digital image correlation (DIC) strain measurements by Cho and Chasiotis give the $\bar{E}_{(110)}$ value with an uncertainty of $\pm 4\%$, just slightly greater than the uncertainty inherent in the s_{ij} values and the polycrystalline averaging process.[14]

Establishing agreement between the predicted and measured elastic properties in consideration of the strength of small-scale structures is critically important for several reasons: First, the agreement implies that there are negligible effects associated with the large surface area/volume ratios of such structures and the etching during lithographic formation of the structures does not introduce a significant surface stress; the Si can be treated as "bulk." Second, the elastic constants can be used to predict stress and strain fields in SCS and polysilicon components containing cracks, and, importantly, as shown in Sec. II C, are required to make connection between the energy flux required to break bonds at a crack tip and the work performed by loads applied externally to the boundaries of a component. Third, it might be argued that knowledge of elastic properties is not required for strength measurements, as stress applied to a sample, and hence sample failure stress or strength is calculable from load and geometry with no knowledge of modulus required. However, accurate measurements of modulus in the same test configurations as used in strength tests enable verification, as shown in Secs. IV and V, that the loads are being applied to samples in the assumed manner, that is, that sample and test configuration and alignment are correct.

C. Fracture properties

1. Crystallographic effects on SCS fracture energy

As with most crystal structures, that of SCS affects fracture anisotropy in two ways: (i) The structure determines the areal density of Si-Si bonds that must be broken in order to form a fracture surface of a given orientation and thereby determines the fracture energy (density), $2\gamma_{(hkl)}$ (energy/area), for a given (hkl) plane. (ii) The structure determines the elastic anisotropy of Si and thereby determines the crack driving force, $G_{(hkl)[uvw]}$ (the mechanical energy release rate, energy/area), for a given crack-front orientation $[uvw]$ in an (hkl) plane.

For brittle materials, such as Si, the fracture process is well described by the propagation of a "sharp" crack, such that the bond rupture process is localized to a zone of a few atomic bonds at a well-defined crack tip. Ahead of the crack tip zone, the body of the material is deformed elastically and well described by linear elasticity. Behind the zone, the fracture surfaces consist of arrays of ruptured "dangling" bonds (i.e., with no long-range surface re-construction or reaction with environmental species), well described by a continuum surface energy—the fracture energy is then just twice the surface energy. The fracture energy density is then the product of the energy/bond u_B and the bonds broken/area n_A for a given fracture plane, a calculation first made for diamond by Harkins.[15] For an (hkl) plane in Si, this gives[16]

$$2\gamma_{(hkl)} = u_B n_A = u_B \frac{4\max(h,k,l)}{(h^2 + k^2 + l^2)^{1/2}} \frac{1}{a_0^2}, \qquad (1)$$

where a_0 is the diamond-cubic lattice constant of Si. This quantity is a minimum for the (111) plane and using $u_B = 226$ kJ mol^{-1} and $a_0 = 0.543$ nm for Si[17] gives $2\gamma_{(111)} = 2.94$ J m^{-2} (compared to 11.3 J m^{-2} for diamond, which has greater bond energy and smaller lattice constant[15]). For (hkl) in the $[\bar{1}10]$ zone, the variation of fracture energy is

$$2\gamma_{(hkl)} = 2\gamma_{(111)}\max(h,l)\left(\frac{3}{2h^2 + l^2}\right)^{1/2} \qquad (2)$$

noting that planes in this zone are of the form (hhl).[1] The above variation is plotted as the open symbols in Fig. 5(c), recognizing that the angular variation is for fracture on planes perpendicular to the discrete directions indicated (the line is a guide to the eye). The fracture energy increases weakly to $2\gamma_{(110)} = (3/2)^{1/2} 2\gamma_{(111)} = 3.60$ J m^{-2} and more strongly to $2\gamma_{(100)} = (3)^{1/2} 2\gamma_{(111)} = 5.09$ J m^{-2}.

Experimental evidence in support of this view of the formation of fracture surfaces in Si and the associated fracture energy calculation comes from a diversity of physical sources and includes direct transmission electron microscopy (TEM) observations of cracks by Lawn et al., showing sharp tips and negligible deformation of the body material and crack faces;[18] electron paramagnetic resonance signals associated with localized electron states (the dangling bonds) that increase in proportion to crack area for fractured Si;[19] electrical measurements showing that resistivity across

cracks can reduce to zero as crack faces heal, in strong support of negligible fracture surface reconstruction;[20] mechanical grinding[16] and chemical etching[21] of Si spheres showing distinct tendencies to form surfaces in the order (111), (110), and (100), consistent with the above surface energy calculations; and a clear linear variation of (111) surface energies calculated as above with (brittle) semiconductor band gaps.[22] Supporting evidence from fracture modeling studies includes molecular statics calculations of (111) fracture in Si showing the dominance of the linear elastic continuum description for the crack-tip displacement field except for a very small (three atom) zone adjacent to the tip[23] and more recent molecular dynamics calculations[24,25] for fracture surfaces in [100], [110], and [111] zones showing excellent qualitative agreement with the variations of surface energy as in Fig. 5(c), although quantitatively the energy values were depressed about 20% from those given above and displayed non-monotonic fluctuations in surface energy with angle for planes close to the (111) orientation.

2. Crystallographic effects on SCS crack driving force

The picture that emerges from the above is that the brittle fracture surfaces of Si are well understood in terms of the formation mechanism (nano-scale rupture zone enclosed in a large linear elastic region) and subsequent excess surface energy densities (crystallography determines broken bonds/crack area). To make a connection with the work necessary to create the surfaces, performed at the external boundaries of a fracture system and involving the measurables of applied forces and displacements and specimen and crack dimensions, the elastic anisotropy of Si must be taken into account. The general expression for equilibrium of linear elastic fracture systems is $G = R$, where G is the mechanical energy release rate and R is fracture resistance.[26] R is given by $R = dU_S/dA$, where U_S is the fracture surface energy and A is the crack area, and hence for SCS, R is given by $2\gamma_{(hkl)}$ as above. G is given by

$$G = d(W - U_E)/dA, \qquad (3)$$

where W is the work performed by the external loading and U_E is the elastic energy of the system. W depends only on the external load and load-point displacement and has no material dependence, whereas U_E depends on the displacement (or stress or strain) field within the fracturing body and contains material dependence through the (potentially anisotropic) elastic properties in determining the resulting strain-energy density field. Hence, for a given W, U_E will, in general, depend on the orientations of the crack plane and propagation front and hence so will G.

In elastically isotropic materials, the connection between the external loading and the internal stress distribution is given by the Irwin relation[27]

$$G = K^2/E, \qquad (4)$$

where K is the stress-intensity factor (SIF), determined entirely by external boundary conditions (including the crack length) and E is the isotropic (plane-stress) Young's modulus.[26] For elastically anisotropic materials, the Irwin relation is modified to read[28,29]

$$G_{(hkl)[uvw]} = K^2/M_{(hkl)[uvw]}, \qquad (5)$$

where the $(hkl)[uvw]$ notation of Wachtman has been used;[29] the direction of crack propagation, consistent with the elastic-anisotropy fracture analysis of Sih et al.,[28] is the vector cross product $[hkl] \times [uvw]$. K is still a material-independent scalar that depends only on external boundary conditions, but the mechanical energy release rate $G_{(hkl)[uvw]}$ is now a (complicated) vector function that depends on material elastic anisotropy and crack orientation through the elastic fracture factor $M_{(hkl)[uvw]}$. (Different notation is used here than that by Refs. 28 and 29, and the factor of π has been omitted from the Irwin relation and incorporated into the definition of K in accordance with common usage.[26]) For SCS, with cubic symmetry, it can be shown[29] that there are four unique values for $M_{(hkl)[uvw]}$ that are a subset of those developed for materials of orthotropic symmetry for which a crack is propagating on a symmetry plane[28] and which can be expressed directly in terms of the elastic constants s_{ij}. The first of these M values is of somewhat limited usefulness for SCS as it describes fracture on the tertiary (001) cleavage plane but provides physical insight. After some manipulation (assuming plane-stress, mode-I loading only)

$$M_{(001)[100]} = \left[\frac{4}{s_{11}(2s_{11} + 2s_{12} + s_{44})} \right]^{1/2}. \qquad (6)$$

For an isotropic material, $s_{44} = 2(s_{11} - s_{12})$ and the isotropic Irwin relation is recovered

$$M_{(iso)} = \left[\frac{1}{s_{11}} \right]_{(iso)} = E_{(iso)}. \qquad (7)$$

For SCS, using the expressions for $E_{[110]}$ and $E_{[100]}$ given in the Appendix, the result is

$$M_{(001)[100]} = [E_{[100]}E_{[110]}]^{1/2}, \qquad (8)$$

and it is observed that the elastic fracture factor is not solely the elastic modulus parallel or perpendicular to the fracture plane or crack front ($E_{[100]}$), but includes information regarding other deformation modes ($E_{[110]}$) in the elastically anisotropic crack tip stress field. Rotating the elastic compliance tensor gives, after some manipulation

$$M_{(001)[110]} = \left[2E_{[100]}E_{[110]} \right]^{1/2}$$
$$\times \left[\left(\frac{E_{[110]}}{E_{[100]}} \right)^{1/2} + \left(\frac{E_{[110]}}{E_{[100]}} \right)(1 - SE_{[100]}) \right]^{-1/2}, \qquad (9)$$

$$M_{(110)[001]} = [E_{[100]}E_{[110]}]^{1/2}, \qquad (10)$$

$$M_{(110)[\bar{1}10]} = \left[2E_{[100]}E_{[110]} \right]^{1/2} \left[\left(\frac{E_{[100]}}{E_{[110]}} \right)^{1/2} + (1 - SE_{[100]}) \right]^{-1/2}, \qquad (11)$$

using the expression for S given in the Appendix; setting $S = 0$ in these expressions as for an isotropic material recovers $M = E_{(iso)}$. The numerical values of these quantities provide physical insight into the coupling between the external loading and the resultant crack driving force as a function of crack orientation. For the (001) plane, $M_{(001)[100]} = 148$ GPa and $M_{(001)[110]} = 155$ GPa and it is noted that $E_{[100]} = 130$ GPa $< M_{(001)[100]}$ and the M values are comparable. The first observation is consistent with the fact that $\langle 001 \rangle$ are the least stiff directions in SCS and hence anisotropic deformation at a {001} crack tip will always sample directions of greater stiffness and thus M will exceed the moduli perpendicular to the crack plane. The second observation suggests that the coupling between G and K will not depend greatly on the direction of crack propagation for fracture in the {001} planes. For the (110) plane, $M_{(110)[001]} = 148$ GPa and $M_{(110)[\bar{1}10]} = 176$ GPa and it is noted that $M_{(110)[001]} < E_{[110]} = 169$ GPa $< M_{(110)[\bar{1}10]}$. This is consistent with the fact that $\langle 110 \rangle$ are intermediate stiffness directions in SCS and thus crack-tip deformation could sample directions of either greater or lesser stiffness than that perpendicular to the crack plane and thus the coupling between G and K will depend on the direction of crack propagation in the {110} planes. (Atomistic simulations are consistent with this continuum calculation, finding that it is much easier to propagate $(110)[001]$ cracks than $(110)[\bar{1}10]$ cracks.[30]) Explicit expressions for M such as the above for fracture on the (111) plane are not possible as the condition of orthotropy is not met. In this case, the connection between G and K requires the (complex) solution of a polynomial with coefficients derived from the elastic compliance tensor rotated into the $\langle 111 \rangle$ zone[23,28] and is beyond the scope of this work. However, the (001) and (110) considerations above suggest the constraint $M_{(111)[hkl]} < E_{[111]}$, as $\langle 111 \rangle$ are the stiffest directions in SCS, and that the variation in $M_{(111)[hkl]}$ with $[hkl]$ will not be great as $E_{(111)} = E_{[110]}$ is invariant with direction in the (111) plane (see Appendix). As a consequence, a very good approximation is $M_{(111)[hkl]} \approx (E_{[111]} E_{[110]})^{1/2} = 178$ GPa.

3. Connection between fracture energy and toughness for SCS and polysilicon

Combining the equilibrium condition for fracture with the modified Irwin relation gives

$$T_{(hkl)[uvw]} = \left(2\gamma_{(hkl)} M_{(hkl)[uvw]}\right)^{1/2}, \qquad (12)$$

where T is the toughness (often designated K_C, and for isotropic materials taken to be a material constant). Using the parameters given above, the predicted toughness values for SCS for the three major fracture planes are $0.87 < T_{(001)} < 0.89$ MPa m$^{1/2}$, $0.73 < T_{(110)} < 0.80$ MPa m$^{1/2}$, and $T_{(111)} \approx 0.72$ MPa m$^{1/2}$, shown in Fig. 5(d). In previous works,[1,24] the approximation $M_{(hkl)} \approx E_{[hkl]}$ was used and the strongly countervailing orientation dependences of 2γ and E led to almost invariant toughness as a function of crack orientation. The more correct calculation here, which includes resistance to elastic deformation beyond that perpendicular to a crack plane, leads to greater predicted variation of

toughness as a function of orientation; nevertheless, the variation is not great, at most 20% (compared with over 60% for 2γ). (All the calculated toughness values here are slightly greater than those calculated previously;[1] a consequence of a greater selected base $2\gamma_{(111)}$ value.) The fracture resistance for polycrystalline materials, assuming random transgranular fracture and averaging over all the planes in Fig. 5(c), is $2\gamma_{(poly)} \approx 3.9$ J m^{-2}. Using this value and $E_{(poly)} = 163$ GPa from above gives a calculated polycrystalline value from the isotropic Irwin relation of $T_{(poly)} \approx 0.80$ MPa m$^{1/2}$. Care must be exercised in interpreting this value as it reflects a calculation of an *average* polycrystalline response. Locally, in a particular grain on a crack front in a polycrystalline ensemble, the mechanical energy release rate will reflect the elastic anisotropy of that grain relative to the crack orientation.[31] Hence, there will be a tendency for the grain-localized crack path to maximize the local (mechanical–surface) energy release rate, $G_{(hkl)[uvw]} - 2\gamma_{(hkl)}$, and thus provide a driving force away from random transgranular planar fracture. The ensuing, deflected, crack path decreases K, however,[26] and thus provides a restoring force back towards planar fracture. The net effect on the externally applied loading required to propagate a crack is thus strongly dependent on polycrystalline microstructural details; usually, the locally enforced deflections of the crack path lead to a decrease in the global value of K, such that greater forces are required for fracture and the polycrystalline material appears "tougher" in the frame of reference of the external loading (in spite of the fact that fracture is occurring predominantly on planes of lesser fracture energy). Experiments on fracture across single grain boundaries are consistent with this view, finding effective required K values of 0.95–1.2 MPa m$^{1/2}$ to 1.2–1.75 MPa m$^{1/2}$ to transmit cracks across grain boundaries of increasing misorientation between grains.[32,33]

4. SCS fracture energy and toughness measurements

The earliest measurements of fracture energy of SCS, using long cracks in macroscopic "fracture mechanics" specimens, were in substantial agreement with the above predictions from crystallography and bond energy values. Measurements by Gilman[34] using 10–30 mm long $(111)[11\bar{2}]$ cracks in a displacement-controlled double cantilever beam (DCB) geometry gave $2\gamma_{(111)} = 2.48$ J m^{-2} and 0.14–25 mm long cracks in a load-controlled DCB geometry used by Jaccodine[35] gave 2.46 J m^{-2} with about $\pm 2\%$ relative uncertainty (cf. 2.9 J m^{-2} prediction above). In both cases, a modulus of $E = 168$ GPa was used, appropriate to flexure of the [110]-aligned beams of the specimens; the equivalent toughness value was then $T_{(111)} \approx 0.65$ MPa m$^{1/2}$ (cf. 0.72 MPa m$^{1/2}$). Bond energy was inferred from surface energy to give $u_B = 190$ kJ mol^{-1} (cf. 226 kJ mol^{-1}), and predictions for $2\gamma_{(110)}$ and $2\gamma_{(100)}$ are made.[35] Subsequent measurements using a displacement-controlled tapered DCB geometry with 9–21 mm and 11–22 mm $(111)[11\bar{2}]$ cracks gave $T_{(111)} = 0.937$ MPa m$^{1/2}$ with about $\pm 3\%$ relative uncertainty[36] and 0.9 MPa m$^{1/2}$ with about $\pm 10\%$ relative uncertainty,[37] respectively. The advantage of tapered DCB geometry is that K is almost invariant with crack length in

the ranges used, decreasing measurement uncertainty; the large scatter in the latter measurements was attributed to prominent surface steps perpendicular to the crack front resulting from displacement-controlled crack initiation from the DCB notch root. Using $M_{(111)[hkl]}$ given above results in $2\gamma_{(111)} = 4.7\,\mathrm{J\,m^{-2}}$ from these measurements. A test geometry for which K has no dependence on crack length is the double torsion (DT) specimen; measurements on 10–70 mm long $(111)[11\bar{2}]$ cracks in DT specimens fabricated from SCS wafers gave $T_{(111)} = 1\,\mathrm{MPa\,m^{1/2}}$ with about $\pm 5\%$ relative uncertainty.[38] Measurements by Bhaduri and Wang[39] using 8–16 mm long (110)[001] cracks in DT specimens fabricated from SCS wafers gave $2\gamma_{(110)} = 3.62\,\mathrm{J\,m^{-2}}$ (cf. 3.60 J m^{-2} prediction above) using $M_{(110)[001]} = 150\,\mathrm{GPa}$ calculated as described above and thus $T_{(110)[001]} = 0.74\,\mathrm{MPa\,m^{1/2}}$ (cf. $M_{(110)[001]} = 148\,\mathrm{GPa}$; slightly different values of s_{ij} were used in Ref. 39).

The above are all "exterior" measurements of fracture properties, in that conditions at the boundaries of the system are used to impose fracture equilibrium and thus infer the (equilibrium) fracture energy or toughness. Under any condition, the stress field in the large, linear-elastic region surrounding the crack tip is related to the SIF determined by these boundary conditions by

$$\sigma_{ij}(r,\theta) = \frac{K}{(2\pi r)^{1/2}} f_{ij}(r,\theta), \tag{13}$$

where r and θ are radial and angular crack-tip coordinates, respectively, and $f_{ij}(r,\theta)$ are angular functions, which depend on the component of the stress tensor σ_{ij} under consideration[26] and which are functions of the elastic constants if the material is elastically anisotropic.[28] If fracture equilibrium is imposed, such that $K = T$, the above equation can be inverted to provide an "interior" method for measuring fracture properties

$$T = \sigma_{ij}(r,\theta) \frac{(2\pi r)^{1/2}}{f_{ij}(r,\theta)}. \tag{14}$$

Measurements of σ_{ij} as a function of r *in* the body of the material ahead of the crack tip then provide a method to estimate T, once f_{ij} is known (f_{ij} take simple forms for $\theta = 0$, that is, for measurements in the crack plane perpendicular to the crack front[26,28]). The Raman shift of Si depends on the state of strain[40] and hence measurements of the Raman peak position adjacent to a crack tip can provide a method for measuring K and thus T. Raman shifts in (100) and (111) Si discs under biaxial stress fields were calibrated assuming plane stress in an elastically isotropic material surface.[41] The calibrations were then used to measure the variation of stress adjacent to 10 mm long cracks in wedge-loaded DCB specimens containing (110) cracks (the orientation is given as "unknown," but other information strongly suggests this orientation). Although the variation of stress with radial distance from the crack tip was weaker than the $r^{-1/2}$ dependence above, force fits to the measurements gave estimates of T in the range of 0.62–0.81 MPa m$^{1/2}$. Although, in general, interpretation of Raman shifts as components of the stress or strain tensor is a complicated function of both the elastic

constant and stress-optical coupling tensor elements,[40] the direct scalar calibration used in Ref. 41 and the averaging over specimens of different orientations imply that the average values of T deduced are reasonably accurate. Another interior fracture measurement method used the relationship between the SIF and the displacement field in the linear elastic region. On imposing equilibrium and inverting, a relationship similar to that above is obtained[26,28]

$$T = 2Mu_j(r,\theta) \frac{(2\pi/r)^{1/2}}{g_{ij}(r,\theta)}, \tag{15}$$

where $g_{ij}(r,\theta)$ are angular functions that depend on the component of the displacement u_j under consideration. Measurements of u_j as a function of r *behind* the crack tip (the "crack-opening displacement" for u_j perpendicular to the crack plane and $\theta = \pi$) then provide a means to measure T. Finite element analysis (FEA) was used to calibrate the ratio (M/g) for crack opening displacements of a wedge-opened crack in an assumed elastically isotropic material[42] and then applied to the surface traces of 10–60 μm long indentation cracks in a range of materials. The value reported for (probably) (110) fracture in Si was $T = 0.84 \pm 0.03\,\mathrm{MPa\,m^{1/2}}$. Although passing over many important factors, the agreement with toughness measurements of other materials suggests that this interior method, too, is reasonably accurate.

Measurements of fracture properties of SCS using short cracks, formed in micromachined specimens, are in agreement with the above long crack measurements. Connally and Brown[43,44] formed free-standing cantilever beams, 75 μm long $\times$ 20 μm wide $\times$ 5 μm thick, by standard lithography and etching methods and then used instrumented indentation ("nanoindentation") to generate linear surface cracks across the cantilever width, approximately 3.3 μm deep and 10 μm from the built in end. SEM was used to determine the crack length. Subsequent instrumented indentation loading of the cantilevers propagated the cracks, leading to estimates of $T_{(110)[001]}$ of 0.65 MPa m$^{1/2}$ and 0.71 MPa m$^{1/2}$ (cf. 0.73 MPa m$^{1/2}$ above). In a similar, but larger geometry, beams 45 mm long $\times$ 3 mm wide $\times$ 3 mm thick were formed by diamond saw, and a conical-section rolling wheel was used to generate linear surface cracks across the cantilever width, about 250 μm deep, in the center of the beam length. Optical microscopy was used to determine the crack length. The beams were then annealed or ground to remove the localized plastic deformation zone formed by the roller contact and thus the associated residual stress field.[1] Subsequent four-point bending of the beams to failure[45] gave $T_{(110)[\bar{1}10]}$ of 0.95 ± 0.07 MPa m$^{1/2}$ (cf. 0.80 MPa m$^{1/2}$ above).

5. Polysilicon toughness measurements

Measurements of the toughness of polysilicon, using short cracks in micromachined specimens, are in agreement with the bond energy, crystallography, and elastic modulus predictions above (at least as lower bounds). Khan *et al.* used a polysilicon film formed with surrounding oxide layers and placed an indentation flaw in the top-surface oxide coating, generating a plastic deformation zone and associated

cracks, which propagated into the underlying polysilicon.[46] Annealing, lithography, and etching processes subsequently removed the oxide layers and the Si underlying the indentation to leave polysilicon tensile bars, 10 μm long × 10–20 μm wide × 3.3 μm thick, and containing cracks 0.76–13 μm long propagating from an edge of a bar and extending through the depth. Electrostatic actuation of the specimens to failure enabled the toughness to be determined from FEA; a median value of $T_{(poly)} \approx 1.1$ MPa m$^{1/2}$ was obtained in a range of 0.2–2.2 MPa m$^{1/2}$. Two changes were made by Khan *et al.* in a subsequent work: the indentation flaw was introduced into an oxide layer adjacent to the intended tensile bar, such that none of the polysilicon specimen needed to be removed, while still including an edge crack, and the polysilicon was deposited with sufficient stress such that on release from the underlying oxide the fixed-fixed beams were placed in imposed tensile strains. The bars were 500 μm long × 60 μm wide × 3.5–6.0 μm thick, containing cracks 10–50 μm long propagating parallel to axes of columnar grains. Crack lengths were determined by SEM. The strains were sufficient to cause crack propagation on oxide release, enabling $T_{(poly)} = 0.81 \pm 0.05$ MPa m$^{1/2}$ to be determined from FEA of three strain levels.[47] A similar "side indentation" method was used in comprehensive studies of similar columnar material by Chasiotis *et al.*, in which edge cracks 2.5–26 μm long were generated in tensile bars 500–1000 μm long × 50–400 μm wide × 1.5 and 2.9 μm thick.[48,49] Crack lengths were determined by atomic force microscopy (AFM). Subsequent loading of the tensile bars in a piezoelectric mictrotensile tester propagated the cracks, enabling $T_{(poly)} = 1.0 \pm 0.1$ MPa m$^{1/2}$ to be determined from over 50 measurements on three separate polysilicon fabrication runs. AFM-based DIC, performed *in-situ* during loading, was used to measure the in-plane displacement field adjacent to crack tips, and the fields compared very well with those predicted from the measured toughness and isotropic linear elastic fracture mechanics analyses. However, the points were made that the range of the toughness measurements, about ±0.2 MPa m$^{1/2}$, was attributable to variability in grain-to-grain behavior of individual cracks, and (isotropic) linear elastic fracture mechanics did not provide a complete description of fracture for a crack tip within a single anisotropic grain.

6. Fracture energy and toughness summary

As summarized in Table I, the above considerations show that predictions for SCS and polysilicon fracture properties from independently measured bond energy, crystallography, and elastic modulus values are in substantial agreement with fracture property measurements using both long (millimeters) and short (micrometers) cracks in both SCS and polysilicon. SCS toughness measurements for (111) fracture varied from 85%–120% of the predicted values and 85%–120% of the predicted values for (110) fracture. For SCS, there was agreement between long crack and more recent short crack measurements, but, as careful as many of these measurements were, experimental quantitative verification of the fracture anisotropy of SCS is still lacking. The 11% increase in toughness or 22% increase in fracture

TABLE I. Toughness of SCS and polysilicon.

Prediction (MPa m$^{1/2}$)	Measurement (MPa m$^{1/2}$)	Test method[a]	Reference
$T_{(111)} = 0.72$	0.65[b]	DCB, $E = 168$ GPa	34
	0.65[b]	DCB, $E = 168$ GPa	35
	0.937	T-DCB	36
	1.0	DT	38
	0.9	T-DCB	37
$0.73 < T_{(110)} < 0.80$	0.74[b]	DT, $M = 150$ GPa	39
	0.72	DCB	41
	0.65	SECB	43
	0.71	SECB	44
	0.95	SECB	45
	0.84	COD	42
$T_{(poly)} \approx 0.80$	1.1	SECB	46
	0.81	SECB	47
	1.0	SECB	48 and 49

[a]DCB = double cantilever beam, T = tapered, DT = double torsion, SECB = single edge-cracked (beam or bar), and COD = crack-opening displacement.
[b]Calculated from stated modulus or elastic fracture factor.

energy for (110) fracture compared to (111) fracture is not evident in the measurements, and, in fact, an unbiased view of the data would suggest the opposite. Polysilicon toughness measurements varied from 100% to 135% of the random transgranular fracture prediction; it seems clear that polysilicon is tougher than SCS, but not by much, in common with other polycrystalline cubic materials, such as MgO that exhibit elastic and cleavage anisotropy,[50] but which lack thermal expansion anisotropy.

Two groups of studies were omitted from the above comparisons: The first uses a recent, but reasonably simply implemented, method to concentrate stress: chemical etching or ion-beam milling to form notched fracture specimens. The second uses a well-established and easily implemented method to generate cracks: indentation fracture. In both cases, the SIF K characterizing the fracture system is, with a few exceptions, inaccurate (the assumed value is different from the true or actual value) or imprecise (the distribution of assumed values about the mean value is large), or both. In both cases, the lack of accuracy or precision is caused by assumptions about the fracture geometry that are untrue or unknown. As a consequence, the failure loads as a function of crack length in notched specimens, in which fracture is unstable, $dK/dc > 0$, or the crack lengths as a function of indention load, for which fracture is stable, $dK/dc < 0$, have ill-defined relations to toughness, T. The fracture mechanics of both of these methods will be considered, briefly, to illustrate the sources of inaccuracy and imprecision. In addition, the fracture mechanics outlined will provide the framework for the review of strengths of micro- and nano-scale Si components.

7. Uncertainty in toughness measurements using notched specimens

The SIF K_a for a crack in a component under a uniform tensile stress σ_a is

$$K_{a} = \psi \sigma_{a} c^{1/2}, \qquad (16)$$

where c is the (defined) crack length and ψ is a related dimensionless crack-geometry factor of order unity.[26] Factors for simple geometries include: a straight, imbedded, through-crack of total length $2c$, $\psi = \pi^{1/2}$ and, a circular, imbedded, crack of radius c, $\psi = 2/\pi^{1/2}$. Proximity to free surfaces increases ψ, for example, a straight, edge, through-crack of length c, $\psi \approx 1.12\pi^{1/2}$. Decreased symmetry removes the invariance of ψ: for the important, typical case of a semi-elliptical surface crack, the geometry factor depends on the ellipse aspect ratio and the location on the elliptical crack front. For example, for an aspect ratio of depth/surface crack dimensions of 0.5, $\psi_{(depth)} \approx 1.07\pi^{1/2}$ and $\psi_{(surface)} \approx 1.17\pi^{1/2}$.[51]

For a component containing a crack of length c_0, fracture equilibrium is obtained by imposing an applied stress σ_f such that

$$K_{a} = \psi \sigma_{f} c_0^{1/2} = T. \qquad (17)$$

The equilibrium is unstable as any positive perturbation in the applied stress or crack length from this configuration leads to $K_a > T$ and dynamic fracture ensues. The stress σ_f is thus the strength of the component

$$\sigma_{f} = T/\psi c_0^{1/2}. \qquad (18)$$

Consideration of the above shows that surface cracks will control failure under uniform applied stress over imbedded cracks of the same geometry and dimensions (as the resulting fracture strength is smaller) and that if the surface cracks are semi-elliptical, the surface will extend in preference to the depth (as the SIF is greater, the crack will tend to the straight, edge configuration). Consideration also shows that strength is a "composite" quantity: there is a dependence on an "intrinsic" material property, the toughness T although this may have orientation dependence (SCS) or location dependence (polysilicon) in the component; and, there is a dependence on an "extrinsic" factor, the crack dimension c_0, although this may have geometry dependence ψ. Variability in the strength of similarly fabricated Si components is then likely to stem primarily from variability in the dimension of the largest incorporated crack, with weak influences of toughness and geometry.

Final consideration shows that toughness may be determined from strength measurements if the crack geometry and dimensions are known, although the strength may be disguised as the unstable load or displacement imposed on the specimen. Incorrect assumptions regarding crack geometry and dimensions lead to inaccuracies in toughness assessment using notched fracture specimens. Specifically, assuming the crack dimension is well-approximated by the notch dimension greatly over-estimates the SIF and hence the inferred toughness. A simple example is that of a very small, straight, through-crack, length c_f, at the base of a semi-circular edge-notched component, notch radius $a \gg c_f$. In the frame of reference of the crack, the (true) SIF is given by

$$K_{(crack)} = 3\psi \sigma_{a} c_f^{1/2}, \qquad (19)$$

where σ_a is the stress uniformly applied to the component remote from the notch and the factor of 3 arises from the well-known stress-concentration of a circular hole. In the frame of reference of the external loading, in which the notch is viewed as a part of the crack dimension, the (apparent) SIF is given by

$$K_{(external)} = \psi \sigma_{a} (a + c_f)^{1/2}, \qquad (20)$$

leading to

$$K_{(external)}/K_{(crack)} = [(1 + a/c_f)/9]^{1/2}. \qquad (21)$$

For a typical MEMS-fabricated component, $a \approx 1\,\mu m$ and $c_f \approx 10\,nm$, and thus $K_{(external)}/K_{(crack)} \approx 3.4$, pointing to the potential for significant over-estimations of toughness and to the potential for great variability in these estimations (as c_f is not controlled or measured) using notched specimens.

Measurements of toughness using notched specimens do indeed exhibit over-estimation and variability. For SCS: $T_{(110)}$ in the range of 0.96–1.65 MPa m$^{1/2}$,[52] although an earlier report using the same geometry gave $T_{(110)} \approx 1$ MPa m$^{1/2}$ with about 3% scatter;[53] $T_{(110)} \approx 1.1$ MPa m$^{1/2}$ (or ≈ 1.4 MPa m$^{1/2}$ if no attempt was made to form a crack at the notch root);[54] $T_{(110)}$ in the range of 1.2–2.5 MPa m$^{1/2}$, $T_{(110)}$ in the range of 0.7–2.1 MPa m$^{1/2}$, $T_{(100)}$ in the range of 1.1–2.2, $T_{(110)} \approx 1.3$ MPa m$^{1/2}$, $T_{(111)}$ in the range of 1.1–1.7, and $T_{(110)} \approx 1.28$ MPa m$^{1/2}$,[55–59] all using the same test geometry as Ref. 60 and $T_{(110)} \approx 2.1$ MPa m$^{1/2}$.[61] Although, from time to time, there is commentary in these works that the reported values are significantly greater than those reported elsewhere, there are no implications that the tests are invalid or that the values suggest that Si bond energies are almost an order of magnitude greater than those measured. For polysilicon, $T_{(poly)}$ has been reported[62] in the range of 1.6–3.2 MPa m$^{1/2}$ (in fact, it was the large values and scatter in these experiments that provided the impetus for the development of the side indentation cracking method[47]). For a range of microstructures, mean values for $T_{(poly)}$ in the range of 1.4–2 MPa m$^{1/2}$ with relative standard deviations of approximately 15% have been reported (no significant dependence on microstructure was observed).[63] For a range of doping types, mean values for $T_{(poly)}$ in the range of 1.5–2.1 MPa m$^{1/2}$ with relative standard deviations of approximately 15% have been reported,[54] along with 1.35 MPa m$^{1/2}$.[64] In the case of polysilicon, the overestimation and variability are less clearly artifacts of the notch test geometry, but the above works should not be cited in support of the values of SCS toughness.

8. Uncertainty in toughness measurements using indented specimens

On surface contact of a brittle material by a sharp indenter (for example, the pyramidal Knoop, Berkovich, or Vickers geometries), a localized zone of plastic deformation (and perhaps phase transformation[65]) forms beneath the contact and remains after indenter unloading and removal. The stress required for plastic deformation is related to the mean contact pressure during indentation, the hardness H, and for a Vickers indenter is given by

$$H = P/2a^2, \qquad (22)$$

where P is the indentation load and $2a$ is the diagonal of the square contact; frequently, $2a$ is measured from the residual contact impression after indentation and P is taken as the peak contact load. Measurements on Si over the load range of interest for indentation fracture show that H is invariant with P (and thus a) ($\approx 10\,\text{GPa}$) and does not vary significantly with doping, surface orientation, or polycrystallinity.[1] The zone of plastically deformed material remains compressed after indentation, leading to a residual stress field in the surrounding elastic matrix that can lead to fracture. In particular, the residual field includes circumferential tension exterior to the plastic deformation zone at the material surface and radial tension beneath the zone in the depth of the material.[66] A consequence is that, above "threshold" indentation loads, cracks can initiate from fracture nuclei formed in the plastic deformation zone and propagate stably into the surrounding elastic matrix. Functionally, for Vickers indentation loads greater than about 0.5 N in SCS, "radial" cracks initiate at the surface near the contact impression corners and propagate away from the impression, perpendicular to the surface. As the load is increased, the cracks also propagate into the depth of the material and may coalesce beneath the plastic deformation zone to form two perpendicular semi-elliptical "half-penny" cracks. For loads greater than about 5 N, "lateral" cracks initiate beneath the surface at the plastic deformation zone boundary and propagate away from the zone, nearly parallel to the surface.

The SIF for the half-penny cracks in the residual indentation stress field K_r can be approximated by the form of that for an imbedded, center-loaded circular crack[51]

$$K_r = \chi P/c^{3/2}, \qquad (23)$$

where c is the crack length measured from the contact impression center and χ is a dimensionless term taking into account surface and indentation geometry effects as well as the amplitude of the residual stress field. Imposing $K_r = T$ gives the predicted variation of the equilibrium half-penny crack length c_0 with indentation load

$$c_0 = (\chi P/T)^{2/3}. \qquad (24)$$

The equilibrium is stable as any positive perturbation in c_0 leads to $K_r < T$, implying an easy method for estimating toughness:[67] Simply measure the indentation crack length for a known indentation load (easily performed on polished Si) and use a calibrated value of χ and the above equation to determine T. For elastically isotropic materials

$$\chi = \xi(E/H)^{1/2}, \qquad (25)$$

where ξ is a geometrical factor. Measurements on a range of brittle ceramics and glasses gave $\xi = 0.016 \pm 0.04$.[67] This methodology and these relations come with significant qualifications, however, that effectively preclude their use to assess the toughness of Si, even qualitatively, and especially in the assessment of toughness anisotropy. The group of materials and indentations used to arrive at the value of ξ

above were carefully selected such that the indentations were near-ideal. In particular, the indentation half-penny crack patterns were not disrupted by lateral cracking, and materials that exhibited non-volume-conserving indentation deformation (e.g., the densifying anomalous glasses) were excluded: Non-ideal indentations exhibited significantly depressed values of ξ and thus χ. Even then, the relative standard deviation over the experimental measurements was still $\pm 25\%$. Si exhibits significant disruption of the indentation pattern, even at moderate indentation loads, especially if the indentation orientation is such that the impression diagonals do not lie along easy cleavage planes[1] and also exhibits densifying phase transformation under sharp indentation. Measurements on SCS show that χ varies by over a factor of two as indentation and surface orientations, and thus degree of lateral cracking, vary. Measurements of the surface traces of (110) and (111) half-penny cracks at carefully aligned indentations in Si do exhibit the correct load dependence,[1] i.e., $c_0 \sim P^{2/3}$, implying that χ/T and thus χ can be invariant with indentation load. However, these measurements extended from 0.1 to 300 N, well over the load range from which the indentations appeared ideal to that at which the indentations were completely dominated by lateral cracks. The implication is that χ was invariant, but suppressed, over the entire load range. This last observation is supported by Raman spectroscopy measurements of stress fields at indentation crack tips (similar to that applied to DCB cracks noted above[41]). Measurements on (110)[001] and (110)[$\bar{1}$10] well-formed Vickers, Berkovich, and cube-corner indentation cracks gave K in the range of 0.2–0.4 MPa m$^{1/2}$,[68] well below the 0.73–0.80 MPa m$^{1/2}$ expected for (110) fracture of SCS, consistent with the idea that the amplitude term for indentation fracture of Si is significantly suppressed, even when the indentations are not noticeably disrupted.

As a consequence, although often cited,[24,69–73] assessment of toughness by indentation crack length measurement in Si is not valid. The value of χ, and its variation with indentation load and indentation orientation, is simply not known well enough, except for qualitative comparisons between near-ideal indentation geometries.[1,73] Most studies performed measurements only over a very limited indentation load range[69,72,73] or did not do so at all,[70,71] such that the assumed contact and fracture mechanics were not validated (i.e., a and c_0 were not shown to have the correct P dependence). Some studies mention lateral crack effects, and such cracks are visible in published images,[69,71] although sometimes as an example of an obviously invalid test.[72] Although the published values are all in the range of 0.7–1 MPa m$^{1/2}$ for many SCS orientations and polysilicon, the numerical agreement with the independent measurements above must be regarded as fortuitous and such studies cannot be cited in support of the toughness of Si or its anisotropy.

Indentations may be used as controlled flaws in strength tests, in which case the net SIF K_{net} acting on an indentation crack in a component under uniform applied stress is given by the sum of K_a and K_r, such that

$$K_{net} = \psi \sigma_a c^{1/2} + \chi P/c^{3/2}. \qquad (26)$$

As K_{net} contains both stabilizing and destabilizing elements, the maximum applied stress sustainable by the component must be obtained by simultaneous solution of the equilibrium condition, $K_{net} = T$, and the incipient instability condition, $dK_{net}/dc = dT/dc = 0$. Doing so shows that under the action of the applied stress, an indentation crack grows stably from its initial length of c_0 to an unstable length of c_m when the applied stress reaches the value σ_m, at which point the system becomes unstable and the component fails; σ_m is thus the strength of the component. These parameters are given by

$$c_m = (4\chi P/T)^{2/3} = 4^{2/3}c_0 \approx 2.52c_0, \qquad (27)$$

$$\sigma_m = \frac{3T^{4/3}}{4^{4/3}\psi\chi^{1/3}P^{1/3}} = \frac{3}{4^{4/3}}\sigma_f \approx 0.47\sigma_f, \qquad (28)$$

where σ_f is the indentation residual-stress-free strength given above. It is clear that the effects of the residual stress field are to generate stable precursor crack extension and to decrease the strength. The weaker dependence on $\chi^{1/3}$ suggests that indentation-strength measurements might be a somewhat more robust method for estimating toughness and this is the case. Although the experiments are more difficult to perform and hence are less frequent, comparison shows much better agreement between raw indentation-strength measurements of Si than between raw indentation crack length measurements; see review in Ref. 1. However, it is also clear that reduction in the residual field, quantified by a reduction in χ, will lead to suppressed precursor crack extension and increased strength; if the value of χ is unknown, the relationship between indentation-strength and toughness becomes uncertain. Indentation-strength measurements of Si are consistent with the above equation and suggest uncertainties in toughness estimation of approximately a factor of two if residual stress and lateral crack effects are not taken into account.[1]

9. Uncertainty in toughness measurements using fractography

Although it is possible to express the indentation strength σ_m in terms of the initial indentation crack length c_0, unless the correct indentation fracture mechanics is used (as above), measurement of c_0 and the subsequent use of the residual-stress-free equation for strength will lead to errors in toughness estimation. As a consequence, although often cited,[74–79] assessment of the toughness of Si by strength measurement of indented specimens and fractographic determination of crack dimensions is not valid. In these studies, Si specimens were indented with Vickers or Knoop indenters (or blasted with a spark discharge[80]) and the strengths measured. The fracture surfaces were then examined and the dimensions of the (mostly semi-elliptical) surface cracks were determined. These dimensions were then used in the above equation to estimate toughness and toughness anisotropy in SCS and polysilicon. Although fracture surfaces are presented in these works and failure locations are obvious, it is not obvious what the crack dimensions were; no criterion for determining a crack dimension or the uncertainty in that criterion is given. Even if this were not the case, there is the unknown factor of what crack length was determined by

fractography in the range c_0 to c_m. Finally, omitting the indentation residual field from the fracture mechanics led to the wrong relationship between strength, crack dimensions, and toughness. As above, although the published values are all in the range of 0.75–1.3 MPa m$^{1/2}$ for many SCS orientations and polysilicon, the numerical agreement with the independent measurements above must be regarded as fortuitous and such studies cannot be cited in support of the toughness of Si or its anisotropy.

D. Strength analyses

1. Residually stressed flaws

Further fracture mechanics considerations allow the strength of Si to be described over a large flaw size range and provide context for interpreting the strengths of small-scale Si components. As noted above, lateral cracks at indentation contacts significantly reduce the contact-induced residual stress field, with the greatest reductions occurring at large contact loads. This effect can be accounted for in indentation fracture mechanics models of strength by modifying the residual stress field amplitude term to include load-dependence[1,81]

$$\chi = \chi_0/(1 + P/P_L), \qquad (29)$$

where P_L is a characteristic indentation load at which lateral crack effects become significant. The indentation strength then becomes

$$\sigma_m = \sigma_L(1 + P_L/P)^{1/3}, \qquad (30)$$

where σ_L is a lower-bound to the strength

$$\sigma_L = \frac{3T^{4/3}}{4^{4/3}\psi\chi_0^{1/3}P_L^{1/3}}. \qquad (31)$$

For $P \gg P_L$, the strength asymptotically approaches the invariant σ_L; for $P \ll P_L$, the asymptotic $P^{-1/3}$ variation of strength with indentation load (Eq. (28)) is obtained.

As also noted above, at small indentation loads, radial cracks may not initiate during the indentation cycle; such indentations are referred to as "sub-threshold" (indentations with cracks are referred to as post-threshold). Sub-threshold contacts still have residual stress fields, both interior and exterior to the plastic deformation zone, and include crack nuclei in the form of shear faults located within the zone. Thus, sub-threshold contacts can still control strength, as the applied stress assists the residual stress field to initiate cracks from these nuclei. Such initiated cracks are unstable and immediately propagate dynamically to failure. The level of applied stress required for crack initiation is thus the strength of the component. The net SIF K_{sub} for a crack nucleus contained within a sub-threshold contact zone is again given by the sum of applied and residual SIFs[82]

$$K_{sub} = \psi\sigma_a c^{1/2} + \kappa H c^{1/2}, \qquad (32)$$

where it is recognized that the effective length for the crack nucleus is smaller than the contact impression, $c < a$, and ψ

will take a different value for the crack nucleus relative to a post-threshold indentation crack. The second, residual stress term in the above equation includes the hardness as the amplitude, reflecting the predominant shear-stress influence on the crack nuclei. The dimensionless geometry term κ accounts for the transformation of this shear stress into an effective mode-I SIF that enables the above equation to be written. Note that the residual SIF term is positive and destabilizing, reflecting a driving force for crack initiation even in the absence of an applied stress. The condition for initiation is that $c = a$, and using this and inverting the above equation gives the applied stress level at initiation σ_{sub} and hence the strength

$$\sigma_{sub} = \sigma_S[(P_S/P)^{1/4} - 1], \qquad (33)$$

where P_S is the threshold indentation load for spontaneous crack initiation in the absence of applied stress and σ_S is a characteristic strength level

$$P_S = \frac{\alpha T^4}{\kappa^4 H^3}; \; \sigma_S = \frac{\kappa H}{\psi}, \qquad (34)$$

where α is an indentation geometry term ($H = P/\alpha a^2$ where $\alpha = 2$ for a Vickers indenter).

Figure 6 shows the strength of Si as a function of flaw size using the three limiting forms for the strength given above: (i) simple, Griffith, surface cracks, Eq. (18), using $T = 0.75$ MPa m$^{1/2}$ and $\psi = 1.1\pi^{1/2} \approx 1.9$ (labelled "crack"); (ii) post-threshold residually stressed indentation cracks, Eq. (30), using the experimentally measured values for SCS of $\sigma_L = 48$ MPa and $P_L = 20$ N (labelled "contact");[1] and (iii)
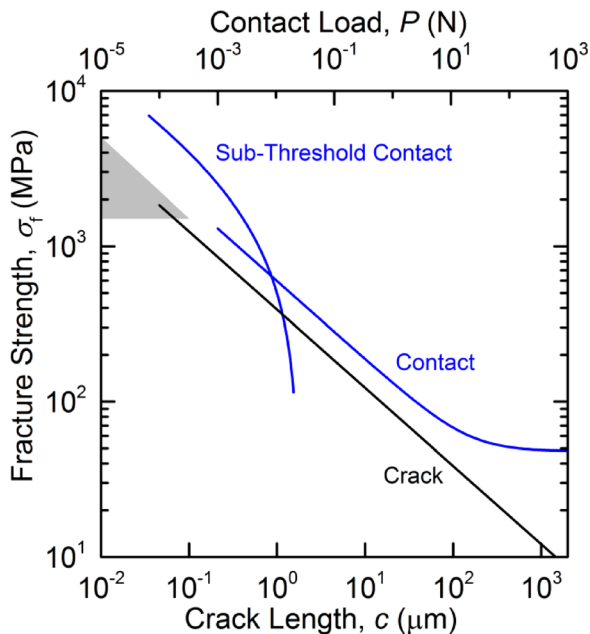

FIG. 6. Fracture strength of Si as a function of flaw size using three limiting forms for strength: (i) simple, Griffith, surface cracks (labelled "Crack"), (ii) post-threshold residually stressed indentation cracks (labelled "Contact"), and (iii) sub-threshold residually stressed indentation nuclei (labelled "Sub-Threshold Contact"). The strength range observed for typical MEMS-fabricated components is indicated by the shaded triangle in the upper left of the diagram.

sub-threshold residually stressed indentation nuclei, Eq. (33), using the experimentally measured values for SCS of $\sigma_S = 2.0$ GPa and $P_S = 25$ mN (labelled "sub-threshold contact").[82] The connection between the lower, crack-length axis and the upper, contact-load axis was made using the experimentally measured indentation fracture invariant of $\langle P/c_0^{3/2} \rangle = 11.5$ MPa m$^{1/2}$ for SCS. The strength range observed for typical MEMS-fabricated components, 1.5–5 GPa (see later), is indicated by the shaded triangle in the upper left of the diagram. The above elastic, plastic, and fracture considerations suggest that the predictions for all three forms of flaws in polysilicon would not differ very much from those in Fig. 6 in the logarithmic coordinates used.

The central, contact response in Fig. 6 represents the strengths of components controlled by the *propagation* of cracks previously initiated at contact sites (ii); the response has $c^{-1/2}$ or $P^{-1/3}$ behavior at small contacts and tends to an invariant lateral crack- or chipping-limited strength at large contacts. Such flaws control the strengths of microelectronic devices[1] in the center of the flaw size range shown, 10–100 μm. It is possible that such flaws could control the strengths of MEMS devices at the small edge of the range, ≈ 1 μm, if sharp, moving components of the devices were to come into contact during device operation (Si indenting Si) or if a moving dust or debris particle were to come into contact with a component (SiO$_2$ indenting Si). However, it is more likely that if the strengths of MEMS devices are controlled by contact events, such contacts would be subthreshold, indicated by the upper response in Fig. 6. The response represents the strengths of components controlled by the *initiation* of cracks from nuclei formed at contact sites (iii) and approaches a $P^{-1/4}$ asymptote at small contacts and a vertical asymptote at the threshold load. For Si, this sub-threshold response intersects the post-threshold response at $\approx 10^{-2}$ N (10 mN) at a contact scale of ≈ 1 μm. Comparison with the characteristic MEMS strength range suggests that sub-threshold contact events of 0.3–3 mN could control the strength of MEMS components, corresponding to contact scales of 50–300 nm.

2. Residual-stress free flaws

The lower response, labelled as "crack" in Fig. 6, represents the strengths of components controlled by the *propagation* of cracks solely under the influence of an applied stress field (i); the origin of such cracks is not specified. In the beam and bar studies above, focused on toughness evaluation,[43–49] cracks 250–1 μm long were formed in components by indentation or contact methods and then the indentation plastic deformation zone and residual stress field were removed by etching or annealing. The strengths of the resulting "simply" cracked components are described by the lower response in Fig. 6 over this crack length range. (The fact that the contact strength response lies above that of the crack strength response implies that ψ, as well as χ, is much reduced from the ideal value for indentation flaws.) Extrapolating this "crack" response into the range of strengths of MEMS components, however, is problematic, as the origin of such simple, Griffith cracks in the required

length scale range of 10–100 nm is not obvious. "Crack" here is taken to mean a sharp crack: An area of broken bonds that is terminated by a small tip zone of dimensions of a few bonds, in which the bond rupture process occurs, surrounded by a large, elastically deformed region, characterized by an $r^{-1/2}$ stress field described by a SIF.[23,26] The formation of polysilicon materials and the shaping of polysilicon and SCS components by etching can both give rise to sources of stress *concentration* in MEMS components: grain-boundary grooves in polysilicon,[83,84] surface etch features such as scallops and pitting in both polysilicon and SCS,[85,86] and component-scale features such as notches and corners in both polysilicon and SCS.[87–91] These are not cracks. However, these sources of stress concentration can be modeled in a continuum sense as triangular notches with a characteristic included angle and infinitesimal notch radius. The stress field in the material adjacent to a loaded notched component is then given by

$$\sigma_{ij}(r, \theta) = K_{\mathrm{n}} r^{\lambda - 1} f_{ij}(r, \theta), \tag{35}$$

which is similar in form to that for a crack (Eq. (13)) but where the *notch*-SIF K_{n} depends on the notch angle γ, as does the divergence of the stress field $(\lambda - 1)$ which is less than that for a crack (i.e., $\lambda > 0.5$).

The *initiation* of a crack at the notch root then focuses on notch-specific values of K_{n}, with units of MPa m$^{1-\lambda}$, set by the far-field boundary conditions. Experiments using bending[88] and tensile[89,90] geometries, along with atomistic simulations,[91] are consistent with such a fracture criterion (somewhat analogous to toughness); the criterion may also be expressed in terms of the existence of a critical stress at a characteristic, atomic-scale, distance from the notch root (exactly equivalent to the theoretical strength). For MEMS components loaded in the far field by destabilizing influences, say, a uniform applied stress, initiation of a crack from a notch root leads to fracture instability, dynamic crack propagation, and component failure; the applied stress required for initiation is thus the component strength. However, cracks can be initiated at such notches by transient stress fields or stabilizing imposed strain or displacement fields. Examples of such fields include thermal or mechanical shock, thermal mismatch with an adjacent component, or wedging by a particle or fluid, to leave a small crack in the stress-concentration field of the notch. For polysilicon, initiation of such cracks from grain-boundary grooves is assisted by the fact that grain boundaries are likely to be less fracture resistant and less stiff than the single crystal. Such zones of weakness are also not cracks (thermal expansion anisotropy cannot give rise to crack initiation in polysilicon, as it can in polycrystalline alumina,[92] as Si is cubic and thus thermally isotropic). Once a crack has initiated at a notch root, the strength is described by Eq. (16), but with considerable uncertainty regarding the enhanced value of ψ characterizing the geometry of the stress concentration. At the lower edge of the typical MEMS strength range, the dimension of the crack is unclear. The crack could be large and resemble a well-formed semi-elliptical crack on a flat surface, Eq. (18) or the crack could be small and resemble a small crack at the root of a stress concentrator Eq. (20). At the upper edge of the MEMS strength range, the dimension of the crack must be very small or non-existent, and hence the shaded region is triangular. Overall, it appears that the strengths of nano- or micro-scale Si components are controlled by crack initiation: either from crack-like nuclei in sub-threshold contact flaws or from crack-free stress concentrations at micromachined surface roughness or notches.

E. Strength distributions

A particular nano- or micro-scale component will likely contain a number of flaws of varying scale, geometry, residual stress state, and local toughness, depending on the fabrication method and mechanical environment. One of these flaws will require the smallest applied stress for fracture instability and will thus set the strength of the component (assuming all flaws are stressed equally, e.g., for a bar under homogeneous tension). Such a flaw may be regarded as having the largest "size" in the component. A group of components will thus exhibit a distribution of strengths if this largest flaw size varies from component to component, that is, if there is a (largest) flaw size distribution on the surface or in the volume of the components. Such flaw size distributions are common, and, as a consequence, brittle fracture is often considered to be a probabilistic process and therefore requires appropriate statistical models to characterize the resulting strength distributions. In 1939, Weibull[93,94] introduced the first statistical model to examine the scatter in fracture strength data; the approach was based on the previously developed weakest-link theory (WLT).[95] WLT is analogous to pulling on a chain, in which failure occurs when the weakest link in the chain is broken. For a chain with n links, Weibull proposed the following mathematical expression for the (cumulative) probability of failure for chains exposed to a stress of σ_{f}:[96]

$$P_{\mathrm{f}} = 1 - \exp\left\{-n\varphi(\sigma_f)\right\}, \tag{36}$$

where the only conditions $\varphi(\sigma_{\mathrm{f}})$ must satisfy are: (i) to be a positive, non-decreasing function and (ii) to vanish at some threshold strength. Weibull then noted that one of the simplest functions to satisfy these conditions was that of a three-parameter power law, which is often used to describe the strength distribution of a group of components

$$P_{\mathrm{f}} = 1 - \exp\left\{-[(\sigma_{\mathrm{f}} - \sigma_{\mathrm{th}})/\sigma_\theta]^m\right\}, \tag{37}$$

where m, σ_{th}, and σ_θ are the three parameters that describe the distribution. m is the Weibull modulus or slope, which describes the variability in the strength distribution (large m values correspond to less variability and small m values correspond to more variability). σ_{th} is the threshold strength, or the stress below which the failure probability is zero. σ_θ is defined as the scaling strength, such that the "characteristic strength," where $P_{\mathrm{f}} = 0.632$, is $\sigma_{\mathrm{c}} = \sigma_\theta + \sigma_{\mathrm{th}}$.

The three-parameter Weibull distribution function given by Eq. (37) includes no information regarding component dimensions, whereas the general expression suggested by Weibull explicitly includes the dimensions of the chain via

the number of links. This omission occurs because in the pre-dominant usage of Eq. (37) it is implicit that the group of components is of identical dimensions and tested in the same way. However, weakest-link concepts indicate that components with strengths controlled by surface flaws should ex-hibit different strength distributions as the component stressed surface area is altered. In particular, larger compo-nents should exhibit weaker strengths, as the probability of including larger flaws is increased (consistent with Eq. (36); as more links are added to the chain, the probability of a given link containing a large flaw increases). Area scaling analyses for component strengths described by the three-parameter Weibull distribution are not prevalent in the litera-ture and here such an analysis is outlined. The two key elements to such an analysis are (i) a flaw distribution exists on the surface of the component that is independent of com-ponent size and (ii) the probability of failure for the compo-nent requires summing over all the "links" comprising the component surface. In practice, specimen size-independent strengths determined by the flaw distribution are used and the sum is converted to an integral. For a component contain-ing surface flaws, this results in

$$P_{\mathrm{f}} = 1 - \exp\left\{-\lambda \int_{A_{\mathrm{s}}} [(\sigma_{\mathrm{f}} - \sigma_{\mathrm{th}})/\sigma_0]^m \mathrm{d}S\right\}, \qquad (38)$$

where λ is the number density of strength-controlling flaws per area,[97] A_{s} is the stressed surface area, and m, σ_0, and σ_{th} are the Weibull parameters that describe the size-invariant distribution. Under simple tension this becomes

$$P_{\mathrm{f}} = 1 - \exp\left\{-(\lambda A_{\mathrm{s}})[(\sigma_{\mathrm{f}} - \sigma_{\mathrm{th}})/\sigma_0]^m\right\}, \qquad (39)$$

and it is apparent that strength decreases as component area increases (in comparison with Eq. (36), $\lambda = 1$/link, and $A_{\mathrm{s}} = n$ links). Comparison of Eq. (37) with Eq. (39) shows that the parameter σ_θ that describes a measured strength dis-tribution of components of a specific size is related to the size-invariant parameter σ_0 by

$$(\lambda A_{\mathrm{s}})(1/\sigma_0^m) = (1/\sigma_\theta^m). \qquad (40)$$

In particular, for two sets of components of stressed areas $A_{\mathrm{s}1}$ and $A_{\mathrm{s}2}$, the parameter σ_θ scales as

$$\sigma_{\theta 2}/\sigma_{\theta 1} = (A_{s1}/A_{s2})^{1/m}. \qquad (41)$$

The threshold strength and Weibull modulus are not affected by the change in component area, $\sigma_{\mathrm{th}2} = \sigma_{\mathrm{th}1}$, $m_2 = m_1$. The invariant underlying flaw-size distribution function, using Eq. (18), for example, is $\varphi_c = [(c^{-1/2} - c_{\max}^{-1/2})/c_0^{-1/2}]^m$, extending from $c = 0$ to a maximum flaw size of $c = c_{\max} = (T/\psi\sigma_{\mathrm{th}})^2$. For components with volume flaws, all of the aforementioned expressions become a function of vol-ume instead of surface area. An assumption embedded in the Weibull analysis and corresponding WLT is that the applied stress samples a large number of "links" or representative area or volume elements, each of which samples from the underlying flaw distribution. There is an implied scale sepa-ration such that the areas or volumes described in the

previous equations are much larger than the size or spacing of the flaws (for the area example above, A_{s} is assumed to be much larger than $1/\lambda$). When the sampling area or volume approaches the flaw size or spacing, more advanced theories are needed such as finite-volume WLT[98] or statistical meth-ods can be replaced with conservatively bounded worst-case analyses.[84]

Although less utilized in the literature today, more recent work has focused on models to predict fracture of components in multiaxial stress states. Barnett et al.[99] and Freudenthal[100] proposed the principle-of-independent action (PIA) model, which is the weakest-link statistical equivalent of the maximum stress failure criterion and only applicable to components in tensile stress states. Bardoff later suggested that brittle fracture should not only be governed by the WLT as in the Weibull and PIA models but also by linear-elastic fracture mechanics, as this specifies both the size of the strength-limiting flaw and its orientation relative to the applied load.[101,102] The Bardoff theory assumed a random flaw orientation and a consistent crack geometry and in doing so calculated the combined probability of a critical flaw being in a specific size range and oriented such that it may cause failure. Nearly a decade later, researchers at the NASA-Lewis Research Center demonstrated a FEA method-ology to predict the reliability of complex components based on data from simple geometries such as tensile or flexural test specimens; the result of this effort was a public domain computer program called the Ceramics Analysis and Reliability Evaluation of Structures (CARES) program.[103] CARES combined three major elements to perform this function: (i) linear elastic fracture mechanics to relate the strength to the size, shape, and orientation of the critical flaw, (ii) extreme value statistics to obtain the characteristic flaw size distribution function, and (iii) material microstruc-ture. To illustrate the approach, results from the fracture of four-point bend bars tested at NASA and then analyzed by CARES were compared to failure predictions for both con-toured hubs and turbine blade rings.[104] The agreement between the two sets of predictions was good, with the small discrepancy probably due to the different stress-volume data used in solving the reliability problem.

For $\sigma_{\mathrm{th}} = 0$, Eq. (37) reduces to the oft-used two-param-eter Weibull distribution function, given by

$$P_{\mathrm{f}} = 1 - \exp\left\{-[\sigma_{\mathrm{f}}/\sigma_\theta]^m\right\}. \qquad (42)$$

This function is easily linearized into the form $y = ax - b$, with transformed probability and strength coordinates, $y = \ln[\ln(1/(1 - P_{\mathrm{f}}))]$, $x = \ln\sigma_{\mathrm{f}}$ and "slope" and "intercept" of $a = m$ and $b = m\ln\sigma_\theta$. For a small group of components and thus a small strength measurement ensemble, descriptive m and σ_θ values are thus easily found using a hand calculator or even manual linear regression methods, explaining the popularity of this function until the 1980s. From a statistical viewpoint, however, it is difficult to see the continued ration-ale for such analysis: Most data analysis software generates parameters and their uncertainties for almost any given (non-linear) distribution, from even large numbers of measure-ments, on desktop computers, in seconds. More importantly,

from a materials viewpoint, the two-parameter Weibull distribution is unphysical for brittle strength distributions: It stipulates that engineering processes must be capable of generating at least one component containing a strength-controlling flaw greater in size than the component, such that the distribution contains at least one component of zero strength, independent of the size of the component. This is clearly not true. Any manufacturing process or mechanical environment will contain a limitation on the amount of energy that can be expended in creating a strength-limiting flaw in a component, and hence there will always be a concomitant finite largest flaw size (c_{max} above), with a conjugate non-zero smallest strength σ_{th}. It may be true that two-parameter Weibull distributions may be force fit to ensembles of limited numbers of measurements, and appear as good descriptions of measurements in the multiple logarithmic axes required by the linearized coordinates, but the fits are unphysical and (even for limited data sets) usually exhibit systematic bias as a consequence of omission of the threshold strength. An important counterpoint is that with limited data sets, such that the threshold is not well defined, use of the two-parameter distribution provides an inherently conservative estimate of failure probability for strength levels less than the data range. For example, extrapolation of fits to strength levels less than a perceived threshold returns a non-zero failure probability for the two-parameter fit and zero for the three-parameter fit. For engineering purposes in which the value (e.g., 10^{-3} or 10^{-6}) of the non-zero failure probability is used to predict rare events, not just the inclusion of the threshold but the empirical power-law form of the Weibull distribution must also be considered in performing the extrapolation.[98] Assessments of large distributions of components in the review below show clearly that inclusion of the physically meaningful σ_{th} is a necessity (and hence use of a three-parameter distribution). However, many strength studies only report values from the two-parameter approximation, and this is done here for limited comparative purposes only.

III. EXPERIMENTAL METHODS

The development, optimization, and qualification of micro- and nano-scale components are greatly dependent on mechanical properties measurements at small length scales. However, mechanical testing at small length scales is difficult: Not only are the involved loads and displacements small, making measurement difficult, but issues of specimen gripping and loading alignment, which are also often problematic at large scales, are more difficult as well. Also, post-test sample collection and manipulation are taxing, which impedes the ability to identify property-limiting structural defects during failure analysis and thus hinders the development of processing-structure-mechanical properties linkages. To address this measurement need, a number of test structures have been developed to measure the strength of MEMS materials, most of which attempt to replicate large-scale test specimen geometries such as tensile bars, fixed-free beams, fixed-fixed beams, and biaxial flexure plates.[105–108] Because of the aforementioned difficulties with mechanical testing at

small length scales, these studies are typically limited to small datasets, hindering their ability to accurately describe the lower tail of strength distributions. More recent test specimens have enabled statistically meaningful numbers of small-scale strength measurements via more complex geometries and loading schemes. In this section, we review the various experimental methods used to characterize the fracture strength of micro- and nano-scale Si components.

A. Fabrication methods

There are a number of multi-project wafer (MPW) foundries based on both bulk and surface micromachining processes that enable cost-effective, proof-of concept micro- and nano-scale Si components for universities, government agencies, and industry. For SCS, one such MPW foundry is the SOIMUMPs^{TM} process by MEMSCAP. The SOIMUMPs process starts with a silicon-on-insulator (SOI) wafer, which consists of a Si handle wafer, buried sacrificial oxide layer, and Si device layer stack.[109] Two types of SOI wafers are available, the first of which has a 10 μm device layer thickness and a 1 μm buried oxide thickness and the second with a 25 μm device layer thickness and a 2 μm buried oxide thickness (both have a 400 μm handle wafer thickness). To start, the Si surfaces are doped by depositing a phosphosilicate glass (PSG) layer and annealing at 1050 °C for 1 h, after which the PSG layer is removed via wet chemical etching. The device layer is patterned via photolithography, etched down to the buried oxide via deep reactive ion etching (DRIE), and finally covered with a sacrificial oxide layer for protection during subsequent etching steps. Similarly, the handle wafer is patterned via photolithography and etched down to the buried oxide via DRIE. The minimum feature size in the SOIMUMPs process is 2 μm.

For polysilicon, materials from three foundries will be discussed in this review: (i) the PolyMUMPs^{TM} process by MEMSCAP, (ii) the SUMMiT IV^{TM} and V^{TM} processes by Sandia National Laboratories, and to a lesser extent, (iii) the ThELMA^{TM} process by STMicroelectronics. PolyMUMPs is the oldest of the MPW surface micromachining processes and based largely on work at the University of California, Berkeley in the 1980s.[110] In this process, three polysilicon layers and two sacrificial oxide layers are deposited and patterned in a cyclic manner, resulting in one electrical layer (poly0) and two structural layers (poly1 and poly2). The poly0, poly1, and poly2 layers have nominal thicknesses of 0.5 μm, 2.0 μm, and 1.5 μm, respectively, with the poly1 and poly2 layers often combined to generate 3.5 μm-thick components. All polysilicon films are deposited using low-pressure chemical vapor deposition (LPCVD), covered with PSG and annealed at 1050 °C for 1 h to dope the polysilicon and reduce its residual stress, and etched via RIE. Laterally, components typically have in-plane dimensions on the order of ones to hundreds of μm, the former of which is limited by the minimum feature size, $\approx$2 μm, and the latter of which is limited not only by the die size, $\approx$1 cm, but more importantly by phenomena such as adhesion[111–114] and friction.[115,116]

In contrast, the SUMMiT IV and V processes have four and five layers of polysilicon, respectively. The four-level

process allows for complex, interconnected, interactive mechanisms with actuators, whereas the five-layer process allows translation and rotation of these mechanisms over the surface of the Si substrate.[117] SUMMiT IV[TM] has been discontinued, and as a result, only the SUMMiT V[TM] process will be discussed here. Briefly, five polysilicon layers and four sacrificial oxide layers are deposited and patterned in a cyclic process, resulting in one electrical layer (poly0) and four structural layers (poly1, poly2, poly3, and poly4). The poly0, poly1, poly2, poly3, and poly4 layers have nominal thicknesses of $0.3\,\mu m$, $1.0\,\mu m$, $1.5\,\mu m$, $2.25\,\mu m$, and $2.25\,\mu m$, respectively, but can again be combined to form composite layers; for instance, the poly1 and poly2 layers are often combined to form a poly12 layer with a $2.5\,\mu m$ thickness. All polysilicon films are deposited as phosphorus-doped, fine-grained polysilicon in a LPCVD furnace at $\approx580\,°C$ with silane as the precursor gas and etched using RIE. As before, components typically have in-plane dimensions on the order of ones to hundreds of μm, but in this case only limited by a minimum feature size of $\approx1\,\mu m$ or smaller.

The ThELMA process is significantly different than the first two polysilicon processes, in that it is based on the *epitaxial* growth of the structural polysilicon layer, thereby enabling an order of magnitude increase in the layer thickness.[118] The process involves five main steps: (i) thermal oxidation of the substrate, (ii) deposition and etching of the first polysilicon layer (poly1), (iii) deposition and etching of the sacrificial oxide layer, (iv) epitaxial growth and DRIE etch of the second polysilicon layer (poly2), and (v) sacrificial oxide removal and contact metallization deposition. In more detail, the Si substrate is initially covered with a $2.5\,\mu m$ thick sacrificial oxide layer via thermal treatment at $1100\,°C$. Next, the poly1 layer is deposited to a thickness of $0.7\,\mu m$ and etched via RIE, which allows for *thin* polysilicon components and horizontal interconnections. The $1.6\,\mu m$ thick sacrificial oxide layer is then deposited via plasma-enhanced chemical vapor deposition, which taken together with the initial thermal oxide, allows for a $4.1\,\mu m$ gap between the subsequent poly2 layer and the Si substrate. The poly2 layer is grown epitaxially to a thickness of $15\,\mu m$ and etched via DRIE, which allows for *thick* polysilicon components such as microactuators and accelerometers. Finally, the sacrificial oxide layers are removed and the metallization is deposited.

B. Tensile test methods

Tensile testing is a well-known and oft-used technique for measuring the mechanical properties of materials at the macroscale. A typical tensile specimen, or "dogbone," consists of two filleted shoulder sections with an intermediate gauge section; the shoulder sections are wide to promote gripping, whereas the intermediate gauge section is narrow to induce localized deformation in this region. The specimen is mounted into a tensile testing machine, which normally consists of a fixed grip and a moving grip, the latter of which is attached to a load cell. As the grips are moved apart, the load applied to the sample and the displacements between the grips are measured until failure. The load-displacement

data can then be used to determine fundamental material properties such as the elastic modulus, strain-hardening characteristics, and yield or fracture strength. Initial tensile tests of microscale components were based on this same approach, albeit with much smaller grips and much smaller dogbone specimens. However, as the technique has evolved and as specimens have become smaller, researchers have developed more innovative ways to avoid the gripping, loading, and post-test characterization problems associated with the traditional approach.

Early work on tensile testing of SCS and polysilicon mainly focused on the determination of the fracture strength, as direct measurements of the actual specimen deformation (and the resulting values for strain and elastic modulus) were limited. Eisner measured σ_f of SCS whiskers with diameters on the order of $1\,\mu m$ or smaller.[119] The whiskers were held in place between two wire loops with beads of diphenyl carbazide and then tested by displacing a pendulum from its equilibrium position via micromanipulators; the methodology allowed σ_f to be measured with an uncertainty of less than 0.5%. Sylwestrowicz similarly tested SCS crystals at temperatures ranging from -196 to $1380\,°C$ and at strain rates ranging from 0.02 to 1.0 min^{-1}.[120] Much later, Koskinen *et al.* investigated E and σ_f of polysilicon fibers with grain sizes ranging from 50 to 500 μm.[121] Each fiber array, which consisted of 20 identical fibers mounted in parallel, was fabricated via standard microfabrication methods and removed from the Si substrate via two adhesive bars for testing. One end of the fiber array was then glued to a load cell, while the other end of the array was glued to a crosshead consisting of steel blades. The testing protocol consisted of (i) rotating the crosshead in one direction to buckle the fibers and (ii) rotating the crosshead in the other direction to straighten, deform, and eventually fracture the fibers. The stress and strain at each point in the test were inferred from the load cell and test frame displacement, respectively.

Biebl and Phillipsborn conducted mechanical testing on polysilicon test specimens that more closely resembled the prototypical dogbone specimens to elucidate the effect of dopants on σ_f of polysilicon films.[122] The test structure consisted of a narrow test beam surrounded by two wider loading beams; the residual stresses in the film forced the wider beams to apply a tensile force on the narrow beam. The applied force was varied as the length of the wider beams was varied from (20 to 100) μm in increments of 20 μm. The test structure geometry and pre-release residual stress were used to calculate the post-release stresses in the beams, which were then used to extract the tensile strength of the film by assessing the transition between fractured and unfractured specimens. The deformation of the narrow test beam was not monitored, and as a result, the strain in the beam and the elastic modulus of the film were not measured. Read and Marshall later investigated E and σ_f of polysilicon using two methods: a "pick-and-place" method in which the tensile specimen was removed from the wafer and placed into a tensile testing machine and a "skyhook" method in which a probe was glued to one end of the tensile specimen.[123] The stress and strain at each point in the test were inferred from the load cell and DIC measurements from

0.05 μm diameter alumina particles on the specimen surface, respectively, which resulted in values for both E and σ_f. The results from the DIC analysis were described as "marginal," however, leading to a large uncertainty in the strain and elastic modulus.

In 1997, Sharpe presented the first method to directly measure strain on a tensile specimen, thereby allowing for an accurate assessment of E and ν (in addition to σ_f).[124] The samples were fabricated via the PolyMUMPs process and consisted of polysilicon test specimens with a gauge section of 3.5 μm thick by 600 μm wide. Both axial and lateral strains were measured via an interferometric strain/displacement gauge (ISDG) technique using gold markers deposited on the specimens, which resulted in 5 microstrain resolution. The applied load was measured with a load cell with an air bearing to eliminate friction. Yi *et al.* later used this same approach to elucidate E and σ_f of SCS test specimens patterned with four different Si etchants: potassium hydroxide (KOH), ethylene diamine pyrocatechol (EDP), tetramethyl ammonium hydroxide (TMAH), and xenon difluoride (XeF$_2$).[125] In contrast to Sharpe's work, however, these specimens were fabricated on a SOI wafer, using the thin device layer to form the tensile bar and the thicker handle wafer as a frame. Each test specimen consisted of a tensile bar in the $\langle 110 \rangle$ direction and two support columns that were cut away just prior to the test, all of which were glued between a fixed and moving stage. Suwito *et al.* used a different approach to measure the strain in their tensile bars and "t-structures";[89] in that study, the authors measured in-plane displacements (and strains) using speckle interferometry, which has the advantage of not needing a grating or pattern on the specimen surface. The tensile testing system was largely based on that of Read[126] and consisted of a fixed platform and a moving platform, the latter of which was controlled by two piezoelectric stack actuators under independent closed-loop control. The load on the specimen was inferred from measurement of the relative displacement between the two platforms (via calibration) and the deformation in the gauge section was determined via a time-dependent analysis of the speckle intensities. The results from the "t-structures" were interpreted via a complete analysis of the elastic fields at the sharp corners between the gauge and shoulder sections, as these areas were found to be the predominant fracture initiation sites due to the associated stress concentrations.

The inclusion of a direct strain measurement on the tensile test specimens was a significant step towards accurately characterizing the mechanical properties of micro- and nanoscale Si components. However, the aforementioned approach was still fraught with difficulties associated with test structure fabrication and testing. For instance, all of the previous studies used an adhesive to mount the specimens to the grips, which is an easy way to ensure a strong bond between the two surfaces, but becomes time consuming due to cleaning the grips between tests. Moreover, the test specimens required additional fabrication steps to remove portions of the substrate, such that the components were freestanding and could be mounted into the test systems. Tsuchiya *et al.* addressed these issues by developing a tensile testing system
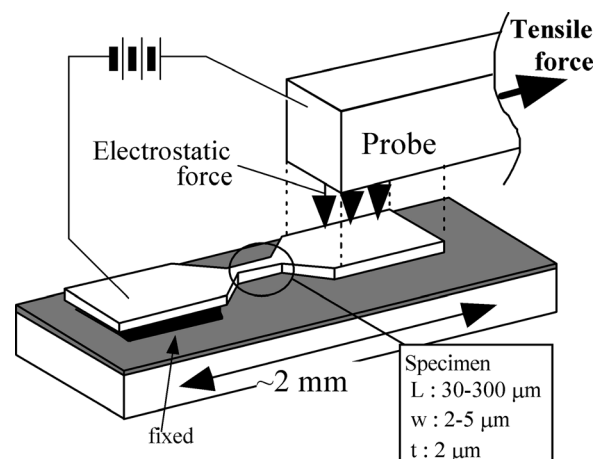

FIG. 7. Schematic diagram of a tensile testing system with an electrostatic-force gripper. The test specimens were tensile bars free at one end and fixed to the Si substrate on the other end; the electrostatic force grip was attached to the free end of the bar by adjusting the applied voltage between the grip and sample. Reprinted with permission from Tsuchiya *et al.*, J. Microelectromech. Syst. **7**, 106 (1998). Copyright 1998 IEEE.

based on an electrostatic-force gripping system mounted in a SEM for *in-situ* observations of the test.[127,128] Figure 7 shows a schematic diagram of the test setup. The test specimens were dogbone tensile bars, free at one end and fixed to the Si substrate on the other; the electrostatic force grip was attached to the free end of the bar by adjusting the applied voltage between the grip and specimen to generate a frictional lock between the two during the test. A tensile force was applied to the bar until it fractured. After the test, the remaining portion of the bar was released from the probe by reversing the polarity of the applied voltage. Load and deformation were monitored using either strain gauges[127] or a load cell and DIC,[128] which were then used to determine E and σ_f of both SCS and polysilicon as a function of specimen size and testing environment.

Sharpe *et al.* later used a similar electrostatic gripping approach to study the effect of specimen size on E and σ_f of polysilicon test specimens.[129,130] To this end, the specimen size was varied, with gauge section lengths, widths, and thicknesses ranging from 50 to 500 μm, 2 to 50 μm, and 1.5 to 3.5 μm, respectively. A die with several of the test specimens was mounted to a five-axis piezoelectric stage. Each specimen was then tested, using the electrostatic probe to grip its free end and a single-axis piezoelectric stage to pull it until failure. The applied load was recorded with a load cell, and the overall displacement of the system was measured with a capacitive-based transducer. σ_f was calculated from the load at failure, whereas E was found using three different methods. The first two methods were applicable to all specimen geometries and focused on subtracting the load cell displacement from the overall displacement of the system to arrive at the specimen deformation; the "calibration" approach required measurements to determine the load cell stiffness and the "differential stiffness" approach depended on testing specimens with equal widths but different lengths. The third method utilized the ISDG technique described above to obtain a direct measure of specimen deformation,

and thus strain, but was only useful on the wider specimens. Bagdahn *et al.* used a similar test setup with notched specimens to investigate σ_f of polysilicon at stress concentrations.[131] Chasiotis *et al.* also used this general approach to measure the elastic and fracture properties of polysilicon specimens with and without notches, but did so via an innovative approach for measuring the strain from DIC of AFM data.[132–135]

Another geometry used to conduct tensile tests on SCS and polysilicon components is the "pull-tab" test specimen, which consists of a tensile bar with a ring at the free end. A probe tip or instrumented indenter tip is inserted into the ring and pulled until the specimen fails in the gauge section. Greek *et al.* first used this approach to investigate the elastic and fracture properties of polysilicon as a function of specimen size.[136,137] The pull-tab test specimen was designed such that its motion was restricted to a straight line (i.e., there was no rotation at the fixed end). The testing apparatus consisted of a probe attached to a voltage-driven piezoelectric actuator and strain gauge force sensor; the strain gauges were found to be slightly non-linear in their response, but could be calibrated via known weights, making the force (and strength) measurements relatively straightforward. The specimen deformation (and strain) measurements were less forthright, however, and required testing specimens with equal widths but different lengths to utilize the differential stiffness method.[137] Independent measurements of E were also conducted using X-ray diffraction and electrostatic test specimen measurements. The entire test setup was mounted inside an SEM, which allowed for *in-situ* measurements and post-test characterization. Schweitz and Ericson later used this same pull-tab geometry to characterize the mechanical properties of SCS along the $\langle 100 \rangle$ direction.[138]

At Sandia National Laboratories, researchers developed a similar pull-tab test specimen, mainly to investigate σ_f of polysilicon as a function of processing conditions, specimen size, and test temperature and environment.[83,139–141] This pull-tab design included a free-rotating pivot on the substrate end of the device as shown in Fig. 8, which allowed for self-alignment to minimize bending errors associated with off-axis loading. Early versions of the specimen design and test methodology suffered from two problems: (i) the specimens failed outside of the gauge section[139] and (ii) the lateral force applied to the ring end of the pull-tab was a convolution of elastic tensile forces and substrate friction forces.[139,140] Both issues were later addressed via a redesign to the pull-tab to include larger fillet radii and more robust pivot designs[140] and the addition of a custom-built mechanical probe station.[83] The new probe station consisted of a load cell with a tungsten probe tip, machined into a cylindrical geometry with a focused ion beam (FIB), to apply the load and a resistance coil die heater to heat the components to over $800\,^{\circ}\mathrm{C}$ in an environmental chamber.[83] Miller *et al.* used a variant of this specimen design and the same probe station to measure σ_f of SCS components from the SOIMUMPs process.[85] Recently, Boyce developed a "slack-chain" pull-tab design to test thousands of specimens at a rate of approximately one per minute; the new approach permitted the rapid evaluation of polysilicon σ_f distributions.[142] In this design, force was
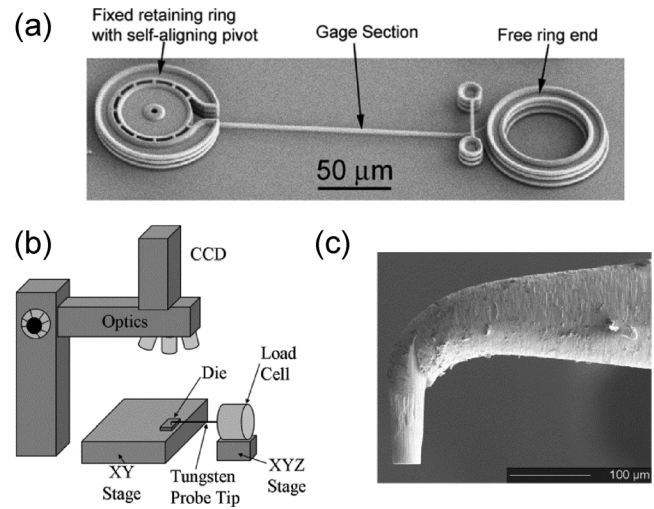

FIG. 8. (a) SEM image of a pull-tab test specimen fabricated with the SUMMiT V process. (b) Schematic diagram of a mechanical probe station. (c) SEM image of a FIB machined tungsten tip with a $35\,\mu m$ tip diameter used to hook and pull the pull-tab test specimen. Reprinted with permission from Boyce *et al.*, J. Microelectromech. Syst. **16**, 179 (2007). Copyright 2007 IEEE.

applied to the free end of the chain and was initially transmitted only to the test specimen closest to the applied load. After the first specimen fractured, the load was transmitted to the second tensile specimen until fracture, which was then repeated until all of the specimens in the chain were tested. This high-throughput approach allowed a statistically relevant number of samples to be tested, thereby providing an accurate evaluation of the lower bound of the σ_f distribution.

In another study on the strength of polysilicon from the SUMMiT V process, Hazra *et al.* demonstrated a compact on-chip tensile tester with a prehensile grip mechanism.[143,144] A schematic diagram and field-emission SEM image of the device are shown in Fig. 9. The upper end of the tensile bar was fixed to the substrate via a support structure, while the lower end of the tensile bar was connected to a freestanding crosshead with displacement gauges and the female ends of a prehensile gripping assembly. The lower part of the device consisted of a shuttle that connected the corresponding male ends of the gripping assembly to a chevron-type thermal actuator. A voltage was applied across the thermal actuator legs to engage the gripping assembly and load the tensile bar. As the voltage increased, Joule-heating-induced expansion of the legs induced shuttle motion and eventually gripper insertion. As the voltage decreased, cooling-induced contraction of the thermal actuator legs resulted in gripper engagement and eventually tensile bar loading and fracture. The displacement of the tensile bar was measured throughout the test using a custom long-working distance interferometric apparatus with a pattern matching algorithm focused on the displacement gauges. The measured displacement was then converted to the gauge section displacement using a compliance correction factor from FEA of the tensile bar. At fracture, the displacement of the gauge section was used to calculate the fracture strain, which was then multiplied by $E_{(poly)}$ to arrive at σ_f. Myers *et al.* later
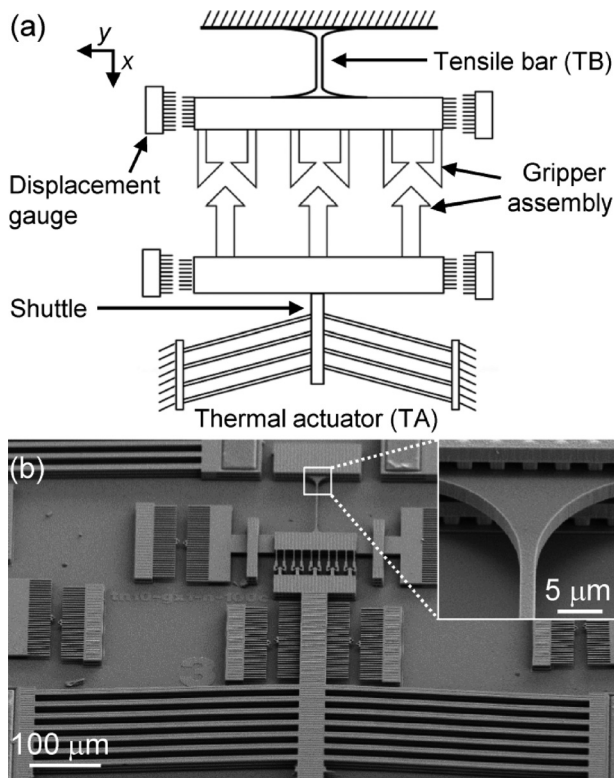
FIG. 9. (a) Schematic diagram and (b) SEM image of an on-chip polysilicon tensile testing device with a prehensile grip mechanism. Joule-heating-induced expansion of the thermal actuator legs resulted in shuttle motion and gripper insertion, whereas cooling-induced contraction of the legs resulted in gripper engagement and tensile bar loading. Reprinted with permission from Appl. Phys. Lett. **104**, 191908 (2014). Copyright 2014 AIP Publishing LLC.

used confocal Raman microscopy (CRM) to measure stress in the tensile bar prior to fracture.[145] The tensile bar was placed in various levels of uniaxial tension and two-dimensional maps of Raman spectral shifts were formed. FEA models of the devices allowed for direct comparison of the spatial variation of predicted and measured stresses, and a polycrystalline opto-mechanical analysis enabled direct comparison of the magnitude of predicted and measured stresses.

Gravier et al. and Urena et al. used a completely different on-chip method to investigate the mechanical properties of polysilicon[146] and SCS[147] thin films, respectively. The basic premise for the test specimen was to use internal stress in one material, referred to as the "actuator," to impose a load on the material of interest. In the first study, the test material was polysilicon and the actuator material was Si_3N_4, both of which were deposited on a SiO_2 sacrificial layer. After removing the sacrificial layer, the actuator was allowed to expand or contact, thereby applying a force and inducing a displacement in the test material. The stress and strain in the test material were then assessed, given that the displacement of the test specimen and the elastic modulus and mismatch strain of the actuator material were known. The displacement of the test specimen was measured on digitized images taken from a field-emission SEM as the relative displacement between a fixed and moving pointer. The mismatch strain in

the actuator material was inferred from both self-actuated test specimens and free actuator bars. Finally, the elastic modulus of the Si_3N_4 was measured via instrumented indentation. The stress-strain response was used to calculate E, and the stress corresponding to the last unbroken sample in the series was taken as σ_f. In the second study, the test material was SCS and the test specimens were fabricated on a SOI wafer along the [100] direction. The elastic properties from the on-chip method were compared to those from dynamic resonance-based methods. Moreover, the elastic and fracture properties were measured as a function of surface-to-volume ratio to investigate their dependence on specimen size.

To avoid many of the gripping, mounting, loading, and post-test characterization issues associated with the previous designs, Quinn et al. developed a micromachined "theta-like" test specimen to measure σ_f of SCS at the microscale.[148,149] The new design consisted of an outer ring with a central bar, or "web region," of uniform cross section. The web region is placed in tension by diametrally loading the outer ring in compression using instrumented indentation. The original test specimen, which was based on a macroscale design first used by Durelli to study photoelasticity[150] and named for its likeness to the Greek letter Θ, demonstrated its viability as a microscale technique, but also revealed a number of problems: mounting the specimens for testing was difficult, non-ideal loading led to undesirable stress concentrations,[151] and collecting the broken parts after testing for fractography was difficult. A later version of the theta test specimen improved on many aspects of the original concept[152] and is shown in Fig. 10. Most notably, the new specimen was designed with a "top hat" to minimize loading misalignments and stress concentrations, fabricated using SOI wafers for better control of device thickness, and tested using a break-detection routine to minimize damage after specimen failure. In addition, the complex inner geometry of the original Durelli design was replaced with a simple arch, thereby reducing the size and extent of secondary stresses in the specimens on loading. Gaither et al. used the original Durelli and new arch theta test specimens to examine both unintended[153] and intended[86] etching process effects on the surface structure, fracture strength, and reliability of SCS. In these studies, the load-displacement response at the load-point was translated into stress-strain behavior across the web region using FEA and σ_f for each specimen was calculated from the peak load at sample failure. In addition, the surface roughness for each etching recipe was determined by AFM, and sample fragments were examined via SEM. Surface roughness topography and fracture origins located during fractographic analysis of tested samples were then compared with strength-limiting flaw size calculations based on Eq. (18). A more detailed investigation of the surface roughness from each etch recipe has recently been conducted via height-height correlations of the AFM data.[154]

As the size of components has continued to shrink, the need for in-situ mechanical testing methods has become increasingly more important, as they provide a valuable way to both qualitatively and quantitatively examine the component as it is loaded and eventually fractured. As an example,
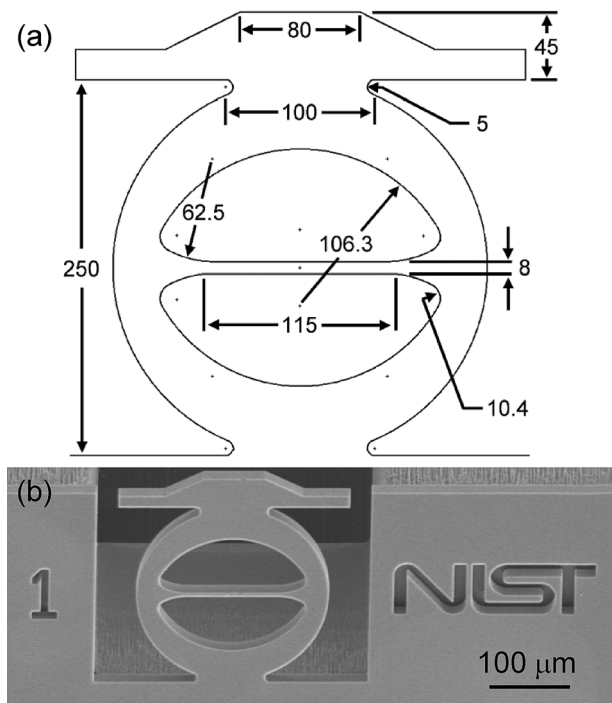
FIG. 10. (a) Engineering drawing and (b) SEM image of an arch theta test specimen (dimensions are given in μm). The web region was placed in tension by diametrally loading the outer ring in compression using instrumented indentation. The load-displacement response at the load-point was translated into stress-strain behavior across the web region using FEA. Reprinted with permission from Gaither et al., Scr. Mater. 63, 422 (2010). Copyright 2010 Elsevier.

Zhu and Espinosa developed a material testing system for *in-situ* electron microscopy based on a microelectromechanical device.[155] The device included either a comb-drive electrostatic actuator or a thermal actuator as the actuator and a capacitive-based measurement system as the load sensor. Thin films and nanostructures were both tested with the device, the former via cofabrication with the actuator and load cell and the latter using a micromanipulator or guided self-assembly. As an example of its ability to test thin films, polysilicon test specimens were formed on the device using standard photolithography and FIB etching. In addition, two platinum lines were deposited on the specimen for deformation measurements by image analysis with edge detection software. Two specimens were tested, resulting in stress-strain curves that were used to determine E and σ_f of the specimens. Zhu et al. later reported on a different *in-situ* technique to examine the elastic and fracture properties of silicon nanowires (SiNWs) synthesized using the vapor-liquid-solid (VLS) process with diameters ranging from 15 to 60 nm.[156] In this study, the tests were conducted inside an SEM using a nanomanipulator as the actuator and an AFM cantilever as the load sensor. A single SiNW was clamped to the tungsten tip of the nanomanipulator using electron beam induced deposition (EBID) of carbonaceous materials, pulled away from the Si substrate, moved towards the AFM cantilever, and finally clamped to the AFM cantilever via EBID. The specimen was then loaded and unloaded several times to eventual failure. During this process, a series of SEM images were taken to assess the forces and deformations, which

were subsequently used to calculate the elastic, plastic, and fracture properties.

Other examples of uniaxial tensile test methods include the magnetic-solenoid force actuator method by Ding et al.,[157] the torsional bar method by Nakao et al.,[60] and the direct tensile test method by Banks-Sills et al.[13,158] Although less common, biaxial flexure tests that generate equibiaxial tension in the center of a specimen have also been used to obtain σ_f data on SCS and polysilicon.[159,160]

C. Compressive test methods

Many materials behave differently in compression than in tension. One reason for this difference involves a change in the stress state in the component; tensile test methods commonly put the gauge section of the specimen in a uniaxial stress state, whereas compressive test methods can put the gauge section of the specimen in anything from a uniaxial stress state to a triaxial stress state depending on the aspect ratio of the component.[161] As a consequence, the results from compressive tests are sometimes difficult to interpret. On the other hand, compressive test methods with an instrumented indenter or AFM are sometimes easier to conduct, in that they avoid many of the gripping, mounting, loading, and post-test characterization issues associated with tensile test methods.[153] Consequently, a number of researchers have recently developed test methods based on compressive loading schemes, especially for investigating the mechanical properties of nanoscale SCS components.

For instance, Moser et al. developed a compressive test method[161] to investigate the deformation and failure behavior of micromachined SCS pillars with diameters ranging from 16 μm down to 800 nm, as shown in Fig. 11. The SCS pillars were fabricated from SCS substrates with a 200 nm SiO_2 layer; the SiO_2 layer was grown by thermal oxidation in wet conditions and used as a mask during the subsequent Si anisotropic etching steps. The cylindrical pillars were then
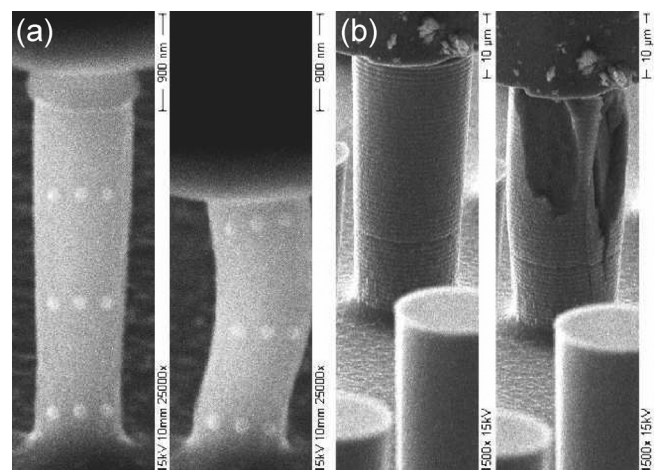

FIG. 11. SEM images of SCS micropillars during the initial (left) and final (right) stages of compression. (a) Significant buckling was found in many of the smallest diameter pillars, whereas (b) axial cracking dominated the failure behavior of the largest diameter pillars. Reprinted with permission from Moser et al., J. Mater. Res. 22, 1004 (2007). Copyright 2007 Cambridge University Press.

placed inside the SEM with a custom-built instrumented indentation module for mechanical testing. The indentation module consisted of two main parts: the sample stage and the tip holder.[162] The former was mounted on top of a load cell and several positioning stages, whereas the latter consisted of a piezoactuator that moved a flexure guide to which the tip holder was fixed. In these experiments, the compression tests were carried out using a diamond flat punch with a diameter greater than that of the largest pillar tested. Load on the sample and displacement of the piezoactuator were recorded for multiple compression tests and used to determine the stress-strain behavior and the associated fracture properties of the pillars. The elastic properties of the pillars were more difficult to ascertain, however, as the piezoactuator-based strain measurements were confounded by a number of effects (e.g., indenter compliance and pillar sink-in). These issues led the authors to investigate a more direct measure of strain based on SEM images of a series of small dots applied to the pillar surfaces via electron-beam contamination deposition. However, this approach was also fraught with difficulties, such as its inability to detect and measure the out-of-plane buckling of the pillars. Östlund *et al.* later used the same *in-situ* indentation system together with a commercially available *ex-situ* instrumented indenter to study the brittle-to-ductile transition (BDT) in SCS pillars at room temperature;[163] in this study, the pillars were fabricated using a FIB technique and ranged in diameter from 940 nm to 230 nm. Wasmer *et al.* also conducted compression tests on SCS pillars using the custom-built indentation module,[164] but this time under a CRM. The stress results from the CRM measurements were compared to the stress results from the indentation module load cell.

Another top-down approach to fabricate SCS compressive test specimens was demonstrated by Li *et al.*[165] In this study, the authors fabricated SCS nanolines with rectangular cross-sections and nearly atomically flat sidewall surfaces. In more detail, the nanolines were fabricated by etching a Si (110) wafer with electron-beam lithography and anisotropic wet etching with TMAH. Using this process, the nanoline width and height were varied from 40 to 500 nm and 100 to 2000 nm, respectively. An AFM-based instrumented indenter with a conical-shaped tip (radius $\approx 4.6\ \mu$m) was then used to compress the nanoline array, and in the process, simultaneously collect the force and displacement data during the loading and unloading process. FEA was used to interpret the force-displacement data and extract the elastic, fracture, and frictional properties of the SCS nanolines.

D. Bending test methods

Bending test methods are similar to compressive test methods in that they avoid many of the gripping, mounting, loading, and post-test characterization issues associated with tensile test methods. Weihs *et al.* originally illustrated this point using the mechanical deflection of a cantilever beam to measure the mechanical properties of Au and SiO$_2$ micro-scale thin films.[166] In particular, the authors noted that bending test methods may be preferential to other methods because of their: (i) limited substrate effects and specimen

handling, (ii) ability to assess local elastic, plastic, and fracture properties with reasonable experimental uncertainty, and (iii) versatility with regards to the test specimen material. Moreover, the bending mode more directly replicates the functional loading condition found in many MEMS-based sensors and actuators. Pantano *et al.* also aptly noted that bending test methods often require smaller loads and produce larger displacements;[108] the former point requires more stringent force resolution, but the later point makes problematic displacement measurements easier. As a result, a significant amount of work has been devoted to developing bending test methods to investigate the elastic and fracture properties of SCS and polysilicon components, some of which is described in this section.

Early bending test methods used a *mechanical stylus* to apply a normal load to the end of a cantilever beam; the load and displacement of the stylus are recorded throughout the loading and unloading process and then used to calculate E and σ_f via an analytical or FEA model. Johansson *et al.* used this method to perform *in-situ* fracture testing of SCS cantilever beams in an SEM.[167] The beams were manufactured in two different ways from a Si (100) wafer, both of which resulted in cantilevers with different thicknesses (8 μm–16 μm) and crystallographic orientations ($\langle 011 \rangle$ and $\langle 001 \rangle$). In the first approach, an *n*-type pattern was diffused into a *p*-type SCS wafer at 1150 °C for 14 h; the diffusion patterns yielded beam shapes that had rounded corners and were independent of crystallographic orientation. In the second approach, an entire *p*-type SCS wafer was subjected to *n*-type diffusion at the same conditions described above and then etched with KOH, yielding beams with sharp corners defined by particular crystallographic planes. Both sets of cantilevers were loaded into the SEM and positioned under the mechanical stylus using a translational stage. The stylus was then used to apply a normal force to the end of each beam until failure. Using an analytical model based on beam theory and linear elastic fracture mechanics, the fracture load was used with the geometry of the beam to calculate σ_f, which was then used with the toughness of SCS to estimate the critical flaw size using Eq. (18). The model was also used to determine E of the SCS components. Ericson and Schweitz later used the same method to test a statistically relevant number of samples to elucidate the effects of surface treatments on E and σ_f of SCS cantilever beams.[168] Four different test specimens were examined: as-fabricated beams, diamond-polished beams, oxidized beams, and HF-etched beams. As before, the resulting σ_f values were used to determine the critical flaw sizes. However, in this study, the calculated critical flaw sizes were compared to cross-sectional TEM results to further validate the approach.

Wilson *et al.* identified two problems with the initial version of the method: (i) the location of the stylus on the beam changed as the beam was loaded and (ii) the analytical model used to calculate the elastic and fracture properties did not account for large beam deflections, material anisotropy, and non-ideal geometry at the base of the beam.[169] The two issues were addressed via changes to the cantilever beam fabrication process and the inclusion of a FEA model. The cantilever beams were fabricated from *p*-type SCS (100)

wafers, using RIE on the front-side to define the length and width of the beam and KOH anisotropic etching on the back-side to define the beam thickness. The process resulted in beams oriented along the ⟨110⟩ direction, with lengths varying from 350 to 750 μm, thicknesses varying from 16 to 30 μm, and widths of 200 μm. Most importantly, a 25 μm through-hole was also etched into each beam, about 150 μm from the free end and along the center line. During a bending test, the stylus was loaded into this hole, thereby preventing relative motion as the beam is deflected and eventually fractured. The force was measured with a force transducer and the displacement was measured with a micro-displacement gauge. The load-displacement data and the fracture force were obtained for each beam tested. The fracture force from the experiments was then used as an input to a FEA model of the beam, which included all of the non-idealities discussed above. σ_f was taken as the stress in the model at the fracture location. Wilson and Beck later extended this approach to not only load the beams on the top and bottom surfaces but also on the side surfaces.[170]

Jones *et al.* developed a slightly different stylus-based bending test method to characterize σ_f of polysilicon test specimens.[171] The test specimens were fabricated with the PolyMUMPs process and consisted of a shuttle tethered to a substrate by a folded flexure. An array of cantilever beams was attached to the shuttle. As the shuttle was displaced in-plane with a probe tip, the ends of the beams contacted several posts fixed to the substrate, which caused each of the cantilevers to deform and eventually fracture. The end displacements at fracture were determined from a video image and were used with non-linear beam theory to calculate the fracture strains. It is important to note that this method only provided fracture strains; σ_f was only calculated after assuming a value for $\bar{E}_{(110)}$.

More recent bending test methods have used an AFM to apply a normal load to the center of a fixed-fixed beam; the AFM is capable of more stringent force and displacement resolutions, both of which are necessary when trying to ascertain E and σ_f of smaller, and thus more compliant, SCS components. Namazu *et al.* developed an AFM-based method to elucidate the specimen size effect on E and σ_f of SCS nano-scale components.[172] Nano-scale SCS beams varying in width from 200 to 800 nm were fabricated on an SCS (001) diaphragm using AFM-induced field-enhanced anodization and TMAH anisotropic wet etching. The field-enhanced anodization was used to create sub-μm lines of SiO$_2$, which were used as mask patterns for the subsequent anisotropic wet etching of the SCS. The resulting beams were oriented along the [110] direction in the (001) plane and trapezoidal in cross-section due to the anisotropic etching process. Each beam was tested using a four step process. First, the length, width, and thickness were measured via AFM. Second, the sensitivity of the AFM probe was calibrated; the AFM probe consisted of a stainless steel rectangular cantilever with a diamond tip. Third, the AFM probe was used to conduct the bending tests, which involved measuring the force and displacement as the beams were deformed and eventually fractured. Fourth, E and σ_f were calculated using an analytical model based on linear elastic
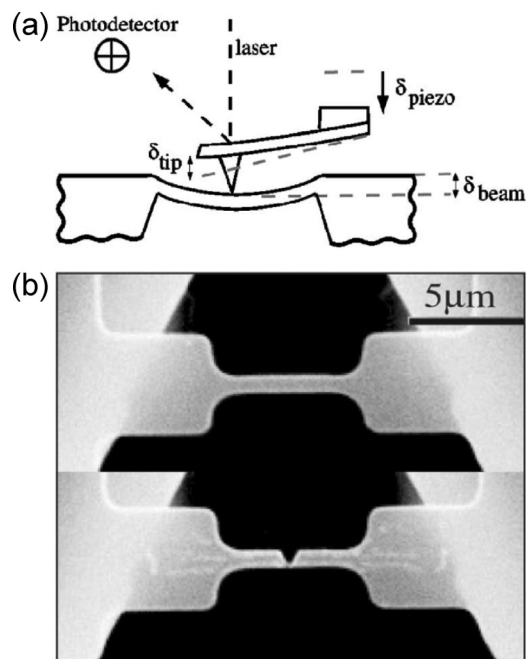

FIG. 12. (a) Schematic diagram of an AFM-based method to determine the fracture strength of SCS fixed-fixed beams. (b) SEM images of beams before (top) and after (bottom) testing; the fractured beams exhibited triangular cleavage along {111} planes. Reprinted with permission from Appl. Phys. Lett. **89**, 091901 (2006). Copyright 2006 AIP Publishing LLC.

theory for isotropic materials. Micro- and milli-scale bending tests were also carried out on SCS beams with a hardness tester and a scratch tester, respectively. Sundararajan *et al.* later used the same method to characterize the elastic and fracture properties of SiO$_2$ nano-scale components.[173]

Alan *et al.* also utilized an AFM-based method to determine σ_f of SCS nano-scale components,[174] as shown in Fig. 12. In this study, however, the authors were interested in studying the effects of surface morphology on the mechanical properties. The SCS test structures were fabricated with standard photolithography and RIE, such that the beams were 190 nm thick, 500 nm wide, and 12 μm long and parallel to the [110] direction. Using a second lithography and etch step, deep triangular wells were formed around each of the beams. The oxide-coated beams were then released from the substrate using two different anisotropic wet etch process, both of which etched non-{111} SCS planes and left the SiO$_2$ intact, but resulted in different SCS surface finishes. Prior to testing, the SiO$_2$ coating was removed from all of the SCS surfaces using a buffered oxide etching solution. In each bend test, an uncoated SCS AFM cantilever was used to deflect the center of each beam to the point of fracture and the applied load and center-point deflection were measured. The fracture load was used to determine σ_f using FEA, which accounted for the large deflections, non-uniform width of the beams, and the anisotropic SCS properties. Alan and Zehnder later reviewed the resulting σ_f distributions and further investigated the effects of surface finish on σ_f using fracture mechanics-based Monte-Carlo simulations.[175] In the simulations, the surface topography of the beams was statistically characterized from AFM height data and then used to generate equivalent surface profiles with randomly

distributed steps. Each of the steps had a "root" or stress singularity with a corresponding notch SIF per Eq. (35) and the simulated beam failed when the SIF at any site exceeded a critical SIF. Using this approach, σ_f for multiple step distributions were determined, resulting in simulated Weibull σ_f distributions that were compared to the experimental results. Alan and Zehnder also used this test method to examine the role of surface chemistry on σ_f.[176] Both hydrogen-terminated and methyl-terminated SCS beams were fabricated and tested; to produce the methyl-terminated beams, hydrogen-terminated beams were exposed to Cl_2 at 3 Torr, illuminated with a 254 nm pen lamp for 3 min, refluxed in methyl Grignard reagent under a constant Ar flow for 2.5 h, and then rinsed in anhydrous methanol and water.

Another approach to fabricate SCS bending test specimens was recently demonstrated by Kirkpatrick et al.[177] The new "gap" theta test specimen was a modification of the arch theta test specimen described above. Whereas in the arch design the web section was continuous, in the gap design the web section was disjointed, resulting in a bending stress state along the frame periphery and no stress in the web under the same diametral loading scheme. Both arch and gap theta test specimens were microfabricated simultaneously, enabling direct comparison of tensile and bending σ_f of lithographically closely related specimens with the same surface finish, but with significantly different stressing modes and stressed areas.

Most of the work described above used top-down fabrication methods to form the test specimens; in general, these methods were "borrowed" from the semiconductor industry and involved forming smaller components from bulk materials using lithography and etching processes. In contrast, there is a growing body of literature that is also interested in using bottom-up fabrication methods to build SCS nanoscale components, followed by characterizing their elastic and fracture properties via AFM-based bending test methods. For example, several studies have fabricated SiNWs using VLS growth methods and then tested their mechanical properties either as freestanding specimens or on a substrate with an AFM. Tabib-Azar et al. used the VLS method to grow SiNWs across two Si posts, and then examined their mechanical properties as a function of nanowire diameter.[178] The VLS process consisted of depositing 1 nm of gold on the Si posts and then exposing the posts to a mixture of SiH_4, HCl, and B_2H_6 in a H_2 ambient at 680 °C for 30 min, which resulted in suspended SiNWs with a [111] growth direction. Three SiNWs were examined: one in a fixed-free configuration and two in a fixed-fixed configuration. The AFM-based bending tests consisted of a three-step process: (i) imaging the nanowire, (ii) deforming the nanowire in 110 nm steps and measuring the corresponding applied force, and (iii) calculating E and σ_f via linear-elastic beam theory. The results from the AFM experiments were finally compared to those from magnetomotive dynamic measurements. Hoffmann et al. also used the VLS method to grow SiNWs on a Si(111) substrate to measure σ_f as a function of nanowire diameter.[179] In this study, however, the nanowires were tested in the as-grown position (i.e., perpendicular to the SCS substrate) using an AFM tip inside of an SEM. The AFM tip was mounted on a piezoelectric arm, while the SCS substrate

was mounted on a piezoelectric stage, both with three degrees of freedom. SEM images were taken as the AFM tip was used to deform the nanowire, and the last image before fracture was used to determine the maximum displacement. With the maximum displacement and the nanowire geometry, σ_f was deduced using both linear-elastic beam theory and FEA. Tang et al. conducted in-situ mechanical testing of SiNWs in a TEM and compared the results to molecular dynamics simulations to gain insight into the effects of nanowire diameter, loading conditions, and stress state on σ_f.[180]

Instead of testing freestanding fixed-free and fixed-fixed cantilever beams, Stan et al. tested SiNWs on a Si(100) substrate, bending them through sequential AFM manipulations and then calculating their σ_f based on the nanowire radius, elastic properties, and bending radius of curvature just prior to failure.[181] The bending radius was determined from topographical images, which were taken between each of the manipulation steps. E was measured as a function of nanowire radius by contact-resonance AFM.[182] Finally, the minimum bending radius of curvature was assessed from the last AFM image prior to fracture, using the contaminants on the SCS substrate to determine the position of the nanowire before springing back from its most bent state. Using all three results, σ_f was calculated from beam theory for a linear elastic and isotropic rod in pure bending. After testing multiple nanowires, the resulting σ_f distribution was used to determine the scale of the defects controlling the strength, which was then compared to TEM images of the stacking fault defects and oxidized surface layers. Stan et al. later used the same approach to measure σ_f of fully oxidized SiNWs.[183]

E. Torsional test methods

Torsion is the twisting of a component in response to an applied torque about its central axis. For a solid or hollow circular component in pure torsion, the stress state is well-defined and similar to that of pure bending, in that the maximum shear stress is found on the surface, and decreases linearly to zero towards the central axis. However, the stress state in a component with a non-circular cross-section is much more complicated, as the shear stress is not constant at a given distance from the axis of rotation and the maximum stress is not necessarily at the farthest distance from the rotational axis. Moreover, pure torsion is difficult to apply, because the loading schemes often result in superfluous axial and bending stresses, making results difficult to interpret.[184] As a result, there are fewer examples of torsional test methods for determining the fracture strength of SCS and polysilicon components.

Saif and MacDonald developed a torsional test method to determine σ_f of SCS pillars.[185] Figure 13 shows a schematic diagram and SEM image of the test method. The SCS pillar was attached to the substrate on one end and to a freestanding lever arm on the other end. The lever arm and thus the sample were twisted using two identical micromachined devices fabricated with the single-crystal reactive etching and metallization process.[186,187] Each device consisted of a comb-drive actuator and a calibrating buckling beam. The voltage on each actuator was increased until its respective
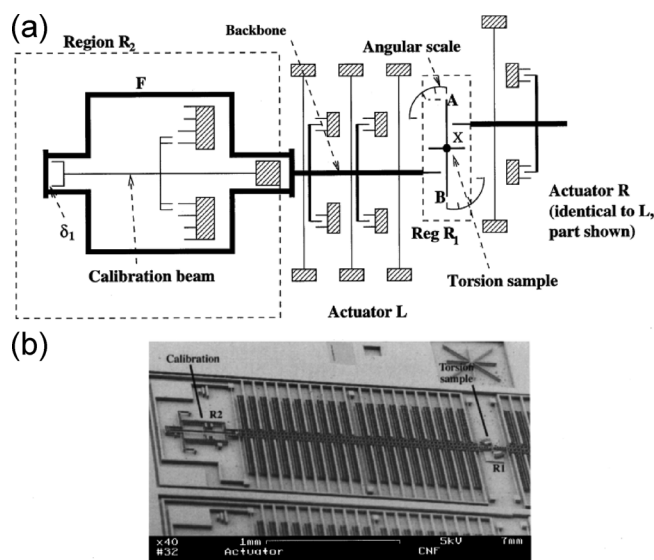
FIG. 13. (a) Schematic diagram and (b) SEM image of a torsional test method to determine the fracture strength of SCS pillars. The voltage on each actuator was increased until its respective calibrating beam buckled, at which point the voltages on both actuators were increased until the pillar fractured. Reprinted with permission from Rev. Sci. Instrum. **69**, 1410 (1998). Copyright 1998 AIP Publishing LLC.

calibrating beam buckled, at which point the voltages on both actuators were increased equally until the pillar fractured. The transverse deformations of the buckled beams and the angle of twist of the SCS pillar were recorded as a function of voltage via optical microscopy and a probe station. Using these data, the force applied by each actuator and the resulting torque on the pillar were determined, which were then used to calculate the SCS shear strength as a function of pillar size. The analytical approach used to calculate the shear strength from the raw data was based on the following assumptions: (i) the first buckling mode can be described by a cosine curve, (ii) the axial deformations of the calibrating beams are small compared to their displacements, (iii) the geometric and material properties of the calibrating beams are well described, (iv) the fixed portions of the actuators are rigid, and (v) the higher-order calibration terms can be ignored.

Schiltges and Dual used a very different approach to measure the torsional σ_f of SCS components.[188] In their study, the test specimen resembled that of a typical dogbone tensile test specimen, with two shoulder and transition sections, and an intermediate gauge section. The specimens were fabricated by KOH anisotropic etching of Si (100) wafers, which resulted in well-defined gauge sections with dimensions $215\,\mu m \times 80\,\mu m \times 50\,\mu m$, but with extremely sharp notches in the transition section that acted as stress concentrators. Each sample was mounted onto a custom-built torsional sensor and actuator, which consisted of a thin steel wire, a rigid bar and plate, and an optical measurement system. The thin steel wire was mounted between the rigid bar and plate, and as a result, a rotation of the wire from an applied torque induced displacements at the opposite ends of the bar. The displacements were measured using a two-point laser interferometer and then used to calculate the angle of

twist and torque on the test specimen via the distance between the two lasers and the torsional stiffness of the wire. Eight different SCS test specimens were tested and the resulting torsional stiffness values were compared to those from numerical simulations. However, due to the stress concentrations in the transition regions, there was no straightforward way to convert the torque at failure to σ_f of the component, at least not without a detailed investigation of the associated SIF. Instead, the authors developed a failure criterion based on energy considerations, which stipulated that failure would occur if the strain energy in a region defined by a critical radius exceeded the surface energy necessary to create two Si (111) surfaces. Meroni and Mazza later used the same test method to again investigate the torsional mechanical properties of SCS components, but this time analyzed the data using FEA simulations and a fracture mechanics approach.[189]

IV. SINGLE-CRYSTAL SILICON FRACTURE STRENGTH

Over the past 60 years, the fracture strength of SCS has been extensively investigated at multiple length scales, with studies ranging in scope from the strength of full-sized SCS wafers,[190–193] to the strength of diced SCS chips,[194–196] to the strength of micro- and nano-scale SCS components.[172,197] Interestingly enough, some of the *earliest* work in this area focused on measuring σ_f of SCS at the *smaller* end of the length-scale spectrum. Eisner measured σ_f of SCS whiskers with diameters on the order of $1\,\mu m$ or smaller to be $\approx 3.8\,GPa$.[119] Pearson later showed that σ_f of SCS whiskers and rods decreased from 2.2 to 0.35 GPa as the characteristic length increased from 20 to 100 μm,[198] which not only demonstrated a size effect in its own right but also revealed a drastic decrease in σ_f (i.e., size effect) as compared to the Eisner results.[119] Sylwestrowicz later tested even larger SCS whiskers (7 cm length and 1.5 mm width) and found an average σ_f of 0.2 GPa, again pointing to a decrease in σ_f with an increase in specimen size.[120] Since that time, there have been hundreds of articles that touch on the topic of SCS strength (Fig. 2) that have not only focused on the effects of component size and geometry but also on the effects of processing and test conditions. This section reviews many of the most salient findings to date in some of the key studies on the fracture strength of SCS.

A. Processing conditions

The techniques used to fabricate SCS microdevices are inextricably linked to the failure process. For instance, the etching processes used to define the *structural* layers can leave residual surface features which act as stress concentrations and initiation sites for fracture and failure. Moreover, the etching processes used to remove the *sacrificial* layers can lead to galvanic corrosion of the SCS, which eventually results in a catastrophic reduction in fracture strength and elastic modulus. However, not all processing conditions exacerbate SCS flaws; some can actually smooth the SCS surface and reduce the native flaw population. Because multiple processing steps are required to create a typical SCS

component and these steps have unique and sometimes differing effects on structure and properties, the overall processing-structure-property relationships for SCS are complex and depend greatly on the exact details of the fabrication sequence.

Early work on etching-process effects on σ_f showed that different etching processes can elicit different residual surface features (i.e., flaw populations), and as a result, different σ_f distributions. Wilson et al. used a cantilever-based bending test method to determine E and σ_f of SCS as a function of etch type.[169] Two different etching processes were used to fabricate the cantilever beams: RIE on the front-side to define the length and width of the beam and KOH anisotropic etching on the back-side to define the beam thickness. σ_f of the front loaded and back loaded beams ranged from 0.7 to 5.0 GPa and 0.6 to 1.5 GPa, respectively. AFM images were used to determine the peak-to-valley heights h_{pv} on both surfaces; h_{pv} ranged from 7 to 9 nm for the front side and 46 to 71 nm for the back side. The rougher, back side surfaces were composed of craters intersecting at sharp peaks, and it was proposed that these peaks act as singularities that make failure more likely to occur than on the front side. In fact, it is more likely that flaws at the *bottom* of the craters acted as the strength-limiting defects, as the protrusions carry little stress. Wilson and Beck later extended this approach to load the beams on the side surfaces.[170] The beams were loaded to failure, and the fracture forces were converted to σ_f via FEA and knowledge of the fracture initiation sites. The σ_f data were divided into two categories based on the two planes along which fracture occurred, {110} and {111}. σ_f for {110}-type fractures was 2.3 ± 0.4 GPa, whereas σ_f for {111}-type fractures was 1.3 ± 0.3 GPa. The difference in σ_f was deemed reasonable, given that the {110}-type fractures occurred in the region with the maximum stress and the {111}-type fractures initiated at the bottom edge of the beams at stresses less than the maximum value (i.e., the differences in σ_f were due to differences in the stress state, not the toughness).

Chen et al. used a biaxial flexure specimen to examine the effects of an even wider range of surface conditions on σ_f of SCS components.[159] SCS test specimens were prepared using two different types of mechanical polishing, chemical polishing, KOH etching, and DRIE and then loaded with a steel punch over a circular hole in an aluminum block. The peak loads were converted to σ_f using FEA, and the resulting σ_f distributions were fit with a two-parameter Weibull distribution function, Eq. (42), to determine m and σ_θ. The authors noted a strong inverse correlation between scaling strength and surface roughness; σ_θ ranged from 1.2 GPa for the mechanically polished specimens with $h_{pv} \approx 3$ μm to 4.6 GPa for the DRIE specimens with $h_{pv} \approx 0.3$ μm (the chemically polished surfaces exhibited smaller h_{pv}, but the corresponding values for σ_θ were outside the measurement range). m was also found to vary with the processing conditions, with values ranging from 3 to 12. The experimental data were not particularly well-described by Eq. (42), which may imply the presence of additional strength-limiting flaw populations in the samples, or may also imply that the two-parameter model was unable to accurately describe the lower tail of the

strength distributions as discussed above. Finally, it is worth noting that both Wilson et al.[169,170] and Chen et al.[159] concluded that KOH-etched surfaces exhibit smaller σ_f than RIE surfaces. However, it is equally important to note that the σ_f distributions for these two surfaces were vastly different from study-to-study, indicating that surface morphology and strength are not only sensitive to the type of etch but also to the operating conditions within a particular etch process.

More recent work has corroborated the fact that large variations in processing conditions are not required to induce changes in σ_f; variations within the same etch process can also lead to σ_f variability. For example, Gaither et al. used the original Durelli and new arch theta test specimens to examine both unintended[153] and intended[86] DRIE process effects on the surface structure, fracture strength, and reliability of SCS. Both specimen designs used tangential circular sections to incorporate the web and had the same diameter of 250 μm and web width of 8 μm, and as a result, the same stressed area of $\approx 6.25 \times 10^3$ μm^2. In the first study, the authors showed that the DRIE process generated two different surface structures leading to two σ_f distributions that were specimen geometry independent: One distribution, with an average value of about 2.1 GPa, was associated with the intended, 35 nm, DRIE scallops, near-ideal web widths, and small surface roughness; the second distribution, with an average value of about 1.4 GPa, was associated with larger, 150 nm, pitting defects, reduced web widths, and large surface roughness. The pits were likely formed when the SiO$_2$ isolation layer separating the device and handle layers was fractured during fabrication, leading to backside DRIE gases passing through the SiO$_2$ layer and re-etching the front-side surfaces. The formation of this unintended rough surface was not related to specimen geometry, affecting both the Durelli and arch designs roughly equally. AFM images and topographic line scans along the loading direction parallel to the scallops, and presumably perpendicular to a fracture-initiating flaws, revealed h_{pv} of 35 nm for the scallop surface and 150–250 nm for the pitting defects, which were again in good agreement with the estimated flaw sizes from the σ_f distributions, Eq. (18).

In the second study, the authors investigated three sets of SCS theta specimens fabricated with two different DRIE recipes and one temperature-controlled cryogenic plasma etching recipe, each set resulting in a different specimen surface structure and strength distribution. The resulting σ_f distributions were fit to a three-parameter Weibull distribution function, Eq. (37), to determine the threshold strength of each distribution, as shown in Fig. 14. In general, σ_{th} varied by about a factor of two, indicating that σ_f was influenced by surface structure. On closer inspection, it was shown that the σ_{th} values for samples with the two different DRIE scallop sizes were (i) the same within experimental uncertainty and (ii) about a factor of two greater than the σ_{th} values for samples with the pitting and cryogenic etch. On point (i), the DRIE samples exhibited almost identical σ_f distributions and h_{pv}, indicating that the strength may not depend on the scallop height or pitch, but on sub-surface flaws generated by, and inherent to, the DRIE process. On point (ii), the samples with diminished σ_{th} (i.e., pitted and cryogenic etch samples)
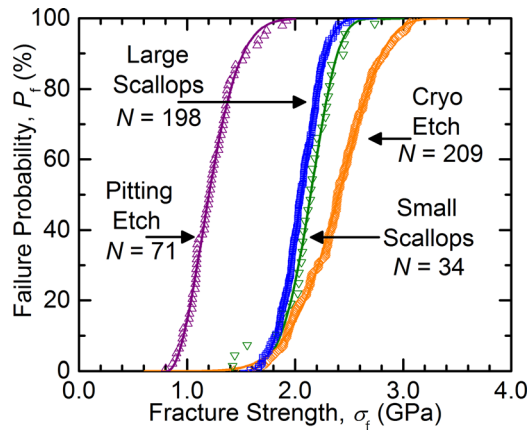
FIG. 14. Strength distributions and corresponding three-parameter Weibull failure probability fits for three sets of SCS theta specimens fabricated with two DRIE recipes and one temperature-controlled cryogenic plasma etching recipe. The strength distribution for the large scallop samples was similar to that of the small scallop samples, whereas the distribution for the cryogenic etch samples was greater on average, but with a larger spread in the distribution. Reprinted with permission from Gaither *et al.*, J. Microelectromech. Syst. **22**, 589 (2013). Copyright 2013 IEEE.

exhibited large h_{pv}, large variability in h_{pv}, or both. DelRio *et al.* later used a height-height correlation methodology to decouple the irregular small-scale roughness from the regular long-range features on these same DRIE surfaces, and in doing so, showed an inverse correlation between σ_c and the root mean square roughness of the surfaces.[154]

The fracture strength of micro- and nano-scale SCS components can be improved (i.e., increased) through the use of appropriate additional processing conditions and controls. For instance, Ericson and Schweitz conducted bending tests on cantilever beams to show that oxidation of the SCS components could lead to drastic increases in σ_f.[168] The [110]-oriented beams were fabricated from *p*-doped (001) SCS wafers via bulk micromachining methods, and then a portion of the beams were exposed to diamond polishing with different grades, oxidation, and HF. The as-fabricated or "reference" beams exhibited an average σ_f of 6.1 ± 0.8 GPa and m of 10.1, which were well above the values previously reported by some of the same authors,[199] and thus a testament to the improved fabrication processes in this work. The diamond polishing was found to decrease the strength of the beams significantly; more explicitly, polishing with $0.25\,\mu$m, $1.0\,\mu$m, and $3.0\,\mu$m particles decreased σ_f by 33%, 54%, and 75%, respectively. In contrast, the thermal oxidation process greatly increased σ_f, not only back to their reference values, but to fracture strengths 15%–20% greater. In the oxidation process, the very top portion of the SCS beam was transformed into a SiO_2 film, which may have strengthened the beams via the formation of oxygen bridges between the cracks induced by the polishing damage.[76] HF etching again reduced the σ_f values, presumably because the SiO_2 film and thus the oxygen bridges were removed during the etch, thereby exposing the underlying SCS flaws. It is worth noting, however, that the HF-etched beams still exhibited greater σ_f than their reference beam counterparts, indicating that the sizes of the strength-limiting flaws must have decreased as a result of the thermal oxidation and HF etching.

Yi *et al.* later used uniaxial tensile testing specimens to illustrate an additional process control that was useful for improving fracture strength in SCS components.[125] SCS test specimens with thicknesses ranging from 3 to 5 μm, widths ranging from 20 to 100 μm, and a length of 6 mm were fabricated from SOI wafers using four different SCS etchants: KOH, EDP, TMAH, and XeF_2. The average σ_f varied from 0.66 GPa for the KOH-etched specimens to 1.22 GPa for the EDP-etched specimens. The variations in strength were described in terms of the surface morphology from each etch process. However, the authors also noted several unexpected results that indicated that the σ_f trends could not solely be described in terms of surface finish. For example, TMAH-etched samples and XeF_2-etched samples exhibited similar σ_f values, despite their markedly different sidewall surface roughness. More importantly, the strengths of the KOH-etched samples were found to be very sensitive to the alignment between the photolithographic mask and the SCS crystallographic orientation; the average value for σ_f decreased from 0.94 to 0.72 GPa as the misalignment increased from 0° to 2°. The misalignment between the mask and SCS orientation created striation marks bounded by {111} planes on the sidewall surfaces, which generated an additional strength-limiting flaw population, thereby decreasing the SCS strength. Therefore, attention to detail with regards to process control can be beneficial to component strength.

On the other hand, additional processing steps and controls can also have a deleterious effect on the fracture strength of SCS components. For instance, Miller *et al.* showed that micro- and nano-scale SCS components coated with Au overlayers can form a galvanic cell when immersed in HF-based solutions,[200] which leads to the autonomous corrosion of the SCS films, in addition to a catastrophic reduction in σ_f of the SCS components. In this study, pull-tab tensile test structures with Au overlayers were mechanically released from the sacrificial SiO_2 layers in aqueous mixtures of either 48 wt. % HF(UDHF), (1:1 volumetric) UDHF:H_2O, or (20:1 volumetric) UDHF:Triton-X-100 for times ranging from 5 to 25 min. Each test structure was loaded until failure using a tungsten probe tip, and the fracture force was converted to σ_f using the cross-sectional area of the gauge section. For the reference specimens (no Au overlayer), σ_θ and m were found to be 2.27 GPa and 12.65, respectively, from Eq. (42). The strength of the specimens immersed in UDHF or UDHF:H_2O decreased with etch time as shown in Fig. 15(a); in detail, σ_θ decreased to ≈ 0.8 GPa after a 12 min etch in UDHF and to ≈ 1.5 GPa after a 24 min etch in UDHF:H_2O (the correlation between changes in m and etch time were less clear, with m unchanged for the UDHF etch, but decreasing for the UDHF:H_2O etch). In contrast, the tensile specimens etched in UDHF:Triton exhibited slightly greater σ_θ (≈ 2.4 GPa) and significantly greater m (≈ 35). The decrease in strength for the SCS etched in UDHF or UDHF:H_2O was attributed to chemical enhancement of individual defects on the top of the sidewall surfaces, whereas the increase in strength for the SCS etched in UDHF:Triton was thought to be the result of blunting of those same defects, as shown in Fig. 15(b). Interestingly enough, the corroded surface layer was only present on the
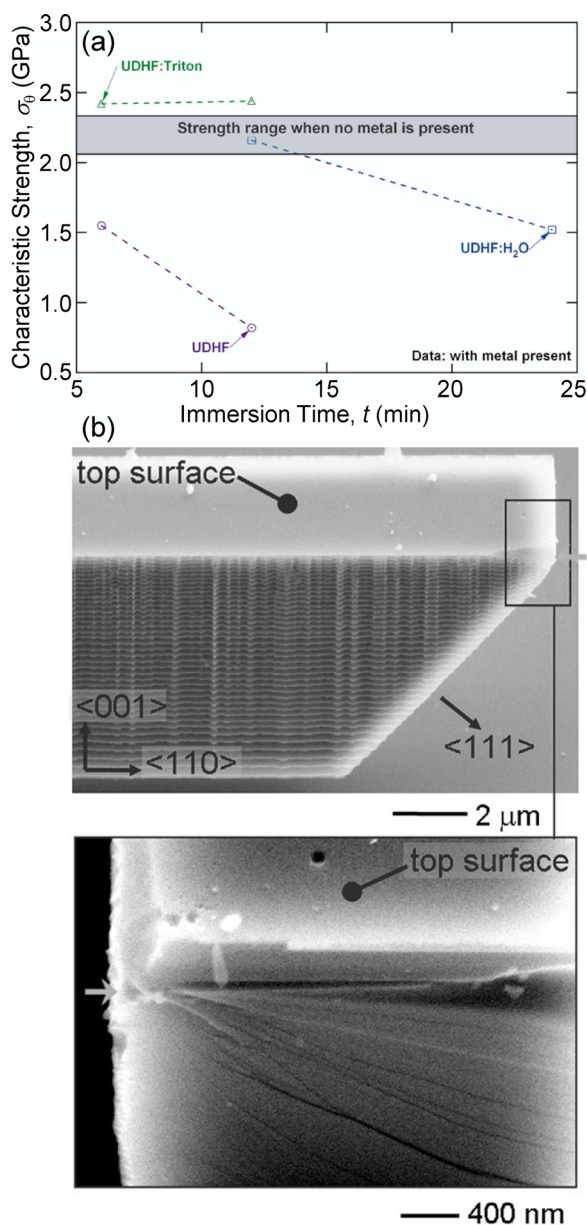
FIG. 15. (a) Fracture strengths for SCS pull-tab test specimens subjected to galvanic corrosion. (b) SEM image of a fractured SCS test specimen, demonstrating that fracture initiated at individual defects on the top of the sidewall surfaces and then propagated on {111} planes. The decrease in strength for the SCS etched in UDHF or UDHF:H$_2$O was attributed to chemical enhancement of individual defects, whereas the increase in strength for the SCS etched in UDHF:Triton was thought to be the result of blunting of those same defects. Reprinted with permission from J. Appl. Phys. **103**, 123518 (2008). Copyright 2008 AIP Publishing LLC.

top surface of each component, most likely because of the dopant distribution profile in the SCS and the charge distribution during the etch process.

Stan *et al.* later showed that oxidation can also have an adverse effect on strength.[183] The authors used an AFM-based method to test both as-grown SiNWs and fully oxidized SiNWs on a Si(100) substrate, bending them through sequential AFM manipulations and then calculating σ_f based on the nanowire radius, elastic properties, and radius of curvature just prior to failure. The fracture strength of an as-grown SiNW with a 26 nm radius was found to be 17.3 GPa,

close to the theoretical ideal cleavage σ_f for SCS of 21–23 GPa.[201,202] Together with the toughness of SCS along the (112) plane (0.8 MPa m$^{1/2}$), this σ_f suggested a strength-limiting flaw size of $\approx$2 nm. In contrast, σ_f of a fully oxidized SiNW with a 29 nm radius was 6.2 GPa, which was again in the range of the ideal fracture strength for the material (i.e., approximately a tenth of the elastic modulus). Taken with the toughness of SiO$_2$ (0.5 MPa m$^{1/2}$), this result translated to a flaw size of $\approx$7 nm as calculated from Eq. (18). Thus, the reduction in σ_f from SCS to SiO$_2$ was due to both an increase in the flaw sizes and a decrease in the toughness. The increase in flaw sizes is in contrast to the results from Ericson and Schweitz,[168] where oxidation actually induced a decrease in flaw sizes (and increase in fracture strength) via the formation of oxygen bridges. Clearly, the effect of oxidation on σ_f of SCS is size-dependent, with an increase occurring in micro-scale components with larger initial flaw sizes and a decrease occurring in nano-scale components with smaller, almost atomically sharp, initial flaw sizes.

B. Component size and geometry

1. Size

In SCS, as with nearly all brittle materials, "smaller is stronger." Equation (41) shows a dependence on relative surface area, as this is the most common location of critical flaws in SCS MEMS, but the same equation applies for relative gauge volumes or relative edge lengths if the flaw population is distributed on those features. The size effect for brittle fracture has been clearly demonstrated in a number of studies of SCS. This section reviews a selection of seminal works that have demonstrated the salient aspects of size effects in SCS.

Namazu *et al.* conducted one of the most comprehensive studies on the size effect on σ_f in SCS,[172] which involved fabricating and testing nano-scale, micro-scale, and milli-scale components varying in width from 200 nm to 1.045 mm and thickness from 255 nm to 520 μm. The extracted values for $E_{[110]}$ were found to be independent of specimen size and consistent with the expected value for SCS, 169 GPa. In contrast, the fracture strength was highly sensitive to the specimen size as shown in Fig. 16; the *average* σ_f for the smallest nano-scale beams (geometry A) was 17.5 GPa, which was 2.3$\times$ (geometry D) to 4.7$\times$ (geometry E) larger than the average σ_f for the micro-scale beams and $\approx$38$\times$ (geometry F) larger than the average σ_f for the milli-scale beams. Moreover, the authors observed a size dependence on the shape and scaling of the σ_f *distribution*; as specimen size increased, both m and σ_θ from Eq. (42) decreased, indicative of smaller and more disparate σ_f values. The observed strengths were used to determine the strength-limiting flaw sizes via Eq. (18), which were found to be in good agreement with the maximum h_{pv} as measured by AFM. Together with fractographic observations, the results indicated that σ_f of the nano-scale specimens was affected by the maximum h_{pv} at the *top* surface, whereas σ_f of the micro-scale and milli-scale specimens was affected by the maximum h_{pv} on the *side* surfaces.
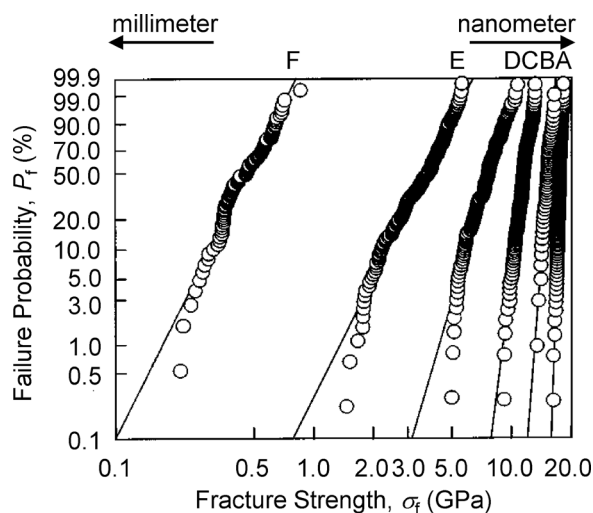
FIG. 16. Strength distributions and corresponding two-parameter Weibull failure probability fits as a function of specimen size for SCS. The average strength for the smallest nano-scale beams (geometry A) was 17.5 GPa, which was 2.3× (geometry D) to 4.7× (geometry E) larger than the average strength for the micro-scale beams and ≈38× (geometry F) larger than the average strength for the milli-scale beams. Reprinted with permission from Namazu *et al.*, J. Microelectromech. Syst. **9**, 450 (2000). Copyright 2000 IEEE.

Other investigators have also characterized fracture strength as a function of specimen size, albeit over a much smaller size range. At the micro-scale, Johansson *et al.* conducted *in-situ* fracture testing of SCS cantilever beams in an SEM.[167] The beams varied in thickness from 8 to 16 μm, in length from 75 to 500 μm, and in width from 75 to 240 μm. In this study, no size effect on σ_f was observed. The authors hypothesized that this may be due to the limited range in the width interval. (In fact, the strength invariance would not be due to a limited width interval, but due to a limited range in *surface area* or *volume*. However, this theory cannot be tested, as the surface areas and volumes for the beams were not reported.) Moreover, the validity of the overall approach is questionable, because the location of the stylus on the beam changed as the beam was loaded and the analytical model used to calculate the fracture properties did not account for large beam deflections, material anisotropy, and non-ideal geometry at the base of the beam, all of which were noted by Wilson *et al.*[169] Miller *et al.* characterized σ_f of two different sets of micro-scale SCS pull-tab test specimens;[85] the length and width for both sets were the same, but the thickness varied by a factor of 2.5. As before, σ_f, m, and σ_θ decreased as the specimen size (thickness) increased. In this case, however, fracture initiated at the base of individual etch defects in the Si, most likely the result of small imperfections in the photoresist mask. The critical flaw sizes calculated from the observed σ_f were consistent with the dimensions of these etch defects, providing another link between the size of etching-induced surface features and fracture strength per Eq. (18). Urena *et al.* measured the elastic and fracture properties of micro-scale SCS test specimens as a function of surface-to-volume ratio to investigate their dependence on specimen size.[147] The average $E_{[110]}$, ≈165 GPa, was invariant with specimen size and

close to the experimental values from dynamic resonance-based methods[203] and the theoretical value for SCS. In contrast, σ_f was found to vary with specimen size, and more specifically, with surface-to-volume ratio. In more detail, σ_f decreased from ≈5.1 to 1.7 GPa as the surface-to-volume ratio decreased from ≈12 to 10 μm^{-1} (or as the width increased from 1 to 10 μm).

Several other groups have characterized the fracture strength and apparent elastic modulus at the nano-scale and have noted that *both* can change as a function of specimen size in this regime. In particular, the former approaches the theoretical limit for the material (i.e., the ultimate strength, ≈21 GPa for SCS), whereas the latter becomes highly dependent on surface stress and oxide thickness. Tabib-Azar *et al.* used the VLS method to grow SiNWs with diameters ranging from 140 to 200 nm and examined both E and σ_f via AFM-based bending tests.[178] E and σ_f varied from 93 to 250 GPa and from 0.30 to 0.85 GPa, respectively, and appeared to vary with specimen size and loading condition. However, only three nanowires were tested, making a statistical assessment difficult. Moreover, the extracted values for σ_f are (i) much smaller, not larger, than the strengths from the aforementioned micro-scale tests, thereby violating the usual size effect and (ii) translate to critical flaw sizes on the order of hundreds of nm, much larger than the diameters of the nanowires. As a result, it is difficult to draw any conclusions from this particular study. Hoffmann *et al.* also used an AFM-based approach to measure the fracture strength of SiNWs with diameters ranging from 100 to 200 nm.[179] The average σ_f from 13 tests was ≈12 GPa. The authors did not observe a relation between strength and diameter, but did note a relationship between strength and length. On further investigation (using the diameters and lengths in their paper to calculate surface areas), there appears to be a weak correlation between strength and surface area, as expected from scaling laws. Zhu *et al.* used an *in-situ* technique[156] to characterize the elastic and fracture properties of SiNWs with diameters ranging from 15 to 60 nm as shown in Fig. 17(a). $E_{[111]}$ remained relatively constant at the bulk value for SCS, 187 GPa, for diameters larger than 30 nm, but drastically decreased to ≈90 GPa at smaller diameters. The decrease in modulus was attributed to the surface stress state, and not the reduced elastic modulus, of the native oxide layer. In contrast, σ_f was found to increase from 5.1 to 12.2 GPa as the nanowire diameter decreased from 60 to 15 nm as shown in Fig. 17(b), which demonstrated the expected size dependence and eventual convergence to the theoretical σ_f for SCS at small diameters. Stan *et al.* later used contact resonance AFM and AFM-based bending tests to show the same trends,[181,182] albeit with large-diameter elastic modulus values (≈160 GPa) consistent with their ⟨112⟩ growth direction[182] and fracture strengths (≈18 GPa) even closer to the theoretical limit for SCS.[181]

2. Geometry

As described above, different processing conditions can induce different residual surface features, which can in turn yield drastically different strength distributions. Variations
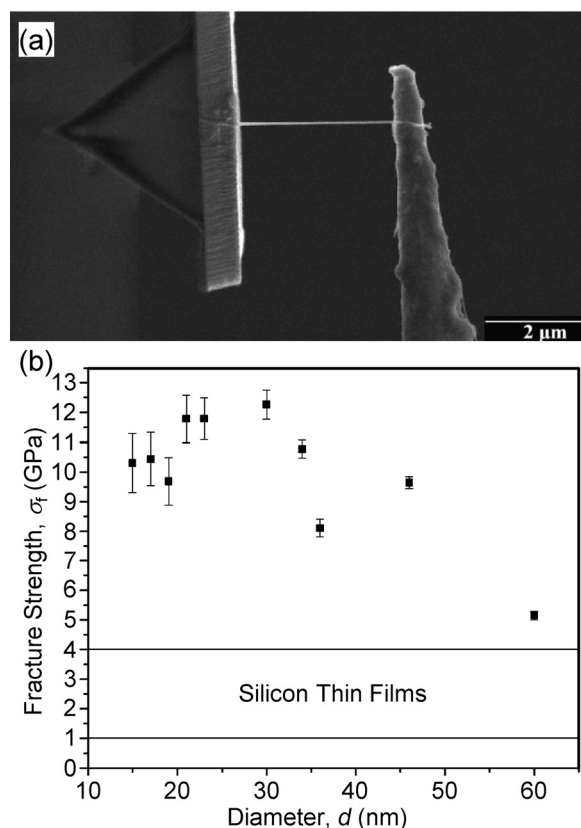
FIG. 17. (a) SEM image taken during an *in-situ* tensile test of a SiNW with a diameter of 23 nm. (b) Fracture strength as a function of SiNW diameter. The strength increased from 5.1 to 12.2 GPa as the nanowire diameter decreased from 60 to 15 nm, which demonstrated the expected size dependence and eventual convergence to the theoretical strength for SCS at small diameters. Reprinted with permission from Zhu *et al.*, Nano Lett. **9**, 3934 (2009). Copyright 2009 American Chemical Society.

in these same processing conditions can also affect the overall geometry of a component, which results in different, but equally important, changes to component mechanical response. For instance, anisotropic etchants such as KOH etch the different SCS crystallographic planes at very different rates; {100} planes are etched at $\approx 1.4\,\mu$m/min, whereas {111} planes are etched almost $400\times$ slower.[89] This disparity in etch rates results in atomically sharp corners at the intersection of the {100} and {111} planes. On the surface, this phenomenon seems beneficial, in that it allows for SCS components with well-defined geometries. However, these sharp corners can also be deleterious, acting as stress concentrations and initiation sites for fracture and failure. As a result, it is crucial to take component geometry into account when calculating σ_f—failure to do so can result in apparent σ_f values much less than the actual strength of the component.

Suwito *et al.* designed and fabricated a series of micromechanical test specimens to study the elastic moduli, strength, and fracture initiation at sharp 90° corners.[89] Three different test specimens were examined: $\langle 110 \rangle$ tensile bars, $\langle 100 \rangle$ tensile bars, and $\langle 110 \rangle$ t-structures. The $\langle 110 \rangle$ tensile bars and t-structures were fabricated by KOH, while the $\langle 100 \rangle$ tensile bars were formed via RIE. In all cases, the force-displacement data were linear to fracture. Only eight
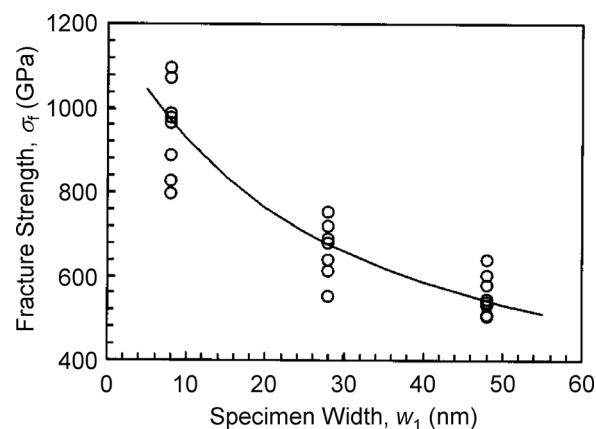

FIG. 18. Measured and predicted fracture strengths of $\langle 110 \rangle$ t-structures as a function of specimen width. The apparent strength scaling with respect to width was well-described by a critical stress intensity criterion for fracture initiation bounded by the tensile bar strength measurements at 1.21 GPa. The agreement between the experiments and model was obtained using a single fitting parameter, $K_n = 2.1$ MPa m$^{0.452}$. Reprinted with permission from J. Appl. Phys. **85**, 3519 (1999). Copyright 1999 AIP Publishing LLC.

of the thirteen $\langle 110 \rangle$ tensile bars with a width of 28 μm failed in the gauge section; the remaining specimens failed at a sharp corner between the shoulders and gauge sections, presumably due to the stress concentration at that location. From the eight specimens, the average σ_f was found to be 1.21 ± 0.35 GPa, which compared favorably to σ_f of SCS whiskers with the same cross-sectional area.[198] In contrast, the measured strengths of the t-structures were much less than those from the tensile bars, with σ_f decreasing from 0.95 ± 0.11 GPa to 0.56 ± 0.05 GPa as the specimen width w_1 increased from 8 to 48 μm, as shown in Fig. 18. This apparent strength scaling with respect to specimen width was well-described by a critical stress intensity criterion-based model for fracture initiation, bounded by the tensile bar strengths of 1.21 GPa. The agreement between the experiments and model were obtained using a single fitting parameter, the *notch*-SIF K_n as given by Eq. (35). For $\gamma = 90°$ here, $K_n = 2.1$ MPa m$^{0.452}$. In conjunction with other K_n data on SCS,[74,88] the authors note that K_n increases as γ increases (albeit with different units), consistent with previous observations for acrylic.[204] Bailey and Sethna later conducted atomistic simulations[91] to calculate K_n as a function of γ and compared the results to those of Suwito *et al.*[89] The authors showed that the shape of the K_n versus γ curve was dependent on the K_n units; K_n varied with γ for K_n in absolute SI units, whereas K_n was nearly invariant with γ for K_n in relative atomic units. The observation indicated a direct link between the macroscopic measurements and a microscopic length scale, with the length scale related to the size of the cohesive zone ahead of the notch.

Shortly after the original work by Suwito *et al.*,[88] Mazza and Dual also studied the mechanical behavior of microscale SCS components with sharp notches, but with much larger notch angles, $\gamma = 135°$.[90] The test specimens consisted of two large plates connected by a gauge section, which was formed using KOH-based anisotropic etch solution. The gauge sections were oriented along the $\langle 100 \rangle$ direction, with thicknesses from 40 to 60 μm, widths from 50 to 90 μm, and

"lower-side" and "upper-side" lengths from 200 to 240 μm and 300 to 340 μm, respectively. The measured forces and deformations were converted to stresses and strains via geometric considerations; the resulting σ_f assuming failure in the gauge section was found to be 0.59 ± 0.02 GPa. However, it was noted that fracture always initiated at the tip of the sharp notches on the bottom of the specimen, indicating that the actual σ_f of the component was much larger than the reported value. To resolve this discrepancy, FEA models were combined with approximate analytical solutions, leading to the determination of the critical stress intensity for this particular geometry. For $\gamma = 135°$, $K_n = 48.4$ MPa m$^{0.326}$, which coincides with the previously reported trend that K_n increases as γ increases. Because K_n was again shown to be dependent on γ, a new scalar criterion was proposed. One of the proposed failure criteria was again based on a microscopic length scale, this time a critical radius from the notch tip R_{cr}, which represented the distance at which the elastic strain energy in the surface layer exceeded the surface energy required to form two new surfaces. For the case considered, experiments yielded $R_{cr} = 0.8$ nm. Schiltges and Dual later extended this approach to consider micro-scale components under both tensile and torsional loads.[188] As before, the failure criterion was defined in terms of R_{cr}. R_{cr} for the tensile and torsional specimens were found to be 0.8 nm and 5.9 nm, respectively. The first result was not surprising, as it was in good agreement with results from their previous work. The second result was unexpected, however, as the two values for R_{cr} should theoretically be the same. The discrepancy was attributed to non-idealities in the experimental setup (i.e., the specimens were not *purely* in tension and torsion).

C. Test temperature, environment, and loading rate

1. Temperature

The fracture strength of small-scale SCS components is highly dependent on temperature T and because many of these components are now being required to perform at elevated temperatures,[205,206] a quantitative understanding of the relationship between the two is of critical importance. The most significant mechanical transition in SCS with temperature is the onset of plasticity. At room temperature under unconstrained tensile conditions, the large (2.1 eV) activation energy of dislocation motion prevents dislocation slip. In bulk SCS, dislocation plasticity begins at temperatures higher than about 525 °C, with the exact transition temperature depending on the orientation of the Si and the applied deformation rate.[207] The BDT in bulk SCS is a sharp transition from a toughness ≈ 1 MPa m$^{1/2}$ below the transition temperature to >3 MPa m$^{1/2}$ above the transition temperature.[208]

Initial studies on the mechanical behavior of SCS components at elevated temperatures were conducted well above the bulk BDT temperature.[198,209,210] For instance, Pearson *et al.* studied the deformation and fracture of both SCS whiskers grown from vapor and SCS rods cut from bulk Si at $T = 25 °C$ and $T > 600 °C$.[198] At $T = 25 °C$, the micro-scale rods deformed elastically up to fracture, with the final strengths varying by $4\times$ depending on the specimen size. On

the other hand, at $T = 800 °C$, the rods deformed plastically, with an upper yield stress of 110 MPa and a lower flow stress of 40 MPa, both of which were less than the room temperature σ_f. Fruhauf *et al.* later showed that the upper yield stress and lower flow stress of $\langle 110 \rangle$ and $\langle 100 \rangle$ SCS beams were dependent on the testing parameters at $T > 650 °C$; both decreased with increasing temperature and increased with increasing deformation rate.[209,210] In addition, the yield and flow stress values for the $\langle 100 \rangle$ beams were found to be less than those of the $\langle 110 \rangle$ beams, most likely due to a difference in the number of slip systems working in each orientation (eight for $\langle 100 \rangle$ and four for $\langle 110 \rangle$).

More recent studies have focused on investigating plastic deformation in SCS components at intermediate temperatures (temperatures ranging from 25 to 300 °C), and more specifically, elucidating the role of specimen size on the BDT temperature. At the *micro-scale*, Nakao *et al.* used an on-chip tensile testing method to demonstrate nonlinear tensile stress–strain behavior at temperatures as low as 400 °C.[60] The measured σ_f was 5.73 GPa at room temperature, but drastically decreased to 1.84 GPa at 500 °C. SEM observations of the fractured specimens showed the classic signs of brittle fracture at $T = 25 °C$ (i.e., crack propagation perpendicular to the loading direction) and plasticity at $T = 500 °C$ (i.e., slip surfaces along the (111) planes), but a completely different behavior at the onset of the nonlinear tensile stress–strain behavior at $T = 400 °C$ (i.e., a "t-shaped" crack indicative of dislocation motion). Namazu *et al.* reported BDT temperatures as low as 100 °C for *nano-scale* SCS components using an AFM-based bending test.[197] The AFM bending tests used four types of SCS wires, with widths of 200, 300, 550, and 800 nm. The stress–strain behavior was linear to fracture at room temperature, but exhibited non-linear behavior at temperatures ranging from 100 to 300 °C. The size of the non-linear region increased as the temperature increased and as the specimen size decreased. Because the test method allowed a statistically relevant number of samples to be measured, the authors were also able to evaluate the strength distributions for each test condition. As shown in Fig. 19(a), σ_f decreased with test temperature, mainly because the SCS slip systems were more readily activated at elevated temperatures. Moreover, the Weibull modulus was found to decrease with an increase in specimen size and temperature, indicating more scatter in the strength data. To further elucidate the size and temperature dependence on the plastic deformation, the critical resolved shear stress τ_c was also calculated from the yield stress as shown in Fig. 19(b). τ_c decreased with size and temperature and ranged from 4.2 to 7.2 GPa; these values are ten times greater than those observed in milli-scale specimens due to a reduction in the number of defects in the SCS wires.[211] Finally, AFM was used to determine the number of slip lines generated on the top of the specimen just prior to fracture as a function of size and temperature. As expected, the number of slip lines increased as the specimen size decreased and the temperature increased; the former dependence was due to greater shear stresses in the smaller wires, whereas the latter dependence was due to an increase in the
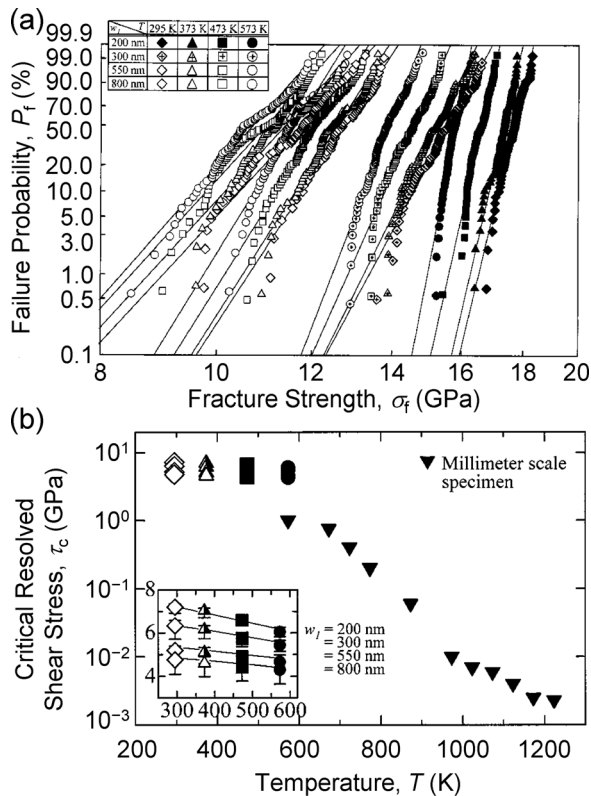
FIG. 19. (a) Strength distributions and corresponding two-parameter Weibull failure probability fits as a function of temperature for SCS. The fracture strength was inversely proportional to the test temperature, mainly because the SCS slip systems were more readily activated at elevated temperatures. (b) Critical resolved shear stress as a function of temperature. The critical shear stresses were inversely proportional to size and temperature and ranged from 4.2 to 7.2 GPa. Reprinted with permission from Namazu et al., J. Microelectromech. Syst. **11**, 125 (2002). Copyright 2002 IEEE.

frequency of activation over energy barriers to dislocation motion at higher temperatures.

In localized volumes, such as at the tip of a crack, the BDT temperature may be even lower than those reported above: in follow-up work, Nakao et al. showed that the apparent toughness of FIB-notched 4 μm-thick SCS abruptly increased from $\approx$1.3 MPa m$^{1/2}$ to >2.1 MPa m$^{1/2}$ at a transition temperature of 70 °C.[59] Recently, Chang and Zhu also showed reduced BDT temperatures for SCS nanowires using a MEMS device with an on-chip heater; the stress-strain behavior for a 60 nm diameter nanowire suggested a transition between 89 and 126 °C.[212]

2. Environment

The degrading effect of environmental conditions on the mechanical behavior of SCS can be indirectly inferred from several studies. For instance, Alan et al. examined the strength distributions of SCS notched nanobeams with hydrogen-terminated surfaces as a function of the number of days after release and found that σ_f decreased by 30% over the first 23 days after release.[176] Unexpectedly, m did not vary with time, indicating that only σ_θ, and not the form of the σ_f distribution, was sensitive to the environmental conditions. It was noted that this observation is particularly concerning because it is common practice to finish the MEMS

process with a HF-release step that renders components susceptible to this subsequent degradation. The degrading environmental effect was mitigated by terminating the surfaces of the nanobeams with a CH$_3$ monolayer. In fact, the methyl-terminated beams were 10% stronger than the hydrogen-terminated after 3 days and showed no systematic decrease in σ_f with time. The slow degradation of SCS components may be related to the rather surprisingly slow oxidation rate of Si: in an oxidation study of (111) SCS surfaces with H-termination, Neuwald et al. found that it takes $\approx$33 days at room temperature in 100% relative humidity (RH) for H-terminated surfaces to form a complete monolayer of oxide.[213] However, 1–2 nm diameter oxide nuclei develop randomly across the surface almost immediately, which may mimic surface roughness in their ability to form stress concentrators[174] and thus explain the drop in σ_f over 3 days.

More direct evidence for the susceptibility of small-scale SCS components to failure in harsh environments comes from an area of study beyond the scope of this work: SCS fatigue. However, a brief summary of fatigue in micro- and nano-scale SCS components is presented here for completeness, with a particular emphasis on the role of environment in the failure process (a more detailed assessment of fatigue in Si films can be found elsewhere[214]). In the early 1990s, Connally and Brown used an electrostatically actuated microcantilever (150 μm wide $\times$ 235 μm long) with a precrack 2–3 μm deep across the thickness to study time-dependent crack growth in SCS components.[43,44] The resonance frequency of the cantilever decreased with time, which was interpreted as a measure of subcritical (stable) crack growth in the oxide layer; the rate of frequency change also decreased with time, which was associated with a reduction in crack-growth rate with increasing crack length. The authors believed that water played a strong role in the crack initiation and propagation process, as the resonant frequency remained constant in dry air, but decreased dramatically in wet air. Tsuchiya et al. later used SCS resonators to show that testing environment affects both fracture strength and fatigue life.[127,128] In terms of strength, it was shown that σ_f at high RH is 10% greater than that at low RH,[127] and more recently, that σ_f in air is only 70%–80% of that in vacuum.[128] In terms of fatigue, lifetimes were significantly reduced for specimens tested in environments with water vapor and oxygen, with the effect of water vapor much more pronounced than that of oxygen. Komai et al. used SCS beams subjected to pure bending and three-point bending to study the influence of water on fatigue lifetime.[215,216] In laboratory air, no fatigue damage was observed up to 5 $\times$ 10^4 cycles, as determined by AFM images of fatigued specimens. However, when the fatigue tests were conducted in water, the lifetimes were drastically reduced and nanoscale grooves were detected via AFM about 70° to the $\langle 112 \rangle$ longitudinal direction, probably corresponding to cracking along a {111} plane. The authors concluded that a synergetic mechanism of fatigue loading and the water environment caused the crack formation on the {111} plane, which eventually led to failure of the component. Pierron and Muhlstein studied the effect of service environment on the fatigue lifetime of electrostatically actuated SCS resonators.[217] In laboratory air (50%

RH), the fatigue lifetime increased from 5.0×10^2 to 7.5×10^{10} cycles as the applied stress decreased from 3.4 to 2.2 GPa. In contrast, none of the specimens tested in moderate vacuum of 10 Pa–40 Pa at stress amplitudes between 2.5 and 3.0 GPa failed up to $\approx 10^{10}$ cycles. Furthermore, the RH was found to have a dramatic effect on the fatigue damage accumulation, with the accumulation rate at 50% RH an order of magnitude larger than that at 25% RH and virtually negligible in moderate vacuum. The authors described the fatigue process as a surface phenomenon, in which "reaction-layer" fatigue leads to sub-critical cracking in the surface oxide layer; the initiation and growth of these cracks via environmentally and cyclically assisted processes eventually results in unstable crack growth and fracture.

3. Loading rate

Although a significant amount of research has focused on the fracture strength of SCS in quasi-static conditions, very little work has considered SCS dynamic fracture strength. Unlike quasi-static conditions, under shock loading a component may not be in stress equilibrium but instead be governed by elastic wave propagation, reflection, and interaction. As a result, the dynamic σ_f may differ from its quasi-static counterpart, making dynamic determination important to the development of components required to survive high-g shock and drop loading conditions (e.g., accelerometers and gyroscopes). In miniature components, shock loading can be particularly problematic, as the impulse frequencies can excite resonant modes in a device.

At the macro-scale, recent work has shown that non-linear surface acoustic wave (SAW) pulses can generate steep impulse shocks with tensile stresses that exceed the σ_f of most brittle materials, e.g., fused silica and SCS, leading to fracture without a precrack or notch in the specimen. For example, Lomonosov *et al.* used a pulsed Nd:YAG laser to excite nonlinear SAW pulses in a SCS strip with length of ≈ 8 mm and width of $\approx 10\,\mu$m.[218,219] The sample surface was covered with an absorbent aqueous suspension layer, leading to overheating and explosive evaporation when irradiated. This resulted in a strong transient normal force on the surface, which generated SAW pulses with large amplitudes. From the spatial-temporal distribution of the stress at the cracking threshold, dynamic σ_f ranging from 0.8 to 1.6 GPa were extracted for SCS. SEM observations revealed that the SAW pulses traveled in both the [$11\bar{2}$] and [$\bar{1}\bar{1}2$] directions, but that the pulse formed in the [$\bar{1}\bar{1}2$] direction was more likely to induce fracture along the weakest SCS cleavage plan due to its tensile nature.

Instead of using SAW pulses to generate tensile stresses in blank SCS strips, other studies have focused on dynamic testing methods based on actual micro- and nano-scale SCS components; such components can be fabricated next to a device of interest, and thereby include the effects of processing conditions on the dynamic strength. Sharon *et al.* investigated the dynamic failure response of MEMS devices using both in-plane and out-of-plane bending test specimens fabricated from SOI wafers with photolithography and DRIE.[220] Both sets of specimens were subjected to acceleration pulses

along their critical loading directions using a shock tower. In the in-plane configuration, the longest cantilever beams were expected to fail first, as they experience the largest stresses at a given acceleration level. However, it was found that the shortest cantilever beams failed instead at 5000 g acceleration pulses along their critical loading directions. FEA simulations suggested that the unexpected failures were due to resonant excitation, and not overstressing, of the shortest beams. The absence of in-plane device failure from overstressing indicated that the dynamic σ_f of DRIE-processed SCS exceeded 1.1 GPa. In the out-of-plane configuration, shock tests on multiple specimens yielded Weibull statistics for dynamic loading conditions; the resulting values for m and σ_θ were 6.5 and 1.2 GPa, respectively. Post-test inspections revealed that failures occurred along {111} planes.

V. POLYSILICON FRACTURE STRENGTH

One of the earliest detailed studies of the parameters that affect the fracture strength of microfabricated polysilicon was reported over two decades ago.[121] In that early study, processing conditions were intentionally varied to alter grain size over the range of 50–500 nm and it was found that the coarsest grain polysilicon was 20% stronger than the finest grain polysilicon, an effect attributed to "stronger grain boundaries suppressing crack migration."[121] Since that time, there have been hundreds of articles that touch on the topic of strength of polysilicon, although the topic is showing signs of maturation as evidenced by the normalized publication rate shown in Fig. 2. This section reviews many of the most salient findings to date in some of the key studies on the fracture strength of polysilicon.

A. Processing conditions

As discussed earlier, the strength of polysilicon components is governed by the interplay between a process- or environment-induced extrinsic flaw population and intrinsic material resistance to crack propagation from this flaw population characterized by the toughness. Processing has its most obvious and dramatic effect on the flaw population, but the polysilicon deposition method can also affect the material toughness. The effect of processing on both the critical flaw population and material toughness are discussed in this section. While there can be many types of defects present in Si, the most common "defects" in polysilicon are grain boundary grooves. These cusp-like surface crevices at grain boundaries are thought to form either by preferential etching of the high-energy grain boundaries[133] or by thermal grooving during high-temperature annealing steps.[221,222] Both have the same thermodynamic origin: all grain boundaries in a pure single-phase material cost more from an energetic perspective than the grain interiors. Chemical etching and temperature provide the kinetic pathway by which the grain boundary material is removed and the material internal energy reduced.

1. Etching, galvanic corrosion, and surface oxides

Etching is widely used in Si microfabrication as a means to remove sacrificial material. While HF is the most commonly used etchant that preferentially attacks SiO_2 over Si, a
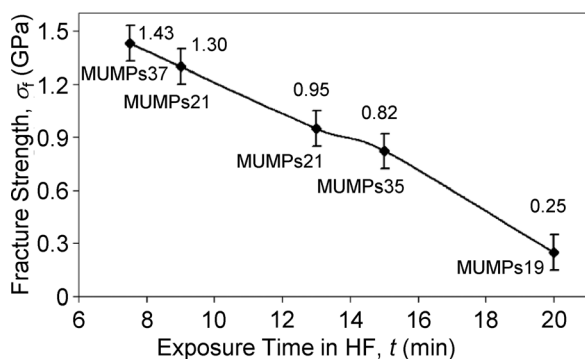
FIG. 20. Fracture strengths of polysilicon tensile test specimens fabricated with the PolyMUMPs process as a function of time in HF. The fracture strength decreased from 1.43 to 0.25 GPa as the etch time increased from 7 to 20 min. Two possible explanations were given for this trend: (i) accelerated etching of the surface oxide or (ii) electrochemically enhanced galvanic corrosion due to the presence of the metallization layers. Reprinted with permission from Chasiotis and Knauss, J. Mech. Phys. Solids **51**, 1533 (2003). Copyright 2003 Elsevier.

wide variety of etchants can be used for various anisotropic and sacrificial layer removal steps. Each of these etchants ultimately governs the remnant surface topography of the liberated Si structures. Chasiotis and Knauss[133] etched polysilicon from the PolyMUMPs process in 49% HF for periods ranging from 7 to 20 min, and showed that σ_f decreased by 83% over this time range from a strength of 1.43 GPa to a strength of 0.25 GPa as shown in Fig. 20. They attributed this small σ_f to a crust of intergranular surface cracks that grew in prevalence and size as the etch time increased. However, it was noted that the (short) etch times were insufficient to explain the rapid formation of such pronounced defect networks by direct chemical attack alone. Two possible explanations were offered: either accelerated etching of the surface oxide or electrochemically enhanced galvanic corrosion due to the presence of metallization layers. The galvanic corrosion argument was later supported by Miller *et al.*, in a detailed analysis of the galvanic couple that forms during etching of Si MEMS with gold metallization layers.[223] The galvanic corrosion process due to etching in 49% HF in the presence of a metallization layer led to the formation of a thick, pitted, surface oxide layer, with preferential attack of the grain boundaries, that caused a precipitous loss of strength,[200] comparable to that reported by Chasiotis and Knauss.[133] However, when the same devices were fabricated without a gold metallization layer there was essentially no loss in σ_f even after 90 min of exposure to the HF solution. Miller *et al.* also noted a concomitant drop in apparent E due to the galvanic corrosion process and connected both σ_f and apparent E decrease to the morphology of the thick surface layer of pitted, crevice-like features formed during galvanic corrosion.[200] The thick, defected oxide layers that form by galvanic corrosion of polysilicon have also been linked to diminished fatigue performance.[224]

In a direct side-by-side comparison of σ_f using both dog-bone tensile bars and resonator devices, Alsem *et al.* showed that SUMMiT V polysilicon was 25%–50% stronger than PolyMUMPs polysilicon.[225] It was noted that PolyMUMPs polysilicon had increased root mean square surface

roughness (14 nm vs. 10 nm) and a much thicker surface oxide (20 nm vs. 3.5 nm) than SUMMiT V polysilicon. While both processes utilize films fabricated by LPCVD, there are many other differences between the two processes that could have led to the disparity in surface condition and ultimately in mechanical response. Some of the details of these proprietary processes are undisclosed, such as the annealing cycles to manage residual stress. However, there is a clear difference in the release etching condition: PolyMUMPs is etched for 3 min in 49% HF, whereas SUMMiT V is released for 90 min in a HF:HCl solution with a perfluorodecyltrichlorosilane monolayer applied prior to exposure to air. It is perhaps revealing to note that fractography of SUMMiT V polysilicon components reveals sites of crack initiation invariably on the sidewalls or edges (corners)[226] as they have greater roughness than the top or bottom surface, whereas Chasiotis suggests that the largest flaws for PolyMUMPs may reside on the top (or bottom) surface.[133]

2. Annealing and grain size

To explore the role of grain size on σ_f, Boyce *et al.* processed polysilicon by two different deposition routes:[141] one that utilized LPCVD deposition at 580 °C to form a "coarse-grained" polysilicon with an average grain size of $\approx$400 nm as shown in Fig. 21(a) and another that alternated 100 nm layers of polycrystalline and amorphous Si followed by an anneal to produce a "fine-grained" polysilicon with an average grain size of $\approx$150 nm as shown in Fig. 21(b). The fine-grained polysilicon was 60%–90% stronger than the coarse-grained polysilicon as shown in Fig. 21(c). This dramatic strengthening effect was attributed to the significantly reduced surface roughness due to suppressed grain-boundary etching in the fine-grained material.

Tsuchiya explored the role of crystallization temperature and ensuing grain size on the strength of polysilicon.[128] Starting with amorphous Si, films were crystallized at temperatures ranging from 600 to 1000 °C. The resulting polycrystalline tensile bars had σ_f ranging from 2.7 to 3.7 GPa depending on the crystallization temperature. As in the work of Boyce described in the previous paragraph, the greatest σ_f values were associated with the highest crystallization temperature, which also produced the finest grain sizes. Tsuchiya also commented that the grain size may have an indirect role on strength by affecting the location and extent of grain boundary "pitting." Tsuchiya compared the polycrystalline materials to the precursor amorphous Si strength and found that the amorphous material exhibited markedly smaller σ_f, <2 GPa. This result is somewhat surprising, as the amorphous material is free of grain boundaries that could serve to form flaws due to differential etching or thermal grooving. Tsuchiya commented that the HF sacrificial etching produced larger defects in the amorphous material compared to the polycrystalline material.

3. Doping

Polysilicon MEMS devices are commonly doped with either *p*-type Boron (B) or *n*-type Phosphorus (P) to increase the conductivity. In one of the first studies on the effect of
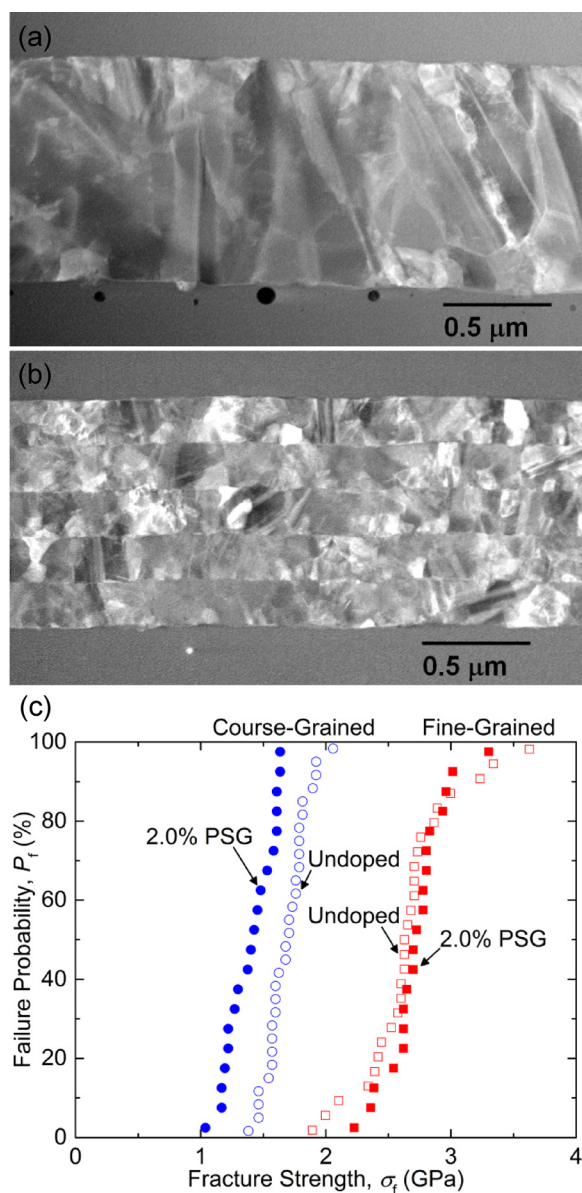
FIG. 21. TEM images of (a) course-grained and (b) fine-grained polysilicon films fabricated with the SUMMiT V process. (c) Strength distributions for undoped and doped course-grained and fine-grained polysilicon films. The microstructure was found to have a significant impact on strength; the fine-grained films were 60%–90% stronger than the coarse-grained films. In contrast, the phosphorous doping had a less pronounced effect, lowering the characteristic strength by only 16% for the coarse-grained film and having little or no effect on the fine-grained film. Reprinted with permission from Boyce et al., Acta Mater. **58**, 439 (2010). Copyright 2010 Elsevier.

doping on fracture strength, Biebl and von Phillipsborn reported that B had no effect on σ_f but P reduced σ_f by 25%.[122] Tsuchiya et al. showed that P not only reduced the mean fracture strength of polysilicon by $\approx$10%, but also reduced the variability in strength (greater two-parameter Weibull modulus).[127] There are two common explanations for the reduction of σ_f of polysilicon by dopants: (i) the segregation of dopants to the grain boundaries leads to an accelerated local attack of the boundaries and more pronounced surface flaws and (ii) the dopants decrease the intrinsic toughness of the material. Son et al. showed that both B and P doping by ion implantation reduces the strength and

toughness of polysilicon.[54] Recently, Bergman and Sherman showed that under low speed dynamic crack propagation conditions, B impurities induce atomic-height jogs in the crack path.[227] However, a direct comparison to intrinsic Si was not made, and the extent of toughening (if any) from doping is unclear. Indentation-strength studies on SCS and polysilicon show no effect of dopants on σ_f.[1]

4. Toughness

The toughness of polysilicon can be affected by crystalline factors such as the material chemical bond makeup (to change the energy/bond, u_B above) or by microstructural factors (to change the local mechanical energy release rate, G above). As noted in the previous paragraph, substitutional dopants (B, P) do not appear to have a great or clear effect on toughness and there are relatively few studies that examine the toughness of chemically modified polysilicon. However, Zbib and Bahr demonstrated that the toughness of LPCVD-deposited granular polysilicon can be reduced substantially, down to a claimed 0.6 MPa m$^{1/2}$, by incorporation of hydrogen (H) in the Si through deposition in a H-rich atmosphere.[228] A simple explanation in this case is that the incorporated H disrupted the Si-Si bonding by forming terminal, non-bonding, Si-H complexes such that the Si-Si bonds/area (n_A above) was decreased. Most studies of toughness of polysilicon focus on the role of the polycrystalline grain structure in governing toughness, although, unlike engineered ceramics such as yttria-stabilized zirconia or polycrystalline alumina,[229,230] there are no reports for polysilicon of significant microstructural modifications that improve the toughness substantially, and the toughness value is typically in the vicinity of 1 MPa m$^{1/2}$.

The presence of grains and grain boundaries in polysilicon does more than just serve as a source of cusp-like stress concentrating defects that facilitate crack initiation. As noted above, the elastic anisotropy-induced stress heterogeneity from grain to grain and within grains serves to both distort the symmetry and alter the magnitude of stress-fields around flaws and cracks.[28,29,31] When the crack is large compared to the grain size, the heterogeneities are somewhat mitigated, but in the case of polysilicon MEMS, crack tips rarely interact with a large number of grains simultaneously. Ballarini et al. noted that the heterogeneous microstructure around cracks in polysilicon largely affected the local mechanical energy release rate field through the influence of the few grains surrounding the crack tip; the implication is that there is a considerable crack-size effect as crack or flaw sizes approach the material grain size.[31]

In addition, different orientations within grains and different grain boundary misorientations in polysilicon have different interatomic bond densities, and, as considered above, therefore have different intrinsic fracture resistance values. As a consequence, a crack propagating transgranularly may arrest at grain boundary if the boundary or adjacent grain orientations are such that the local condition for fracture is not met. Such crack arrest at grain boundaries has been observed experimentally, for example, in Refs. 32, 33, and 49; the similarity between the SIF required to propagate

a crack across a grain boundary and the perceived upper bound to the toughness of polysilicon, both about 1.2 MPa m$^{1/2}$, has already been noted. However, as also noted, polysilicon can exhibit a range of toughness values within a single study, ranging from 0.84 to 1.2 MPa m$^{1/2}$ in the study of Cho *et al.*, for example.[49] The lower bound in this study is very close to the toughness values for that of a random polycrystal, suggesting that if a crack encounters appropriately oriented grains there is no arrest at grain boundaries. In contrast, Foulk *et al.* used cohesive zone fracture modeling to explore the resistance to a propagating crack as it approached a grain with sufficient toughness to resist transgranular fracture and an inclined grain boundary that could force crack deflection as well as grain bridging.[231] In some scenarios explored in this study, the presence of such an oriented grain and grain boundary was found to increase the local toughness by a factor of two to three. In contrast, Corigliano *et al.* conducted polycrystal elasticity finite element simulations of crack propagation in polysilicon and showed the influence of local grain morphology and anisotropy on crack deflection, but little effect on resistance to crack propagation.[64] Observations of crack deflection and grain-boundary arrest stemming from the polycrystalline microstructure of polysilicon have been made,[48] but there are few conclusive observations of grain-localized ligamentary bridging or frictional interlocking as observed in polycrystalline ceramics (e.g., alumina) with thermal expansion anisotropy,[230] suggesting that such energy dissipation mechanisms are not dominant in polysilicon.

An implication of a lower bound to the toughness of polysilicon is that the resulting component σ_f range should also have a lower bound, assuming that there is an upper limit on flaw size. As noted, the commonly used two-parameter Weibull distribution carries the implicit assumption that there is a non-zero probability of fracture for all positive applied stresses. This seems a dubious assumption, given the bounded nature of the toughness and of the flaws. While the original Weibull distribution allows for a third parameter, the cut-off stress below which there is zero probability of failure, reliable determination of this cut-off stress is often difficult in practice due to limited datasets. A high-throughput test method that permitted over 1000 nominally identical tensile tests on polysilicon MEMS has demonstrated the existence of a non-zero threshold strength for polysilicon,[142] as shown in Fig. 22. This result, now confirmed by an independent test method,[84] suggests that σ_{th} is $\approx$1.4 GPa for the poly3 layer of SUMMiT V polysilicon. This cut-off strength appears to be reasonably consistent with known limits of toughness and AFM characterization of flaw populations.[84] Such a cut-off strength is important in engineering design, as it provides a practical lower-bound strength value below which no components (in that size range, and with that defect population) should break.

B. Component size and geometry

1. Size

The most cited work on the size effect in the strength of polysilicon is the 1998 work by Tsuchiya *et al.*[127] In this
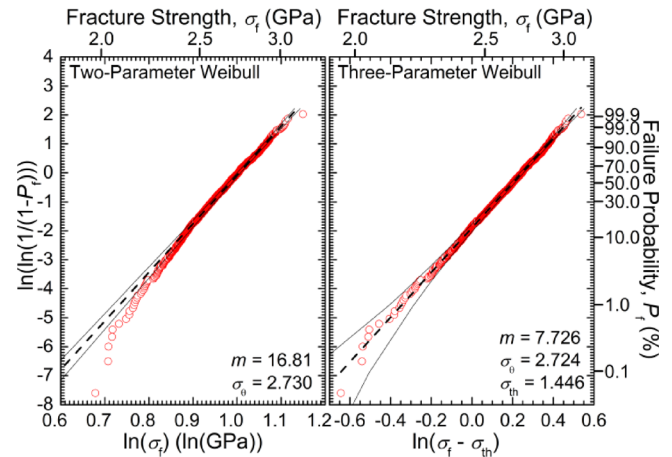

FIG. 22. Strength distributions for 1008 nominally identical tensile tests on polysilicon films fabricated with the SUMMiT V process. The axes were chosen such that the two-parameter and three-parameter Weibull fits (dashed black lines) should appear linear within the 95% confidence bounds (solid black lines). The high-throughput test method demonstrated the existence of a non-zero threshold strength for polysilicon; for the poly3 layer, the threshold value was found to be $\approx$1.4 GPa. Reprinted with permission from Boyce, Exp. Mech. **50**, 993 (2010). Copyright 2010 Springer.

work, the width of the tensile gauge section was varied from 2 to 5 μm and the length of the gauge section was varied from 30 to 300 μm, with a constant gauge thickness of 2 μm. Over this range of specimen sizes, a 10-fold reduction in gauge length increased the mean σ_f by 14%–35%, whereas a 2.5-fold reduction in gauge width increased the mean fracture strength by only 4%–10%. Fractography indicated that the failure originated along one of the four edges of the tensile gauge section, so it is surprising that gauge width had any influence at all. In another highly cited work that followed shortly after the Tsuchiya work, Sharpe *et al.* demonstrated an increase in σ_f of $\approx$38% from $\approx$1.2 to 1.65 GPa by reducing the gauge surface area by $\approx$10^3.[130]

In 2003, LaVan led an inter-laboratory study among five research groups to evaluate the tensile strength of SUMMiT IV^{TM} polysilicon.[232] There were effectively two different specimen designs, and each group had their own approach to testing the designs, but all specimens were fabricated by the same SUMMiT IV method and released at the same time to allow a direct comparison of the results from the different testing methods. The specimens fabricated on the study die ranged in size by a factor of more than 100 in gauge surface area. One of the key results suggested that there was very weak correlation between gauge surface area and σ_f within any given test method. The result highlights the discrepancies that existed at that time between test methods. The elevated σ_f levels measured by the "L" test method relative to the other methods were later attributed to the superposition of frictional forces in the strength measurement.[83]

In 2007, Boyce *et al.* explored the size effect in several different polysilicon layers of the SUMMiT V^{TM} process.[83] The study used a single test technique to interrogate a variation in gauge surface area that spanned over a factor of 100. Over this large range, there was a clear trend of increasing σ_f with decreasing gauge surface area, as shown in Fig. 23.
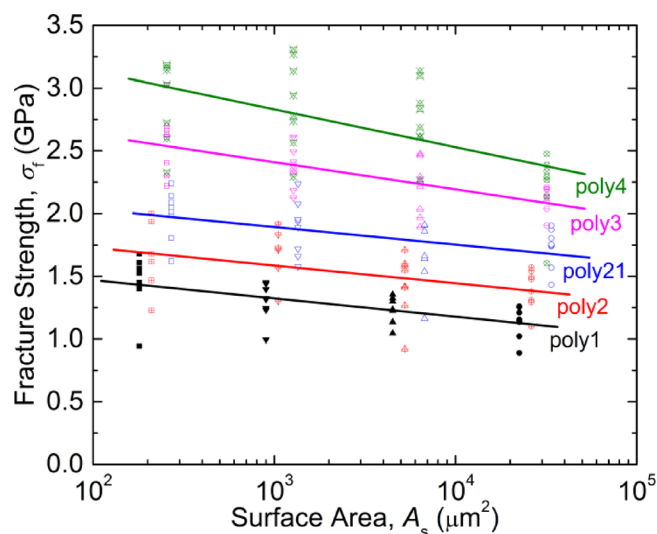
FIG. 23. Fracture strengths of polysilicon tensile test specimens fabricated with the SUMMiT V process as a function of layer type and component size. The study used a single test method to interrogate a variation in gauge surface area that spanned more than two orders of magnitude. Over this range, there was a clear trend of increasing strength with decreasing surface area. Reprinted with permission from Boyce *et al.*, J. Microelectromech. Syst. **16**, 179 (2007). Copyright 2007 IEEE.

The slope of the trend was reasonably consistent for each of the polysilicon layers, although the average σ_f of each layer was distinctly different. The Weibull moduli for each of the different layers, from Eq. (41), were two to three times greater than the *m* estimated by direct measurement of the σ_f distributions, from Eq. (42).

Taken together, there is remarkable similarity between the various size effect studies on microfabricated Si. For every 10-fold reduction in surface area, there is roughly a 10%–20% increase in the average σ_f of polysilicon. It is clear from these works that the smallest stressed Si structures will have exceptionally large σ_f, approaching the theoretical limit. The theoretical ideal cleavage strength of SCS along ⟨111⟩ crystallographic directions is 21–23 GPa.[201,202] Polycrystals, however, would have reduced apparent σ_f due to two related factors: (1) the elastic anisotropy of neighboring grains leads to local stresses in some grains elevated above the far-field applied stress, (2) as a result of this incompatibility at grain boundaries and triple junctions, there can be pronounced stress singularities.[233–235]

2. Geometry

One corollary to the size effect is that stress concentrating features such as holes and notches appear *stronger* than the stress concentration factor itself would suggest. Not only does the SIF have to be taken into account (Eq. (19) or Eq. (20)) but so does the effective reduced sampling volume or area of the hole or notch. In polysilicon, the reduced sampling area not only results in a size effect but also reduces the number of grains and grain boundaries that are significantly loaded. For example, in a homogeneously stressed microscale polysilicon tensile bar roughly 10^4–10^8 grains are stressed, whereas in the presence of a 1 μm radius feature, only a few grains are significantly stressed. Proper

accounting of the notch effects in polysilicon failure is particularly important, as nearly all MEMS devices suffer the greatest stresses at a geometric feature such as a corner. The increased σ_f and increased variability at notch features has been demonstrated and analyzed in several prior studies, e.g., Refs. 84, 131, and 236.

Chasiotis and Knauss evaluated the effect of two-dimensional circular and elliptical perforations in the center of a polysilicon tensile bar with radii of curvature ranging from 1 to 8 μm and nominal stress concentration factors of 3–8.[134] They showed that after accounting for the SIF, samples with a 1 μm radius perforation were still 50% stronger than samples with an 8 μm radius. Moreover, while a detailed statistical analysis was not performed, the range of σ_f values was roughly twice as wide for the 1 μm radius samples compared to the 8 μm radius samples.

In the presence of particularly sharp geometric features, the principles of size-scaling analysis become dubious. A basic tenant of the Weibull size-scaling analysis is that the stressed volume is always large enough to sample from the distribution of strength-limiting flaws. The strength-limiting flaws have a distribution of sizes, but they also have a spatial periodicity or distribution (given by λ above). For example, Reedy considered grain boundary cusps as the population of strength-limiting flaws in SUMMiT V polysilicon.[235] These grain boundary cusps are spatially distributed at the edge of every grain boundary, roughly 300–400 nm apart. While a tensile bar may sample many hundreds of cusps, a particularly sharp stress concentration comparable to or smaller than the cusp spacing may not sample any, and may be controlled by a different population of secondary flaws. The spacing of strength-limiting flaws establishes an intrinsic material length scale, i.e., a minimum dimension to sample a representative volume element (RVE) of material. In terms of the area scaling considered in Eq. (38), the RVE is $1/\lambda^{3/2}$. Le *et al.* notes that when the stressed volume is comparable to or smaller than the RVE, the σ_f distribution is no longer Weibullian, but has a Gaussian core with a Weibullian tail.[98] In the study by Reedy,[235] it was found that the σ_f of a notch of comparable size to the strength-limiting flaw population was underpredicted by Weibull size analysis.

A particular geometric feature that is often overlooked, but present in any MEMS design, is the attachment point between layers. This can be the attachment between a single MEMS layer and the substrate, or an attachment point between two layers in a multilayer MEMS process. Unlike in-plane geometric features that are rounded either intentionally or by lithographic resolution limitations, the out-of-plane stress concentrations at attachment points are often quite sharp. An example from the SUMMiT V process is shown in Fig. 24. In that example, a tensile bar failed unintentionally at a relatively thick region involving an attachment point of a Si overlayer instead of at the much thinner gauge section of the tensile bar. The TEM image shows that the stress concentrating feature is clearly smaller than the microstructural features and only a single grain boundary would experience significant stress. In an unpublished study on polysilicon, a set of tensile bars were manufactured with an Si overlayer attached in the middle of the gauge section,
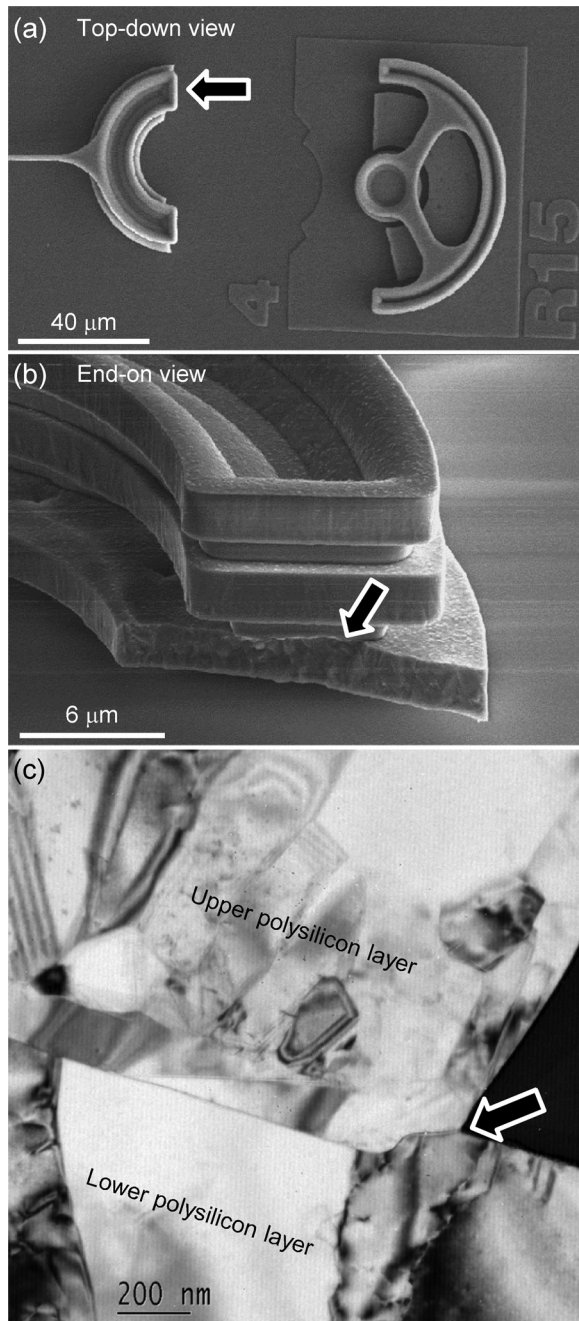
FIG. 24. (a) Top-down and (b) end-on SEM images of a polysilicon tensile bar that failed at an attachment point instead of in the gauge section. (c) TEM image of the interface, showing that the stress concentrating feature is clearly smaller than the microstructural features.
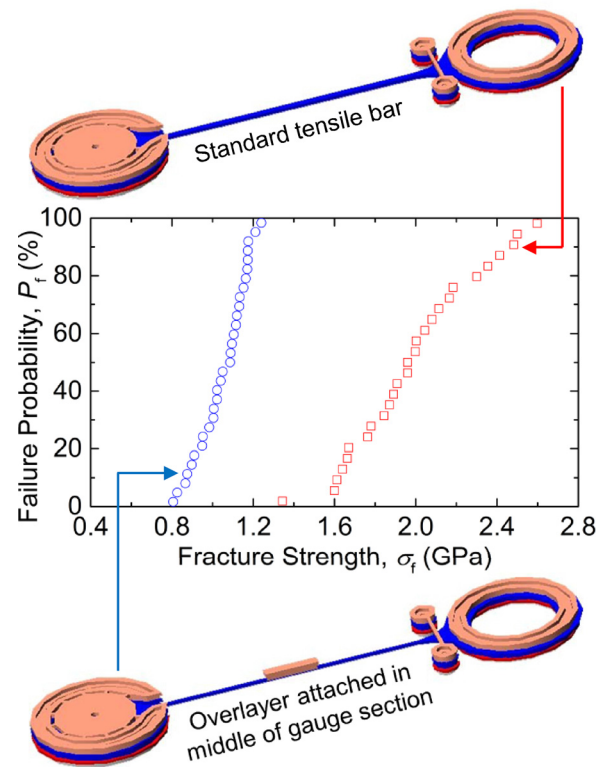

FIG. 25. Strength distributions for standard tensile bars and tensile bars with a Si overlayer in the gauge section, both fabricated with the SUMMiT V process. The presence of the Si overlayer reduced the effective strength of the underlying Si by a factor of two, most likely due to the sharp geometric features at the interface between the two layers.

as shown in Fig. 25. Using the SUMMiT V process, the gauge section was poly3 with an overlayer of poly4 (or poly2 with an overlayer of poly3). In a comparison to standard tensile bars, the presence of the overlayer reduced the effective σ_f of the underlying polysilicon by a factor of 2.

C. Test temperature, environment, and loading rate

Overall, the effects of temperature, environment, and loading condition on σ_f are not strongly sensitive to the microstructure of polysilicon, and therefore follow closely with the observations in Sec. IV related to SCS. In this

section, additional observations are drawn from the polysilicon literature, although these observations are broadly consistent with observations in the SCS literature.

1. Temperature

In some applications, polysilicon components are required to maintain structural integrity under non-ambient conditions, such as at high temperatures. Kamiya *et al.* made statistical measurements of the Weibull distribution of polysilicon in nitrogen gas at room temperature and 180 °C.[237] The polysilicon was ≈10% stronger at 180 °C, an effect attributed to the Nakao observation of increased apparent toughness at temperatures above 70 °C.[238] Over a wider range of temperatures, Boyce *et al.* examined the tensile strength of SUMMiT V polysilicon at temperatures ranging from ambient to 800 °C in nitrogen and air environments.[83] At temperatures above 200 °C in both air and nitrogen environments, the study showed a marked decrease in σ_f: at 600 °C, the polysilicon strength had decreased to less than 40% of its room temperature value. The observations suggested a BDT temperature in the vicinity of 400 °C, somewhat lower than observed for bulk Si. At 800 °C, the σ_f distribution of polysilicon in a nitrogen environment (<5 ppm O_2) was nearly identical to air, suggesting that oxidation was not a likely cause of the strength degradation. Moreover, the strength was recoverable after high temperature exposure: after the Si had been exposed to 800 °C for 1 h, and subsequently tested at room temperature, the
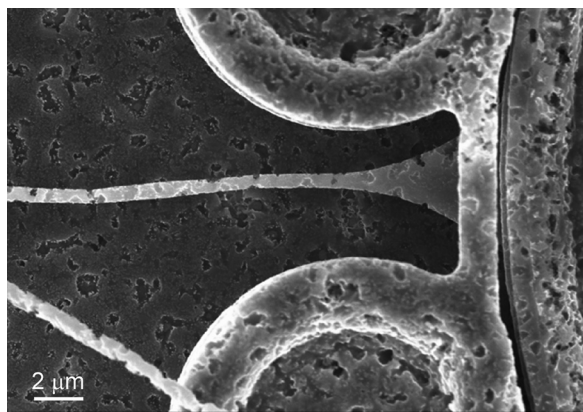
FIG. 26. SEM image of a SUMMiT V polysilicon component after a 1 h exposure to 1200 °C (87% homologous temperature) in an Ar atmosphere. This "thermal pitting" phenomenon has been observed in several inert environments including Ar, N$_2$, and vacuum in both polysilicon and SCS.

strength of the polysilicon returned to 90% of the baseline room temperature strength.

At even higher temperatures or very long exposure times, polysilicon appears to be susceptible to a thermal pitting phenomenon that can degrade the strength by imparting flaws that are larger than the native as-fabricated population. In a study attempting to study the creep behavior of polysilicon MEMS, even 20 min of 1000 °C annealing in an Ar atmosphere was shown to lead to substantial surface pitting, which catastrophically degraded σ_f. An extreme example of this degradation is shown in Fig. 26. This phenomenon has been confirmed in several "inert" environments including Ar, N$_2$, and vacuum; and has been confirmed in both polysilicon and SCS. However, at temperatures of 800 °C and below, the effect was not observed, even after a 10 h exposure. The pitting phenomenon, which may be related to localized sublimation, has important implications for high-temperature applications such as thermal actuators.

2. Environment

Polysilicon-based MEMS are typically thought to be rather stable in a room temperature inert gas or air environment. However, this is not always the case. Kamiya et al. compared the Weibull strength distributions of polysilicon in 80% RH laboratory air and dry nitrogen.[237] They found that the polysilicon was 6% stronger in dry nitrogen compared to 80% RH lab air, although an explanation for this effect was not given. Humidity has also been shown to have a marked effect on reducing the fatigue resistance of polysilicon (e.g., Refs. 237 and 239–242). This degrading effect of humidity has widely been attributed to a "reaction layer" process by which the surface oxide is thickened by cyclic loading, although this mechanism has been called into question by some.[243] There are at least four factors that could cause a surface oxide to degrade the strength of Si:

(1) The surface oxide is less tough than polysilicon. In air, the oxide is reported to have a toughness of ≈ 0.8 MPa m$^{1/2}$ or less,[244] whereas the polysilicon, as already discussed, toughness is typically reported in the range of 0.85 MPa m$^{1/2}$ to 1.2 MPa m$^{1/2}$.

(2) The surface oxide, when under residual stress, is known to be susceptible to stress corrosion cracking under ambient (humid) environments,[244,245] whereas polysilicon is thought to not suffer from stress corrosion cracking. As a result, thin film tension tests of microfabricated SiO$_2$ show that both the strength and toughness is substantially less in (humid) air than in vacuum.[246] The moisture-induced subcritical cracking of the surface oxide in polysilicon has also been attributed as the cause of high-cycle fatigue failure of polysilicon microsystems,[247] although this explanation has been called into question by some.[47]

(3) There are significant stresses caused by the large volumetric mismatch between the Si and its oxide: $\Omega_{Si}/\Omega_{SiO_2} = 20$ Å^3/45 Å^3, where Ω is the molecular volume.

(4) The enormous stresses that would result from epitaxial accommodation of the above volumetric mismatch are mitigated (but not entirely eliminated) by the formation of defects. Near-surface defects include dislocations, atomic ledges, and nanoscale cracks.

Section V A 1 addressed the issue of galvanic corrosion between polysilicon and metallization layers that occurs when MEMS devices are immersed in an ionic liquid during fabrication. However, polysilicon MEMS devices are rarely if ever used in a liquid medium and adsorbed water molecules on the surface of MEMS in a humid environment are likely insufficient to permit significant corrosion. However, on the application of significant voltages to polysilicon, such as during extended periods of electrostatic actuation, cathodic corrosion can occur. Hon et al. showed that under a constant voltage of 100 V and a RH of $\geq 57\%$ for 24 h, polysilicon can undergo significant cathodic degradation and dissolution of the cathode,[248] in addition to expected anodic oxidation, as shown in Fig. 27. This surprising cathodic degradation is postulated to be caused by reduction of adsorbed water and generation of hydroxide on the electrode surface such that the native oxide becomes unstable and forms
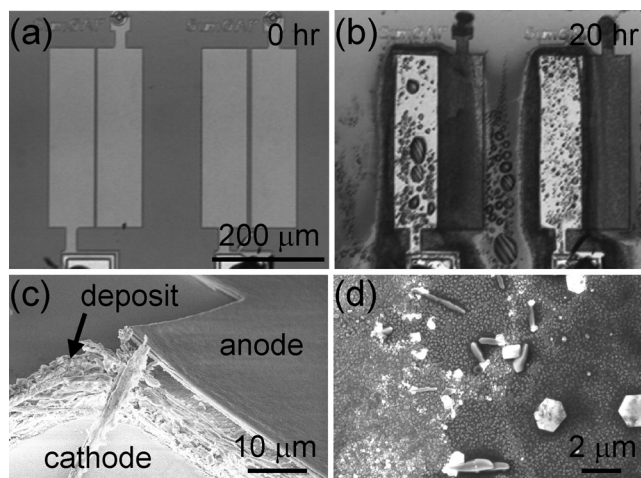

FIG. 27. Optical microscope images of asymmetric rectangular polysilicon electrodes fabricated with the PolyMUMPs process and exposed to -100 V at 97% RH for (a) 0 h and (b) 20 h. After 20 h, SEM images reveal (c) deposits around the cathode perimeter and delamination of the cathode and (d) crystals on the cathode where water condensation was present. Reprinted with permission from Hon et al., Sens. Actuators, A 145, 323 (2008). Copyright 2008 Elsevier.

soluble species in the alkaline environment. While the morphology of degradation has been studied,[248] to our knowledge there has not been a study of the evolution in mechanical properties of the polysilicon during cathodic corrosion. Both hydrogen-terminating and alkyltrichlorosilane-based self-assembled monolayers have been shown to reduce the rate of the corrosion mechanism.[249]

Under combined harsh conditions, such as elevated temperature and corrosive atmospheres, polysilicon has been shown to degrade. Michelutti *et al.* evaluated polysilicon resistivity and dynamic electrical noise under Ar, air, and chlorinated environments while in contact with aluminum at temperatures of 400 or 600 °C for up to 24 h.[250] While resistivity only shifted by >10%, power spectral density analysis showed that there was increasing noise at frequencies less than 1000 Hz. Here again, to our knowledge, there has been no study of the degradation in E and σ_f under these combined harsh conditions.

3. Loading rate

Shock fracture of polysilicon is more challenging and stochastic than SCS, as grain boundaries and elastic anisotropy within the polycrystalline grain structure give rise to complex internal elastic wave interactions and reflections.[251,252] However, most computational analysis of shock loading in MEMS treat the material as a homogeneous isotropic continuum. To evaluate devices for shock loading, most often a dynamic computational analysis is performed for the device geometry to determine the peak stresses during the shock, and those stresses are compared against measured quasi-static strength values to determine a safety factor.[253] In fewer cases, the performance of the polysilicon is actually measured in a dynamic loading environment.[254] Even in these combined experimental and computational studies, the polysilicon shock tests are often performed not on specially designed test coupons, but instead on devices that confirm their go/no-go functional reliability. These confirmation tests typically do not seek to characterize the threshold envelope of acceleration levels, frequencies, and durations that induce failure. For this reason, it is difficult to confirm the common assumption that measured quasi-static failure strengths still apply to the local stress values predicted for a shock loading profile. Moreover, quasi-static tests almost invariably sample a larger volume of material than the local regions excited by elastic wave interactions, and the unaccounted-for size effect renders the shock analysis conservative. In other cases, where a systematic experimental study was undertaken to explore a range of impact conditions, the "weak link" in the reliability of the MEMS devices was not polysilicon fracture, but impeded device performance due to device features interfering with one another (e.g., Ref. 255), stiction (e.g., Ref. 256), or package failure (e.g., Ref. 257). Moreover, device performance can be hindered by debris generation that occurs during service by impact of adjacent Si surfaces[258] or tribological wear of contacting surfaces.[259] Taken holistically, the existing literature on polysilicon microdevices under shock loading suggests that they are rarely limited by

fracture of the polysilicon, but rather by other practical limitations of the design.

VI. DISCUSSION

It is clear from the foregoing that the materials science and engineering of strong micro- and nano-scale SCS and polysilicon components is reasonably mature. Early measurements focused on simply measuring the strength of microfabricated specimens, largely replicating macro-scale tensile testing methods at small scales (e.g., Fig. 7). Progress in device fabrication, some complicated (e.g., Figs. 9 and 13), some simple (e.g., Figs. 10–12), has enabled strengths to be measured under tension, compression, bending, and torsion. In many cases, dedicated devices have enabled the determination of large strength distributions containing hundreds (e.g., Fig. 14) to thousands (e.g., Figs. 16, 19, and 22) of samples. A major focus in determining such distributions has been to refine fabrication methods so as to achieve large strengths: The success of this endeavor may be judged by the fact that microfabricated SCS and polysilicon components now routinely exhibit strengths of several GPa and SiNWs approach the theoretical strength of Si of about 20 GPa. Dedicated specimens, along with the use of FEA and DIC methods, have enabled the fundamental elastic and fracture properties of Si (e.g., Fig. 2) to be determined, providing the basis for fracture mechanics analyses of such strengths and the nature of the processing-induced ten-nanometer-scale strength-controlling flaws (e.g., Fig. 6). To place the strength in perspective, consider a MEMS tensile component, 30×30 μm^2 in cross-section, with a strength at the small end of the MEMS range of 1 GPa. The *force* the component can sustain is about 1 N or about a 100 g mass in the earth's gravitational field. If the mass were a Si block, the block would have sides of length about 3.5 cm! Clearly such a component is capable of generating useful mechanical work as part of a MEMS device. In particular, a significant fraction of the load-carrying capability of such strong components can then be used to overcome the friction inherent in the mechanisms and linkages of complex MEMS devices such as the microdrive of Fig. 1. The question to be asked then is: "How, quantitatively, can the ability to measure and control the strength of micro- and nano-scale Si components be used to improve the reliability of MEMS devices?"

The ability to measure σ_f for a large number of samples enables the σ_f distribution for a given set of conditions to be determined with great precision. If the same set of conditions is used in the fabrication of components of MEMS devices, then the strength distribution of the components is known with similar precision and can be used by MEMS designers to optimize component mechanical reliability—the ability of a component to support a required load over a specified lifetime. In designing for component reliability, knowledge of the variation of load applied to the component with time t is required, and, in particular, the variation with time of the maximum load and thus the maximum stress experienced by the component. Comparison of this maximum experienced stress σ_{max} with the threshold strength σ_{th} of the component strength distribution leads to a choice in designing for

reliability that depends on the flexibility in selecting the geometry of the MEMS component. If the geometry of the MEMS component can be selected such that the maximum load leads to the maximum experienced stress never exceeding the threshold strength, that is $\sigma_{max} < \sigma_{th}$ over the desired lifetime of the component, then the component will never fail and the reliability is then deterministic. In this case, the details of the variation in applied stress with time and the details of the component strength distribution do not matter and MEMS design attention focuses on the *processing-structure-property* relations associated with setting the required σ_{th}. If, however, the geometry of the MEMS component cannot be varied to satisfy $\sigma_{max} < \sigma_{th}$, then there is a likelihood that some components will fail prior to the desired lifetime, and the reliability is then probabilistic. In this case, the variation of the maximum stress with time $\sigma_{max}(t)$ is convoluted with the variation of the cumulative failure probability $P_f(\sigma_f)$ to generate the component reliability $R(t) = 1 - P_f(t)$, and as a result, MEMS design attention focuses on the *property-performance* linkages associated with predicting $\sigma_{max}(t)$, $P_f(\sigma_f)$, m, σ_θ, and σ_{th}. The discussion here will provide example answers to the question above for these two design choices, focusing on processing-structure-property relationships and property-performance predictions.

A. Processing-structure-property relationships

As shown above, variations in *processing* conditions leads to different Si surface *structures*, which in turn leads to different Si strength *properties*. Such variations are highlighted in Fig. 28, which shows a graph of measured fracture strength of SCS and polysilicon as a function of the approximate stressed surface area A_s for many of the sample and loading geometries (e.g., uniaxial tension, equibiaxial tension, bending) and surface processing methods (e.g., grown, mechanical contact, wet etch, dry etch) discussed earlier. Two clear trends are apparent in Fig. 28: (i) Fracture strengths tend to decrease with increased surface area, independent of processing method, consistent with the *engineering* principle that fabrication methods tend to scale surface roughness, and therefore strength-limiting defect sizes, with component size and (ii) fracture strengths tend to decrease with increased surface area, with a different dependence for a given processing method, consistent with the *physics* principle that processing methods tend to generate a particular distribution of flaw potency, and that the probability of a component containing a more potent defect increases with component size. The dashed lines on Fig. 28 indicate trend (ii) for selected processing conditions. An implication of Fig. 28 is that if processing method and surface area are invariant, then strength should not be altered by sample or component geometry.

For SCS, there appears to be three distinct regions in Fig. 28(a), largely defined by the component size and the processing condition. In the nano-scale region, σ_f ranges from ≈5 to 18 GPa and demonstrates the expected size dependence and eventual convergence to the theoretical strength for SCS of 21–23 GPa at small A_s.[201,202] Together with the toughness of SCS, this σ_f range translates to critical flaw sizes on the order of a few to tens of nm (Eq. (18) and
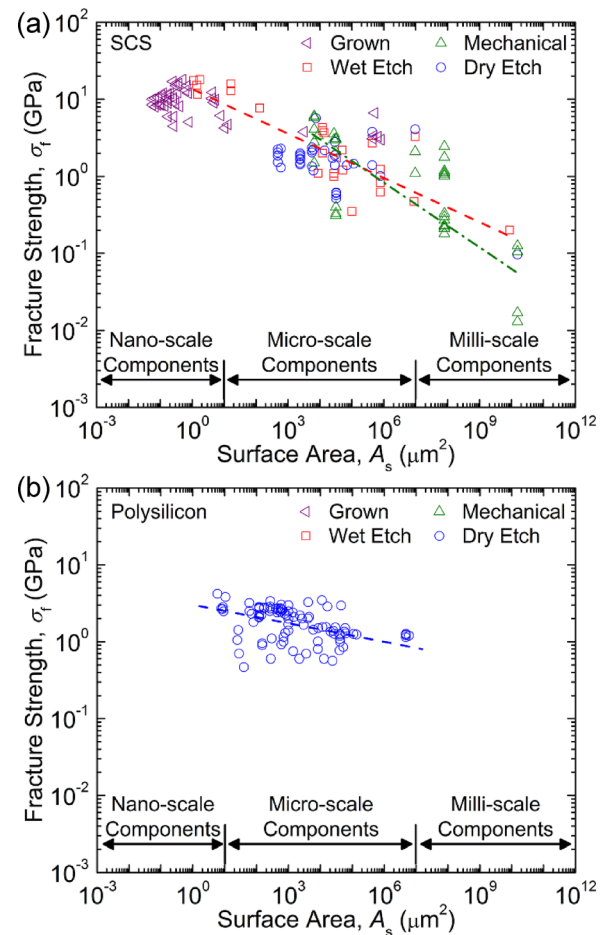

FIG. 28. Fracture strength as a function of approximate stressed surface area for (a) SCS and (b) polysilicon. Data were collected from a large number of sources in this review for both SCS and polysilicon. Power law trend lines are shown to highlight the overall behavior of the strength data.

Fig. 6). It is clear from Fig. 28(a) that such small flaw sizes are only possible with growth techniques such as VLS and wet etch processes such as TMAH, as these processing conditions are known to grow or etch Si along particular crystallographic planes, often limiting the surface flaws to *intrinsic* planar defects in the Si such as stacking faults and twin boundaries.[181] In the micro-scale region, σ_f ranges from ≈0.5 to 5 GPa, which translates to critical flaw sizes on the order of tens to hundreds of nm. The methods used to create these components are not limited to growth and wet etch processes; in fact, the larger component size often requires a different class of processing conditions (e.g., dry etch and mechanical contact), as they provide the much faster etch rates required for MEMS fabrication. As shown earlier, the techniques used to fabricate SCS microdevices are inextricably linked to the failure process, in large part because they create *extrinsic* residual surface features that act as stress concentrations and initiation sites for fracture and failure. In the milli-scale regime, σ_f ranges from ≈0.01 to 2 GPa, which translates to critical flaw sizes on the order of hundreds to thousands of nm. Because of their size, these components often cannot utilize microelectronics-based fabrication methods, and therefore rely solely on macro-scale mechanical contact methods (e.g., polishing, lapping, and sawing).

As with SCS, σ_f for polysilicon in the micro-scale region ranges from ≈ 0.5 to 5 GPa as shown in Fig. 28(b), which again translates to critical flaw sizes on the order of tens to hundreds of nm. Moreover, the methods used to fabricate polysilicon microdevices are also linked to their failure process, again because they leave *extrinsic* residual surface features. The size and location of the residual surface features is highly dependent on the polysilicon deposition and etching conditions; for SUMMiT V polysilicon, fractography reveals crack initiation sites on the sidewalls or edges (corners),[226] whereas for PolyMUMPs polysilicon, results suggested the largest flaws resided on the top (or bottom) surfaces.[133] Unlike SCS, the σ_f data for polysilicon are (i) primarily confined to the micro-scale region and (ii) solely derived from dry etch processing conditions. On the first point, polysilicon components typically have in-plane dimensions on the order of a few to hundreds of μm and out-of-plane dimensions on the order of a few μm,[117] thereby restricting the A_s values to between 10^1 and 10^7 μm^2. Moreover, the σ_f values are also limited, as polysilicon has been shown to have a reduced apparent strength relative to SCS due to elastic anisotropy of neighboring grains and pronounced stress singularities at grain boundaries and triple junctions,[233–235] which prohibits σ_f close to the theoretical limit for Si. On the second point, polysilicon can be etched with many of the same wet etchants as SCS, in many instances, with faster etch rates.[260] Despite this fact, the etch processes for polysilicon are largely dominated by dry methods such as RIE, and in some cases, DRIE.

Traditionally, MEMS manufacturing has focused on *fabricability* of intended features with sufficiently low residual stresses so that the desired geometry is attained. Mechanical reliability considerations have been secondary, if considered at all. However, Fig. 28 makes clear that MEMS manufacturers thus have considerable choice in selecting a *processing* method for MEMS components that determines the nature of the strength-controlling *structures* on the component surfaces, which then in turn determines the *properties* of the components in terms of a strength distribution. This choice, coupled with test specimens capable of statistically relevant numbers of strength measurements, enables σ_{th} to be "designed-in" to a component, thereby enabling quantitative deterministic device reliability. Moreover, there is an opportunity for MEMS foundries to track mechanical performance and specifically the strength distribution in the process. The strength distributions can be tracked with respect to spatial correlations (e.g., center vs. edge of wafer), and across process history (e.g., wafer-to-wafer and lot-to-lot). This rich statistical dataset will allow an even more robust understanding of reliability.

B. Property-performance relationships

A technologically important goal of materials engineering is to establish the linkage between material *properties* and the *performance* of components formed from that material. If the maximum stress $\sigma_{max}(t)$ is known throughout the manufacturing or operational period and the σ_f distribution (the property) is well-characterized, it is possible to predict

the manufacturing yield and operational reliability (the performance) of a group of MEMS components. Gaither *et al.* demonstrated this process using both explicit and stochastic stress spectra,[86] in conjunction with the strength distribution from SCS theta specimens formed with large scallops (Fig. 14). For brevity, only the approach based on the explicit loading scheme will be demonstrated here. In this approach, the spectrum $\sigma_{max}(t)$ was described with a simple power-law function

$$\sigma_{max}(t) = \sigma_T (t/t_T)^n. \tag{43}$$

σ_{max} increases from zero at the start of the time period $t = 0$ to a maximum value σ_T at the end of the time period $t = t_T$ with a dependence determined by the exponent n. The values assumed were $\sigma_T = 3$ GPa, $t_T = 3$ yr, and $n = 0.2, 1$, and 5 for concave, linear, and convex variations of σ_{max} with t, respectively. Generating the reliability prediction was then a simple matter of replacing σ_f with $\sigma_{max}(t)$ in Eq. (37) and combining Eqs. (37) and (43) as a parametric set to generate $P_f(t)$. Figure 29 is a plot of reliability predictions for a group of components containing the large scallop surface finish using the stress variation parameters above. Figure 29(a) shows
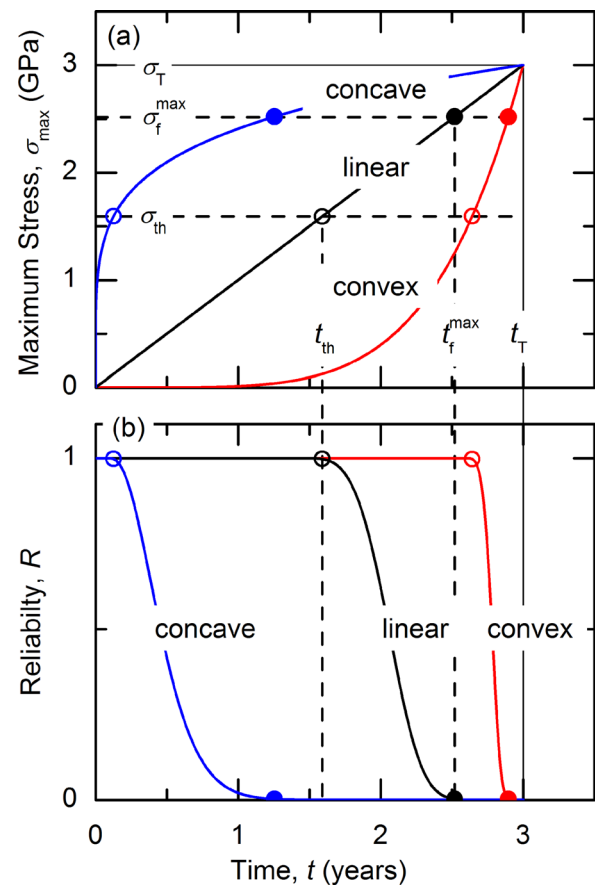

FIG. 29. Reliability prediction simulations for different applied stress functions as a function of time. (a) Concave, linear, and convex relationships for applied stress as a function of time, assuming an applied stress of 0–3 GPa over 3 years. The open and closed circles indicate the time at which the applied stress reaches the threshold strength and the maximum failure stress, respectively. (b) Reliability curves as a function of time for each of the three applied stress curves in (a). Reprinted with permission from Gaither *et al.*, J. Microelectromech. Syst. **22**, 589 (2013). Copyright 2013 IEEE.

$\sigma_{max}(t)$ and Fig. 29(b) shows $R(t)$. Consider first the linear ($n = 1$) variation of $\sigma_{max}(t)$: σ_{max} increases linearly from zero until at time $t = t_{th}$ the condition $\sigma_{max} = \sigma_{th}$ is reached, indicated by the open symbols on the plots. Prior to this time no components in the group fail, indicated by a reliability of 1. At time $t = t_f^{max}$, the condition $\sigma_{max} = \sigma_f^{max}$ is reached, indicated by the solid symbols on the plots, where σ_f^{max} is the maximum failure strength in the strength distribution. The time t_f^{max} is the lifetime of the longest surviving component, and by this time all components have failed, as indicated by a reliability of 0. For intermediate times, $t_{th} < t < t_f^{max}$, the reliability decreases from 1 to 0, and this decrease is seen to be the mirror image of the strength distribution of Fig. 14. For the convex ($n = 5$) variation of $\sigma_{max}(t)$, the initial period for which no components fail is greater than for the linear variation because the time is greater for the condition $\sigma_{max} = \sigma_{th}$ to be reached, again indicated by the open symbol. However, the increase in σ_{max} with t from this condition is more rapid than for the linear case such that the decrease in reliability takes place more rapidly until all of the components have failed, again indicated by the solid symbols. The concave ($n = 0.2$) variation of $\sigma_{max}(t)$ displays the opposite variation from linear than the convex: The initial period for which no components fail is very short and the subsequent decrease in reliability takes place more slowly. In all cases, the reliability variation with time is seen to include an initial period with no failures until the maximum stress experienced reaches the threshold strength, followed by a decrease in reliability that is a variably deformed mirror image of the strength distribution; in the cases here, the maximum applied stress was taken to be greater than the maximum failure strength, leading to a final stage in which all components had failed.

Figure 29 makes clear that MEMS manufacturers have a powerful tool in using the *property* of the MEMS material strength distribution to predict the *performance* of MEMS components in terms of the reliability spectrum. This tool, coupled with knowledge of the applied stress spectrum, enables $R(t)$ to be known for a group of components, including the important time to first fail and time to last fail, thereby enabling quantitative probabilistic device reliability.

Finally, an engineering approach that enables either deterministic or limited probabilistic device reliability is that of proof testing. The concept of proof testing is relatively straight-forward: Prior to operation, a component is subjected to service-like conditions at an applied stress state of σ_{proof}. If a group of components is exposed to σ_{proof}, those with strengths less than σ_{proof} will fail and those with strengths greater than σ_{proof} will survive. The strength distribution of the surviving group of components will then have an engineered threshold of $\sigma_{th} = \sigma_{proof}$. Hence, if σ_{proof} is greater than the upper bound of $\sigma_{max}(t)$, no component will fail in service, barring any unforeseen mechanical, thermal, or environmental anomalies, and the reliability is deterministic. If σ_{proof} is less than the upper bound of $\sigma_{max}(t)$, and $\sigma_{max}(t)$ is known, then at least the time to first fail is known. If the original manufactured σ_f strength distribution is not well characterized, say, due to small strength data set, proof testing provides a means of establishing a firm lower bound
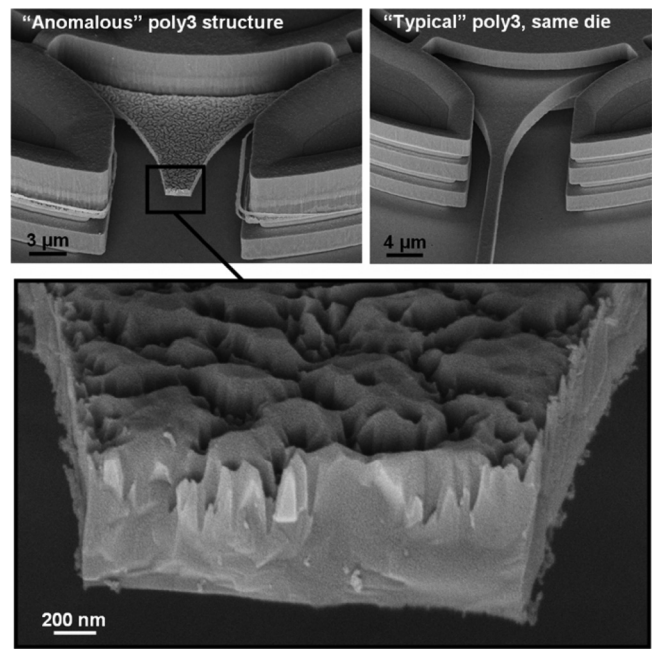

FIG. 30. SEM images of an anomalous defect morphology in a SUMMiT V polysilicon component. This unusual defect was found in only one region of a single die. The "anomalous" specimen exhibited a fracture strength <0.05 GPa, whereas the characteristic strength from a "typical" collection of tensile specimens was 2.35 GPa. Reprinted with permission from Boyce *et al.*, J. Micromech. Microeng. **18**, 117001 (2008). Copyright 2008 IOP Publishing.

to σ_{th}. The proof testing process can also be used to eliminate defective components that are not part of the main strength distribution. Boyce *et al.* discussed the merits of proof testing as it relates to micro- and nanoscale Si components, using an example from a SUMMiT V polysilicon run to illustrate its potential usefulness.[261] In this example, one particular polysilicon tensile bar possessed extensive crevice-like features that penetrated roughly half way through the tensile bar, as shown in Fig. 30. These flaws, which were not present on the other nearby polysilicon layers, nor on the same poly3 layer elsewhere in the die, were thought to be due to uncontrolled grain-boundary attack. The resulting strength of this tensile bar was <0.05 GPa, compared to the nominal characteristic strength of 2.35 GPa found in other poly3 samples on this and other die. The possibility that anomalously defected structures can and have been formed under standard processing conditions suggests that process monitoring alone is insufficient to detect all off-nominal products and hence post-fabrication proof testing is the only path to guarantee reliable performance. A simple proof test at 1 GPa would have been enough to eliminate such an irregularity. Similar remarks can be made regarding the "unintended" etch that occurred during the fabrication of the theta specimens by Gaither *et al.*[153] Boyce *et al.*, however, note several precautions that should be considered if proof testing is to be applied to MEMS components:[261] (i) proof testing loading conditions should match in-service loading conditions, (ii) proof testing environments should be at least as aggressive as the worst case in-service environments, and (iii) proof testing may not be feasible for all component

designs. Nevertheless, although adding another manufacturing step, proof testing provides MEMS manufacturers with a method to bypass *processing-structure* dependencies and directly engineer strength *properties* for optimized device *performance*.

VII. CONCLUSIONS AND OUTLOOK

A conclusion to be drawn from this review is that research regarding the fracture strength of micro- and nanoscale Si components is extensive and coherent. Typical measured strengths of 1–5 GPa are well described by a fracture mechanics framework that points to crack initiation as the likely cause of failure of Si MEMS components. Distributions of strength about these mean values are seen to arise from component to component variability in the size, and to a lesser extent geometry, of the crack-initiating, strength-controlling flaws. The fracture mechanics framework is well anchored in the large number of experimental measurements of Si Young's modulus (about 165 GPa) and toughness (about 0.8 MPa m$^{1/2}$) that are in agreement with elastic and crystallographic considerations. Validation of the combined fracture measurements and analyses is provided by direct observations of component surface morphology that are in agreement with inferred flaw sizes (tens of nanometers). These established processing-structure-properties linkages for Si strength provide a firm basis for predictions of MEMS component performance and reliability. Hence, based on these conclusions, and the diminishing research activity illustrated in Figure 2, one may come to the false additional conclusion that the topic of Si MEMS strength and reliability is fully mature. However, while admittedly there is a significantly broader mastery of Si MEMS reliability that has developed over the past three decades, there are still a number of topics ripe for further advancement. Throughout this review, a number of discrepancies and knowledge gaps have been mentioned. Below, a few of the most significant opportunities for advancement are recapitulated.

A. Optimized microstructures

Most of the focus in MEMS process development has focused on fabricating geometrically precise structures with limited residual stress. There has been much less focus on developing MEMS processes that are designed to generate superior structural and mechanically reliable components. In most engineering fields, the materials of choice have been optimized to large extent and opportunities for further improvement are incremental. However, in Si MEMS it is fully conceivable that improvements in processing could lead to significant increases in strength, control of flaw populations, and tightening of strength distributions. For example, amorphous Si may offer twice the strength of polysilicon, presumably by eliminating grain boundary grooves.[262] By the same token, replacing the common KOH etch process with an alternative etchant can improve the average strength by 25%–100%.[125,174] Most of these published opportunities focus on methods that smooth the surface topography. However, it is not inconceivable that additional toughening could be imparted to Si microstructures. As a point of

inspiration, silicon carbide MEMS materials have demonstrated toughness values that are approximately three times greater than that of Si, and the toughness of hydrogen-free tetrahedral amorphous carbon is six times greater than that of Si.[263,264] While these are unfair comparisons due to intrinsic differences in bonding, it is possible that toughening strategies analogous to zirconia-toughened alumina could one day be developed for Si MEMS.

B. Harsh environments

In current applications that involve elevated temperatures or shock loading, the Si MEMS device itself rarely limits designs. For this reason, there are relatively few studies that have explored in detail the mechanisms governing mechanical reliability of Si MEMS under elevated temperatures or shock loading. For example, there is still no mechanistic explanation for why the strength of Si MEMS evolves significantly over the first few months after release,[176] and likewise controversy persists over the role of humidity on the fatigue strength. Yet there are already device packaging and application scenarios in which Si MEMS are challenged to survive sustained temperatures or dynamic loading or both. When either SCS or polysilicon is heated up above ≈800 °C in inert environments or vacuum, heterogeneous pitting turns devices such as chevron thermal actuators into "crumbs" within a manner of hours, yet again the precise mechanism for this process is not clear.[265] While the mechanisms at play in shock environments would seem to be less controversial, the reality is that there have been exceedingly few detailed studies to confirm the predictability of dynamic transient effects.

C. Standardized principles for property measurements and safe design

It may be unrealistic to expect that an ASTM International standard for toughness evaluation of MEMS materials could be written with sufficient breadth to cover all of the possible techniques and their proper application under the various constraints of different fabrication processes. However, a document such as the current review lays the groundwork by highlighting the weaknesses and pitfalls of some methods. Even within a given standardized MPW process, there is currently little commitment to standardized methods for tracking the die-to-die, wafer-to-wafer, and lot-to-lot mechanical reliability of MEMS Si components. Quality control instead typically focuses on more rudimentary metrics such as dimensional tolerances. In the production of metals and alloys, hundreds and even thousands of tensile bars are routinely tested every day to monitor process evolution over time and certify minimum allowable properties. While a case is made in this review for the collection of sufficient statistical populations to accurately determine a three-parameter Weibull distribution, these data eventually need to be collected as a matter of routine, standardized production practice. If a Si MEMS process can certify its minimum allowable threshold strength, this value will be a powerful tool in the safe design of mechanical devices.

ACKNOWLEDGMENTS

APPENDIX: ELASTIC PROPERTIES ANALYSIS AND REVIEW

This appendix provides (i) analyses underpinning the SCS and polysilicon moduli quoted in the text and (ii) a review of the published literature on modulus measurements using small-scale Si components, for comparison with predictions from these analyses. The SCS analysis and review are presented first, followed by those for polysilicon.

1. Crystallographic effects on SCS elastic moduli

The three independent values in the elastic compliance matrix[8] for cubic SCS are $s_{11} = 7.68$ TPa^{-1}, $s_{12} = -2.14$ TPa^{-1}, and $s_{44} = 12.56$ TPa^{-1}.[9–12] The variation of Young's modulus, E, and Poisson's ratio, ν, with orientation in the $(\bar{1}10)$ plane is given by the two related equations[1,8,266,267]

$$E(m) = E_{[110]}[1 + SE_{[110]}m^2(3m^2/2 - 1)]^{-1} \quad \text{(A1)}$$

and

$$\nu(m) = \left[\nu_{[110]} \frac{E}{E_{[110]}} + 3SEm^2(m^2 - 1)/2 \right], \quad \text{(A2)}$$

where m is the direction cosine relative to [001], $S = (s_{11} - s_{12} - s_{44}/2)$, $E_{[110]} = 1/(s_{11} - S/2) = 169$ GPa and $\nu_{[110]} = -E_{[110]}s_{12} = 0.362$ are the Young's modulus and Poisson's ratio in the [110] direction, respectively; the Poisson's ratio is for transverse and normal strains parallel to the $(\bar{1}10)$ plane. These variations are shown in Fig. 5. Variations in ν are more extreme for transverse strains taken perpendicular to the $(\bar{1}10)$ plane, decreasing to 0.063 in $\langle 110 \rangle$ directions in the (001) plane.[266] A very wide bar or beam lying in the [110] direction in the (001) plane placed in tension or bending will deform with plane-strain modulus, $E_{[110]}/(1 - \nu_{[110]}^2) = 194$ GPa if the majority of the deformation is constrained to the $(\bar{1}10)$ plane; if this is not the case and the bar or beam is narrow, the plane stress modulus, $E_{[110]} = 169$ GPa pertains.

As shown by Brantley, some planes of importance exhibit no orientation variation in elastic constants.[267] For example, E and ν are invariant in {111} planes: $E_{(111)} = \text{E}_{[110]}$ and $\nu_{(111)} = \nu_{[110]}$, given in terms of the s_{ij}

above. This has the consequence that a narrow bar or beam lying in the (111) plane tested in tension or bending will exhibit an invariant (plane stress) elastic modulus $E_{(111)}$, independent of orientation about the [111] direction. Similarly, a wide bar or beam lying in the (111) plane will exhibit an invariant (plane strain) modulus $E_{(111)}/(1 - \nu_{(111)}^2)$ and an invariant (biaxial) modulus $E_{(111)}/(1 - \nu_{(111)})$, appropriate to a (111) plate placed in equibiaxial flexure. This latter condition is also true for the {100} planes, in which the biaxial modulus $E/(1 - \nu)|_{\{100\}} = 181$ GPa is invariant as a consequence of the perfectly countervailing changes in $E_{(100)}$ and $\nu_{(100)}$ with orientation, observed partially for $E_{(110)}$ and $\nu_{(110)}$ in Figs. 5(a) and 5(b). This observation is crucial to the lack of anticlastic deformation resulting from equibiaxial loading of conventional (001) SCS wafers during semiconductor and MEMS fabrication.

The relative uncertainties in the s_{ij} values above, all determined by ultrasonic wave velocity measurements, range from (0.25% to 0.05%) to 0.02%,[9–12] which are comparable to the differences observed between different studies, suggesting that the elastic constants E and ν calculated from them have relative uncertainties of less than 1%. The temperature coefficients for relative change in the s_{ij} values at room temperature are all of order -70 ppm K^{-1},[9,10] suggesting that under most MEMS and microelectronics operating conditions the relative changes in E and ν due to changes in temperature (± 75 K from room temperature) will be at most 2%. The stress or pressure coefficients for relative change in the s_{ij} values at atmospheric pressure all are of order $+10$ ppm MPa^{-1},[11,12] suggesting that under most MEMS and microelectronics operating conditions the relative changes in E and ν due to changes in stress (± 1 GPa from atmospheric pressure) will be at most 1%. The doping coefficient for relative changes in the s_{ij} values from those of pure SCS are all of magnitude 200 ppm (μmol/mol)$^{-1}$,[12] suggesting that for most MEMS and microelectronics materials the relative changes in E and ν due to doping (10 μmol/mol, heavy doping) will be less than 1%. These thermal, mechanical, and chemical variations suggest that the elastic properties given above can all be taken as stated to be within about 2% in considerations of SCS deformation and fracture.

2. SCS elastic moduli measurements

Early measurements of elastic moduli on MEMS-like devices produced mixed results: measurements of flexure resonance frequencies of narrow [100] fixed-fixed beams gave moduli of 130–133 GPa (cf. 130 GPa above),[268–270] but measurements of pull-in voltages for electrostatically actuated, wide [100] and [110] fixed-fixed and fixed-free (cantilever) beams gave 138 ± 4 GPa and 168 ± 6 GPa, respectively (cf. 140 GPa and 194 GPa), and electrostatically actuated biaxial flexure of a (100) diaphragm gave 155 GPa (cf. 181 GPa).[271] Subsequent micro- and nano-scale structures, specifically constructed for static mechanical testing, have provided measurements of Young's modulus and Poisson's ratio in substantial agreement with the predictions above, mostly for bars in tension, as shown in Table II. Recent measurements by Banks-Sills *et al.*, using specially

TABLE II. Elastic constants of SCS.

Prediction	Measurement	Test method	Reference
$E_{[100]} = 130$ GPa	138 ± 11 GPa	Tension	275
	142 ± 9 GPa	Tension	138
	123 ± 8 GPa	Tension	89
	131.4 ± 2.1 GPa	Tension	158
$E_{[110]} = 169$ GPa	140 ± 25 GPa	Tension	275
	166 ± 8 GPa	Tension	89
	169.2 ± 3.5 GPa	Tension	125
	170 ± 5 GPa	Bending	172
	169 GPa	Tension	279
	171.9 ± 4.2 GPa	Tension	13
$E_{[111]} = 187$ GPa	180 ± 20 GPa	Tension	275
$\nu_{(110)[100]} = 0.279$	0.23 ± 0.03	Tension	158
$\nu_{(110)[110]} = 0.362$	0.35	Tension	279
$\nu_{(001)[110]} = 0.063$	0.068	Custom	272

designed specimens and direct measurements of strain by interferometry, give values of the elastic constants with very small uncertainties.[13,158] Use of a specially designed rectangular specimen and direct measurements of deformation by interferometry have recently provided a (001)[110] Poisson's ratio of 0.068 (cf. 0.063 above).[272] Although not direct measurements of modulus, measurements of [110] cantilever stiffness using variable loading points to take beam attachment location uncertainty into account yield values in bending[169,273,274] and torsion[274] consistent with the s_{ij} values above. Finally, using Ref. 275 geometry for bars in [110] tension, measurements as a function of temperature (in the absence of plasticity) provided a decrease of 2% at 300 °C from the room temperature value,[60] in agreement with the assessment above.

3. Microstructural effects on polysilicon elastic moduli

The (111) predictions above have the consequence that a dense polysilicon film formed with [111] crystallographic texture, i.e., all the grain [111] directions are oriented in same direction, might occur in a columnar grain structure on a substrate, is nearly elastically transversely isotropic. Such a film has an out-of-plane modulus of 187 GPa, an in-plane modulus of 169 GPa, and another independent elastic constant, to make three in all, fewer than the maximum of five required for such elastic symmetry.[8] The number of independent elastic constants is further reduced to two if the film or component has a random, uniform, three-dimensional distribution of grain orientations and is therefore elastically isotropic.[276,277] The two independent isotropic elastic constants are calculated from bounds determined from the three independent cubic elastic constants re-expressed as the bulk modulus

$$K = \frac{1}{3(s_{11} + 2s_{12})}, \qquad (A3)$$

and the two single-crystal shear moduli

$$G_1 = \frac{1}{2(s_{11} - s_{12})} \quad \text{and} \quad G_2 = \frac{1}{s_{44}}. \qquad (A4)$$

Polycrystalline shear modulus bounds based on minimizing the elastic strain energy or complementary strain energy of the solid are more restrictive[277] than the commonly used uniform stress or strain bounds[276] and are given by

$$G_1^* = G_1 + 3\left(\frac{5}{G_2 - G_1} - 4\beta_1\right)^{-1} \quad \text{and}$$

$$G_2^* = G_2 + 2\left(\frac{5}{G_1 - G_2} - 6\beta_2\right)^{-1}, \qquad (A5)$$

where

$$\beta_i = \frac{-3(K + 2G_i)}{5G_i(3K + 4G_i)}. \qquad (A6)$$

The polycrystalline Young's modulus and Poisson's ratio bounds are then given by

$$E_i^* = \frac{9KG_i^*}{3K + G_i^*} \qquad (A7)$$

and

$$\nu_i^* = \frac{3K - 2G_i^*}{6K + 2G_i^*}. \qquad (A8)$$

The means of these bounds provide estimates of the elastic constants of the isotropic polycrystal, $E_{(\text{poly})} = 163$ GPa and $\nu_{(\text{poly})} = 0.223$, and these are shown as the circular dashed

TABLE III. Elastic constants of polysilicon.

Prediction	Measurement	Test method	Reference
$\bar{E}_{(110)} = 165$ GPa	164 ± 25 GPa	Tension	121
	151 ± 5 GPa	Biaxial flexure	4
	158 ± 3 GPa	Ultrasonic wave	
	170 ± 6.7 GPa	Tension	124
	136 ± 14 GPa	Tension	280
	174 ± 25 GPa	Bending	
	142 ± 25 GPa	Tension	280
	137 ± 5 GPa	Bending	
	162 ± 14 GPa	Tension	129
	172 ± 7 GPa	Tension	138
	160 ± 4 GPa	Tension	137
	160 ± 30 GPa	Pull-in voltage	
	162 ± 4 GPa	Biaxial flexure	5
	158 ± 10 GPa	Tension	130
	165 ± 6 GPa	Tension	14 and 278
	155.6 ± 6.6 GPa	Strain mapping	
$E_{(\text{poly})} = 163$ GPa	175 ± 15 GPa	Tension	121
	163, 167 GPa	Tension	127
	164 ± 1.2 GPa	Tension	157
	164.3 ± 4.3 GPa	Bending	6
	175 ± 60 GPa	Tension	140
	155 ± 6 GPa	Tension	14
	156.3 ± 2.6 GPa	Tension	281
$\bar{\nu}_{(110)} = 0.24$	0.22 ± 0.01	Tension	124
$\nu_{(\text{poly})} = 0.22$	0.20 ± 0.03	Biaxial flexure	5
	0.254 ± 0.0125	Custom	282
	0.22 ± 0.01	Tension	278
	0.20 ± 0.04	Strain mapping	
	0.22 ± 0.02	Tension	14

lines in Fig. 5; the relative separation of the bounds is less than 1%. Intermediate between the nearly ideal transverse isotropy of the [111] texture and the complete isotropy of the random polycrystal is the behavior of a [110] textured film consisting of a large number of grains with a uniform distribution of orientations about the common [110] direction. In this case, the film exhibits effective elastic transverse isotropy, with an out-of-plane modulus $E_{[110]} = 169$ GPa and in-plane modulus and Poisson's ratio given by the angular averages of the variations shown in Figs. 5(a) and 5(b): $\bar{E}_{(110)} = 165$ GPa and $\bar{\nu}_{(110)} = 0.24$.

4. Polysilicon elastic moduli measurements

Modulus measurements of polysilicon structures formed from [110] textured films are in agreement with the above predictions, as shown in Table III. As with SCS, the measurements are mostly for bars in tension, although there are a few more confirmatory tests using other geometries. Measurements of modulus on random or unspecified texture polysilicon are similar. Measurements of Poisson's ratio on polysilicon, although less frequent, are also in agreement with the above predictions. Analytically and experimentally, there is little distinction between textured and random structures. In common with SCS, the most recent measurements by Cho *et al.*, using specially designed specimens and direct measurements of strain by DIC, give values of the elastic constants with very small uncertainties.[14,278]

[1]R. F. Cook, J. Mater. Sci. **41**, 841 (2006); there are typographical errors in Eqs. (1) and (2).
[2]K. E. Petersen, Proc. IEEE **70**, 420 (1982).
[3]A. Kelly and G. W. Groves, *Crystallography and Crystal Defects* (Longman, London, 1970).
[4]D. Maier-Schneider, A. Köprülülü, S. B. Holm, and E. Obermeier, J. Micromech. Microeng. **6**, 436 (1996).
[5]S. Jayaraman, R. L. Edwards, and K. J. Hemker, J. Mater. Res. **14**, 688 (1999).
[6]B. D. Jensen, M. P. de Boer, N. D. Masters, F. Bitsie, and D. A. LaVan, J. Microelectromech. Syst. **10**, 336 (2001).
[7]M. T. Dugger, B. L. Boyce, T. E. Buchheit, and S. V. Prasad, Technical Report No. SAND2004-1319, Sandia National Laboratories, Albuquerque, NM, 2004.
[8]J. F. Nye, *Physical Properties of Crystals* (Oxford, Oxford, 1957).
[9]H. J. McSkimin, W. L. Bond, E. Buehler, and G. K. Teal, Phys. Rev. **83**, 1080 (1951).
[10]H. J. McSkimin, J. Appl. Phys. **24**, 988 (1953).
[11]H. J. McSkimin and P. Andreatch, J. Appl. Phys. **35**, 2161 (1964).
[12]J. J. Hall, Phys. Rev. **161**, 756 (1967).
[13]L. Banks-Sills, J. Shklovsky, S. Krylov, H. A. Bruck, V. Fourman, R. Eliasi, and D. Ashkenazi, Strain **47**, 288 (2011).
[14]S. W. Cho and I. Chasiotis, Exp. Mech. **47**, 37 (2007).
[15]W. D. Harkins, J. Chem. Phys. **10**, 268 (1942).
[16]G. A. Wolff and J. D. Broder, Acta Crystallogr. **12**, 313 (1959).
[17]J. Emsley, *The Elements* (Clarendon Press, Oxford, 1989).
[18]B. R. Lawn, B. J. Hockey, and S. M. Wiederhorn, J. Mater. Sci. **15**, 1207 (1980).
[19]B. P. Lemke and D. Haneman, Phys. Rev. B **17**, 1893 (1978).
[20]D. Haneman, N. S. McAlpine, E. Busch, and C. Kaalund, Appl. Surf. Sci. **92**, 484 (1996).
[21]P. J. Hesketh, C. Ju, S. Gowda, E. Zanoria, and S. Danyluk, J. Electrochem. Soc. **140**, 1080 (1993).
[22]D. R. Clarke, in *Semiconductors and Semimetals*, edited by K. T. Faber and K. Malloy (Academic Press, Waltham, 1992), pp. 79–142.
[23]J. E. Sinclair and B. R. Lawn, Proc. R. Soc. London, Ser. A **329**, 83 (1972).
[24]M. Tanaka, K. Higashida, H. Nakashima, H. Takagi, and M. Fujiwara, Mater. Trans. **44**, 681 (2003).
[25]T. Mizuguchi, K.-I. Ikeda, F. Yoshida, H. Nakashima, and H. Abe, J. Jpn. Inst. Mater. **68**, 86 (2004).
[26]B. R. Lawn, *Fracture of Brittle Solids*, 2nd ed. (Cambridge University Press, Cambridge, 1993).
[27]G. R. Irwin, in *Handbuch der Physik*, edited by S. Flügge (Springer-Verlag, Berlin-Heidelberg, 1958), Vol. 6, pp. 551–590.
[28]G. C. Sih, P. C. Paris, and G. R. Irwin, Int. J. Fract. Mech. **1**, 189 (1965).
[29]J. B. Wachtman, Jr., in *Fracture Mechanics of Ceramics*, edited by R. C. Bradt, D. P. H. Hasselman, and F. F. Lange (Plenum Press, New York, 1974), Vol. 1, pp. 49–68.
[30]R. Pérez and P. Gumbsch, Phys. Rev. Lett. **84**, 5347 (2000).
[31]R. Ballarini, R. L. Mullen, and A. H. Heuer, Int. J. Fract. **95**, 19 (1999).
[32]J. Chen and Y. Qiao, Scr. Mater. **57**, 1069 (2007).
[33]Y. Qiao and J. Chen, Scr. Mater. **59**, 251 (2008).
[34]J. J. Gilman, J. Appl. Phys. **31**, 2208 (1960).
[35]R. J. Jaccodine, J. Electrochem. Soc. **110**, 524 (1963).
[36]C. St. John, Philos. Mag. **32**, 1193 (1975).
[37]M. Brede and P. Haasen, Acta Metall. **36**, 2003 (1988).
[38]C. P. Chen and M. H. Leipold, in *Fracture Mechanics of Ceramics*, edited by R. C. Bradt, A. G. Evans, D. P. H. Hasselman, and F. F. Lange (Plenum Press, New York, 1986), Vol. 8, pp. 285–297.
[39]S. B. Bhaduri and F. F. Y. Wang, J. Mater. Sci. **21**, 2489 (1986); there is a typographical error in Eq. (21).
[40]E. Anastassakis, A. Pinczuk, E. Burstein, F. H. Pollak, and M. Cardona, Solid State Commun. **8**, 133 (1970).
[41]A. G. Haerle, W. R. Cannon, and M. Denda, J. Am. Ceram. Soc. **74**, 2897 (1991).
[42]F. Haubensak and A. S. Argon, J. Mater. Sci. **32**, 1473 (1997).
[43]J. A. Connally and S. B. Brown, Science **256**, 1537 (1992).
[44]J. A. Connally and S. B. Brown, Exp. Mech. **33**, 81 (1993).
[45]Y.-B. Xin and K. J. Hsia, Acta Mater. **44**, 845 (1996).
[46]H. Kahn, N. Tayebi, R. Ballarini, R. L. Mullen, and A. H. Heuer, Sens. Actuators, A **82**, 274 (2000).
[47]H. Kahn, R. Ballarini, J. J. Bellante, and A. H. Heuer, Science **298**, 1215 (2002).
[48]I. Chasiotis, S. W. Cho, and K. Jonnalagada, J. Appl. Mech. **73**, 714 (2006).
[49]S. W. Cho, K. Jonnalagada, and I. Chasiotis, Fatigue Fract. Eng. Mater. Struct. **30**, 21 (2007).
[50]R. F. Cook and E. G. Liniger, J. Mater. Sci. **27**, 4751 (1992).
[51]*Stress Intensity Factors Handbook*, edited by Y. Murakami (Pergamon Press, Oxford, 1990), pp. 669, 698–700.
[52]A. M. Fitzgerald, R. H. Dauskardt, and T. W. Kenny, Sens. Actuators, A **83**, 194 (2000).
[53]A. M. Fitzgerald, R. S. Iyer, R. H. Dauskardt, and T. W. Kenny, in *Proceedings of Micro-Electro-Mechanical Systems, DSC* (ASME, Pittsburgh, 1988), Vol. 66, pp. 395–399.
[54]D. Son, J.-J. Kim, T. W. Lim, and D. Kwon, Thin Solid Films **468**, 167 (2004).
[55]X. Li, T. Kasai, S. Nakao, H. Tanaka, T. Ando, M. Shikida, and K. Sato, Sens. Actuators, A **119**, 229 (2005).
[56]X. Li, T. Kasai, S. Nakao, T. Ando, M. Shikida, K. Sato, and H. Tanaka, Sens. Actuators, A **117**, 143 (2005).
[57]X. Li, T. Kasai, S. Nakao, T. Ando, M. Shikida, and K. Sato, Fatigue Fract. Eng. Mater. Struct. **30**, 1172 (2007).
[58]T. Ando, X. Li, S. Nakao, T. Kasai, H. Tanaka, M. Shikida, and K. Sato, Fatigue Fract. Eng. Mater. Struct. **28**, 687 (2005).
[59]S. Nakao, T. Ando, M. Shikida, and K. Sato, J. Micromech. Microeng. **18**, 015026 (2008).
[60]S. Nakao, T. Ando, M. Shikida, and K. Sato, J. Micromech. Microeng. **16**, 715 (2006).
[61]R. N. Jaya and V. Jayaram, Int. J. Fract. **188**, 213 (2014).
[62]R. Ballarini, R. L. Mullen, Y. Yin, H. Kahn, S. Stemmer, and A. H. Heuer, J. Mater. Res. **12**, 915 (1997).
[63]R. C. Brodie and D. F. Bahr, Mater. Sci. Eng., A **351**, 166 (2003).
[64]A. Corigliano, A. Ghisi, G. Langfelder, A. Longoni, F. Zaraga, and A. Merassi, Eur. J. Mech. A Solids **30**, 127 (2011).
[65]J. E. Bradby, J. S. Williams, J. Wong-Leung, M. V. Swain, and P. Munroe, J. Mater. Res. **16**, 1500 (2001).
[66]R. F. Cook and G. M. Pharr, J. Am. Ceram. Soc. **73**, 787 (1990).
[67]G. R. Anstis, P. Chantikul, B. R. Lawn, and D. B. Marshall, J. Am. Ceram. Soc. **64**, 533 (1981).

[68] R. F. Cook, Y. B. Gerbig, J. Schoenmaker, and S. J. Stranick, in *12th International Conference on Fracture Conference Proceedings* (Curran Associates, Red Hook, 2009), pp. 3578–3587.

[69] B. Wong and R. J. Holbrook, J. Electrochem. Soc. **134**, 2254 (1987).

[70] F. Ericson, S. Johansson, and J.-Å. Schweitz, Mater. Sci. Eng., A **105**/**106**, 131 (1988).

[71] F. Ebrahimi and L. Kalwani, Mater. Sci. Eng., A **268**, 116 (1999).

[72] R. W. Fancher, C. M. Watkins, M. G. Norton, D. F. Bahaar, and E. W. Osborne, J. Mater. Sci. **36**, 5441 (2001).

[73] J. G. Swadener and M. Nastasi, J. Mater. Sci. Lett. **21**, 1363 (2002).

[74] C. P. Chen and M. H. Leipold, Jr., Am. Ceram. Soc. Bull. **59**, 469 (1980).

[75] C. P. Chen, M. H. Leipold, Jr., and D. Helmreich, Commun. Am. Ceram. Soc. **65**, C-49 (1982).

[76] K. Yasutake, M. Iwata, K. Yoshii, M. Umeno, and H. Kawabe, J. Mater. Sci. **21**, 2185 (1986).

[77] K. Hayashi, S. Tsujimoto, Y. Okamoto, and T. Nishikawa, J. Soc. Mater. Sci., Jpn. **40**, 405 (1991).

[78] K. Hayashi, S. Tsujimoto, Y. Okamoto, and T. Nishikawa, J. Soc. Mater. Sci., Jpn. **41**, 488 (1992).

[79] Y. L. Tsai and J. J. Mecholsky, Jr., J. Mater. Res. **6**, 1248 (1991).

[80] C. Mesmer and J. C. Bilello, J. Appl. Phys. **52**, 4623 (1981).

[81] R. F. Cook and D. H. Roach, J. Mater. Res. **1**, 589 (1986).

[82] Y.-G. Jung, A. Pajares, R. Banerjee, and B. R. Lawn, Acta Mater. **52**, 3459 (2004).

[83] B. L. Boyce, J. M. Grazier, T. E. Buchheit, and M. J. Shaw, J. Microelectromech. Syst. **16**, 179 (2007).

[84] E. D. Reedy, B. L. Boyce, J. W. Foulk, R. V. Field, M. P. de Boer, and S. S. Hazra, J. Microelectromech. Syst. **20**, 922 (2011).

[85] D. C. Miller, B. L. Boyce, M. T. Dugger, T. E. Bucheit, and K. Gall, Sens. Actuators, A **138**, 130 (2007).

[86] M. S. Gaither, R. S. Gates, R. Kirkpatrick, R. F. Cook, and F. W. DelRio, J. Microelectromech. Syst. **22**, 589 (2013).

[87] F. Pouramahmadi, D. Gee, and K. Petersen, in *1991 International Conference on Solid State Sensors and Actuators. Digest of Technical Papers* (IEEE, New York, 1991), pp. 197–200.

[88] W. Suwito, M. L. Dunn, and S. Cunningham, J. Appl. Phys. **83**, 3574 (1998).

[89] W. Suwito, M. L. Dunn, S. J. Cunningham, and D. T. Read, J. Appl. Phys. **85**, 3519 (1999).

[90] E. Mazza and J. Dual, J. Mech. Phys. Solids **47**, 1795 (1999).

[91] N. P. Bailey and J. P. Sethna, Phys. Rev. B **68**, 205204 (2003).

[92] J. E. Blendell and R. L. Coble, J. Am. Ceram. Soc. **65**, 174 (1982).

[93] W. Weibull, Proc. R. Swed. Inst. Eng. Res. **151**, 1 (1939).

[94] W. Weibull, Proc. R. Swed. Inst. Eng. Res. **153**, 1 (1939).

[95] F. T. Pierce, J. Text. Inst. **17**, T355 (1926).

[96] W. Weibull, J. Appl. Mech. **18**, 293 (1951).

[97] M. T. Todinov, Mater. Sci. Eng., A **276**, 39 (2000).

[98] J.-L. Le, Z. P. Bažant, and M. Z. Bazant, J. Mech. Phys. Solids **59**, 1291 (2011).

[99] R. L. Barnett, C. L. Connors, P. C. Hermann, and J. R. Wingfield, U. S. Air Force Flight Dynamics Laboratory, Report No. AFFDL-TR-66-220, Wright Patterson Air Force Base, OH, 1967.

[100] A. M. Freudenthal, in *Fracture, An Advanced Treatise*, Mathematical Fundamentals Vol. 2, edited by H. Liebowitz (Academic Press, New York, 1968).

[101] S. B. Batdorf and J. G. Crose, J. Appl. Mech. **41**, 459 (1974).

[102] S. B. Batdorf and H. L. Heinisch, J. Am. Ceram. Soc. **61**, 355 (1978).

[103] N. N. Nemeth, J. M. Manderscheid, and J. P. Gyekenyesi, Am. Ceram. Soc. Bull. **68**, 2064 (1989).

[104] L. R. Swank and R. M. Williams, Am. Ceram. Soc. Bull. **60**, 830 (1981).

[105] O. M. Jadaan, N. N. Nemeth, J. Bagdahn, and W. N. Sharpe, J. Mater. Sci. **38**, 4087 (2003).

[106] M. A. Haque and M. T. A. Saif, Exp. Mech. **43**, 248 (2003).

[107] K. J. Hemker and W. N. Sharpe, Annu. Rev. Mater. Res. **37**, 93 (2007).

[108] M. F. Pantano, H. D. Espinosa, and L. Pagnotta, J. Mech. Sci. Technol. **26**, 545 (2012).

[109] A. Cowen, G. Hames, D. Monk, S. Wilcenski, and B. Hardy, *SOIMUMPs Design Handbook: Revision 8.0* (MEMSCAP, Durham, 2011).

[110] A. Cowen, B. Hardy, R. Mahadevan, and S. Wilcenski, *PolyMUMPs Design Handbook: Revision 13.0* (MEMSCAP, Durham, 2011).

[111] F. W. DelRio, M. P. de Boer, J. A. Knapp, E. D. Reedy, P. J. Clews, and M. L. Dunn, Nat. Mater. **4**, 629 (2005).

[112] F. W. DelRio, M. L. Dunn, B. L. Boyce, A. D. Corwin, and M. P. de Boer, J. Appl. Phys. **99**, 104304 (2006).

[113] F. W. DelRio, M. L. Dunn, L. M. Phinney, C. J. Bourdon, and M. P. de Boer, Appl. Phys. Lett. **90**, 163104 (2007).

[114] F. W. DelRio, M. L. Dunn, and M. P. de Boer, Scr. Mater. **59**, 916 (2008).

[115] M. P. de Boer, D. L. Luck, W. R. Ashurst, R. Maboudian, A. D. Corwin, J. A. Walraven, and J. R. Redmond, J. Microelectromech. Syst. **13**, 63 (2004).

[116] A. D. Corwin and M. P. de Boer, Appl. Phys. Lett. **84**, 2451 (2004).

[117] J. J. Sniegowski and M. P. de Boer, Annu. Rev. Mater. Sci. **30**, 299 (2000).

[118] A. Corigliano, L. Domenella, and G. Langfelder, Exp. Mech. **50**, 695 (2010).

[119] R. L. Eisner, Acta Metall. **3**, 414 (1955).

[120] W. D. Sylwestrowicz, Philos. Mag. **7**, 1825 (1962).

[121] J. Koskinen, J. E. Steinwall, R. Soave, and H. H. Johnson, J. Micromech. Microeng. **3**, 13 (1993).

[122] M. Biebl and H. von Phillipsborn, in *Proceedings of the Eighth International Conference on Solid-State Sensors and Actuators* (1995), p. 72.

[123] D. T. Read and J. C. Marshall, Proc. SPIE **2880**, 56 (1996).

[124] W. N. Sharpe, B. Yuan, and R. L. Edwards, J. Microelectromech. Syst. **6**, 193 (1997).

[125] T. Yi, L. Li, and C.-J. Kim, Sens. Actuators, A **83**, 172 (2000).

[126] D. T. Read, J. Test. Eval. **26**, 255 (1998).

[127] T. Tsuchiya, O. Tabata, J. Sakata, and Y. Taga, J. Microelectromech. Syst. **7**, 106 (1998).

[128] T. Tsuchiya, Fatigue Fract. Eng. Mater. Struct. **28**, 665 (2005).

[129] W. N. Sharpe, K. T. Turner, and R. L. Edwards, Exp. Mech. **39**, 162 (1999).

[130] W. N. Sharpe, K. M. Jackson, K. J. Hemker, and Z. L. Xie, J. Microelectromech. Syst. **10**, 317 (2001).

[131] J. Bagdahn, W. N. Sharpe, and O. Jadaan, J. Microelectromech. Syst. **12**, 302 (2003).

[132] I. Chasiotis and W. G. Knauss, Exp. Mech. **42**, 51 (2002).

[133] I. Chasiotis and W. G. Knauss, J. Mech. Phys. Solids **51**, 1533 (2003).

[134] I. Chasiotis and W. G. Knauss, J. Mech. Phys. Solids **51**, 1551 (2003).

[135] A. McCarty and I. Chasiotis, Thin Solid Films **515**, 3267 (2007).

[136] S. Greek, F. Ericson, S. Johansson, and J.-A. Schweitz, Thin Solid Films **292**, 247 (1997).

[137] S. Greek, F. Ericson, S. Johansson, M. Fürtsch, and A. Rump, J. Micromech. Microeng. **9**, 245 (1999).

[138] J.-A. Schweitz and F. Ericson, Sens. Actuators, A **74**, 126 (1999).

[139] D. A. LaVan and T. E. Buchheit, Proc. SPIE **3880**, 40 (1999).

[140] T. E. Buchheit, S. J. Glass, J. R. Sullivan, S. S. Mani, D. A. LaVan, T. A. Friedmann, and R. Janek, J. Mater. Sci. **38**, 4081 (2003).

[141] B. L. Boyce, M. J. Shaw, P. Lu, and M. T. Dugger, Acta Mater. **58**, 439 (2010).

[142] B. L. Boyce, Exp. Mech. **50**, 993 (2010).

[143] S. S. Hazra, M. S. Baker, J. L. Beuth, and M. P. de Boer, J. Micromech. Microeng. **19**, 082001 (2009).

[144] S. S. Hazra, M. S. Baker, J. L. Beuth, and M. P. de Boer, J. Microelectromech. Syst. **20**, 1043 (2011).

[145] G. A. Myers, S. S. Hazra, M. P. de Boer, C. A. Michaels, S. J. Stranick, R. P. Koseski, R. F. Cook, and F. W. DelRio, Appl. Phys. Lett. **104**, 191908 (2014).

[146] S. Gravier, M. Coulombier, A. Safi, N. Andre, A. Boe, J.-P. Raskin, and T. Pardoen, J. Microelectromech. Syst. **18**, 555 (2009).

[147] F. Urena, S. H. Olsen, L. Siller, U. Bhaskar, T. Pardoen, and J.-P. Raskin, J. Appl. Phys. **112**, 114506 (2012).

[148] G. D. Quinn, E. Fuller, D. Xiang, A. Jillavenkatesa, L. Ma, D. Smith, and J. Beall, Ceram. Eng. Sci. Proc. **26**, 117 (2005).

[149] G. D. Quinn, Ceram. Eng. Sci. Proc. **29**, 189 (2009).

[150] A. J. Durelli, S. Morse, and V. Parks, Mater. Res. Stand. **2**, 114 (1962).

[151] E. R. Fuller, D. L. Henann, and L. Ma, Int. J. Mater. Res. **98**, 729 (2007).

[152] M. S. Gaither, F. W. DelRio, R. S. Gates, E. R. Fuller, and R. F. Cook, Scr. Mater. **63**, 422 (2010).

[153] M. S. Gaither, F. W. DelRio, R. S. Gates, and R. F. Cook, J. Mater. Res. **26**, 2575 (2011).

[154] F. W. DelRio, L. H. Friedman, M. S. Gaither, W. A. Osborn, and R. F. Cook, J. Appl. Phys. **114**, 113506 (2013).

[155] Y. Zhu and H. D. Espinosa, Proc. Natl. Acad. Sci. U. S. A. **102**, 14503 (2005).

[156] Y. Zhu, F. Xu, Q. Qin, W. Y. Fung, and W. Lu, Nano Lett. **9**, 3934 (2009).

[157]J. N. Ding, Y. G. Meng, and S. Z. Wen, J. Mater. Res. **16**, 2223 (2001).

[158]L. Banks-Sills, Y. Hikri, S. Krylov, V. Fourman, Y. Gerson, and H. A. Bruck, Sens. Actuators, A **169**, 98 (2011).

[159]K. S. Chen, A. Ayon, and S. M. Spearing, J. Am. Ceram. Soc. **83**, 1476 (2000).

[160]K. S. Chen, A. Ayon, X. Zhang, and S. M. Spearing, J. Microelectromech. Syst. **11**, 264 (2002).

[161]B. Moser, K. Wasmer, L. Barbieri, and J. Michler, J. Mater. Res. **22**, 1004 (2007).

[162]R. Rabe, J.-M. Breguet, P. Schwaller, S. Stauss, F.-J. Haug, J. Patscheider, and J. Michler, Thin Solid Films **469–470**, 206 (2004).

[163]F. Östlund, K. Rzepiejewska-Malyska, K. Leifer, L. M. Hale, Y. Tang, R. Ballarini, W. W. Gerberich, and J. Michler, Adv. Funct. Mater. **19**, 2439 (2009).

[164]K. Wasmer, T. Wermelinger, A. Bidiville, R. Spolenak, and J. Michler, J. Mater. Res. **23**, 3040 (2008).

[165]B. Li, M. K. Kang, K. Lu, R. Huang, P. S. Ho, R. A. Allen, and M. W. Cresswell, Nano Lett. **8**, 92 (2008).

[166]T. P. Weihs, S. Hong, J. C. Bravman, and W. D. Nix, J. Mater. Res. **3**, 931 (1988).

[167]S. Johansson, J.-A. Schweitz, L. Tenerz, and J. Tiren, J. Appl. Phys. **63**, 4799 (1988).

[168]F. Ericson and J.-A. Schweitz, J. Appl. Phys. **68**, 5840 (1990).

[169]C. J. Wilson, A. Ormeggi, and M. Narbutovskih, J. Appl. Phys. **79**, 2386 (1996).

[170]C. J. Wilson and P. A. Beck, J. Microelectromech. Syst. **5**, 142 (1996).

[171]P. T. Jones, G. C. Johnson, and R. T. Howe, Proc. SPIE **3880**, 20 (1999).

[172]T. Namazu, Y. Isono, and T. Tanaka, J. Microelectromech. Syst. **9**, 450 (2000).

[173]S. Sundararajan, B. Bhushan, T. Namazu, and Y. Isono, Ultramicroscopy **91**, 111 (2002).

[174]T. Alan, M. A. Hines, and A. T. Zehnder, Appl. Phys. Lett. **89**, 091901 (2006).

[175]T. Alan and A. T. Zehnder, Int. J. Fract. **148**, 129 (2007).

[176]T. Alan, A. T. Zehnder, D. Sengupta, and M. A. Hines, Appl. Phys. Lett. **89**, 231905 (2006).

[177]R. Kirkpatrick, W. A. Osborn, M. S. Gaither, R. S. Gates, F. W. DelRio, and R. F. Cook, MRS Commun. **3**, 113 (2013).

[178]M. Tabib-Azar, M. Nassirou, R. Wang, S. Sharma, T. I. Kamins, M. S. Islam, and R. S. Williams, Appl. Phys. Lett. **87**, 113102 (2005).

[179]S. Hoffmann, I. Utke, B. Moser, J. Michler, S. H. Christiansen, V. Schmidt, S. Senz, P. Werner, U. Gosele, and C. Ballif, Nano Lett. **6**, 622 (2006).

[180]D.-M. Tang, C.-L. Ren, M.-S. Wang, X. Wei, N. Kawamoto, C. Liu, Y. Bando, M. Mitome, N. Fukata, and D. Golberg, Nano Lett. **12**, 1898 (2012).

[181]G. Stan, S. Krylyuk, A. V. Davydov, I. Levin, and R. F. Cook, Nano Lett. **12**, 2599 (2012).

[182]G. Stan, S. Krylyuk, A. V. Davydov, and R. F. Cook, Nano Lett. **10**, 2031 (2010).

[183]G. Stan, S. Krylyuk, A. V. Davydov, and R. F. Cook, J. Mater. Res. **27**, 562 (2012).

[184]M. T. A. Saif and N. C. MacDonald, in *Proceedings of the Ninth Annual International Workshop on Micro Electro Mechanical Systems* (1996), p. 105.

[185]M. T. A. Saif and N. C. MacDonald, Rev. Sci. Instrum. **69**, 1410 (1998).

[186]Z. L. Zhang and N. C. MacDonald, J. Microelectromech. Syst. **2**, 66 (1993).

[187]K. A. Shaw, Z. L. Zhang, and N. C. MacDonald, Sens. Actuators, A **40**, 63 (1994).

[188]G. Schiltges and J. Dual, J. Mech. Phys. Solids **49**, 1021 (2001).

[189]F. F. Meroni and E. Mazza, Microsyst. Technol. **10**, 412 (2004).

[190]S. M. Hu, J. Appl. Phys. **53**, 3576 (1982).

[191]J. C. McLaughlin and A. F. W. Willoughby, J. Cryst. Growth **85**, 83 (1987).

[192]J. Vedde and P. Gravesen, Mater. Sci. Eng., B **36**, 246 (1996).

[193]S.-M. Jeong, S.-E. Park, H.-S. Oh, and H. L. Lee, J. Ceram. Process. Res. **5**, 171 (2004).

[194]S. Michaelides and S. K. Sitaraman, IEEE Trans. Adv. Packag. **22**, 602 (1999).

[195]B. Cotterel, Z. Chen, J.-B. Han, and N. X. Tan, J. Electron. Packag. **125**, 114 (2003).

[196]N. McLellan, N. Fan, S. Liu, K. Lau, and J. Wu, J. Electron. Packag. **126**, 110 (2004).

[197]T. Namazu, Y. Isono, and T. Tanaka, J. Microelectromech. Syst. **11**, 125 (2002).

[198]G. L. Pearson, W. T. Read, and W. L. Feldmann, Acta Metall. **5**, 181 (1957).

[199]S. Johansson, F. Ericson, and J.-A. Schweitz, J. Appl. Phys. **65**, 122 (1989).

[200]D. C. Miller, B. L. Boyce, P. G. Kotula, and C. R. Stoldt, J. Appl. Phys. **103**, 123518 (2008).

[201]S.-M. Dubois, G.-M. Rignanese, T. Pardoen, and J.-C. Charlier, Phys. Rev. B **74**, 235203 (2006).

[202]D. Roundy and M. L. Cohen, Phys. Rev. B **64**, 212103 (2001).

[203]U. Bhaskar, V. Passi, S. Houri, E. Escobedo-Cousin, S. H. Olsen, T. Pardoen, and J. P. Raskin, J. Mater. Res. **27**, 571 (2012).

[204]M. L. Dunn, W. Suwito, S. J. Cunningham, and C. W. May, Int. J. Solids Struct. **34**, 3873 (1997).

[205]A. Mehra, A. A. Ayon, I. A. Waitz, and M. A. Schmidt, J. Microelectromech. Syst. **8**, 152 (1999).

[206]M. Suster, W. H. Ko, and D. J. Young, J. Microelectromech. Syst. **13**, 536 (2004).

[207]P. Hirsch and S. Roberts, Philos. Mag. A **64**, 55 (1991).

[208]M. Brede, Acta Metall. Mater. **41**, 211 (1993).

[209]J. Fruhauf, E. Gartner, and E. Jansch, J. Micromech. Microeng. **9**, 305 (1999).

[210]J. Fruhauf, E. Gartner, and E. Jansch, Appl. Phys. A **68**, 673 (1999).

[211]J. Castaing, P. Veyssiere, L. P. Kubin, and J. Rabier, Philos. Mag. A **44**, 1407 (1981).

[212]T.-H. Chang and Y. Zhu, Appl. Phys. Lett. **103**, 263114 (2013).

[213]U. Neuwald, H. E. Hessel, A. Feltz, U. Memmert, and R. J. Behm, Appl. Phys. Lett. **60**, 1307 (1992).

[214]D. H. Alsem, O. N. Pierron, E. A. Stach, C. L. Muhlstein, and R. O. Ritchie, Adv. Eng. Mater. **9**, 15 (2007).

[215]K. Komai, K. Minoshima, and S. Inoue, Microsyst. Technol. **5**, 30 (1998).

[216]K. Minoshima, T. Terada, and K. Komai, Fatigue Fract. Eng. Mater. Struct. **23**, 1033 (2000).

[217]O. N. Pierron and C. L. Muhlstein, J. Microelectromech. Syst. **15**, 111 (2006).

[218]A. M. Lomonosov and P. Hess, Phys. Rev. Lett. **89**, 095501 (2002).

[219]G. Lehmann, A. M. Lomonosov, P. Hess, and P. Gumbsch, J. Appl. Phys. **94**, 2907 (2003).

[220]G. Sharon, R. Oberc, and D. Barker, Int. J. Struct. Integr. **4**, 191 (2013).

[221]P. V. McAllister and I. B. Cutler, J. Am. Ceram. Soc. **55**, 351 (1972).

[222]W. M. Robertson, J. Am. Ceram. Soc. **64**, 9 (1981).

[223]D. C. Miller, C. R. Becker, and C. R. Stoldt, J. Electrochem. Soc. **155**, F253 (2008).

[224]O. N. Pierron, D. D. Macdonald, and C. L. Muhlstein, Appl. Phys. Lett. **86**, 211919 (2005).

[225]D. H. Alsem, B. L. Boyce, E. A. Stach, and R. O. Ritchie, Sens. Actuators, A **147**, 553 (2008).

[226]E. D. Reedy, B. L. Boyce, J. W. Foulk, R. V. Field, J. A. Ohlhausen, M. P. de Boer, and S. S. Hazra, Technical Report No. SAND2010-6701, Sandia National Laboratories, Albuquerque, NM, 2010.

[227]L. B.-B. Bergman and D. Sherman, Scr. Mater. **75**, 14 (2014).

[228]M. B. Zbib and D. F. Bahr, Metall. Mater. Trans. E **1**, 20 (2014).

[229]D. J. Green, R. H. J. Hannink, and M. V. Swain, *Transformation Toughening of Ceramics* (CRC Press, Boca Raton, 1989).

[230]S. J. Bennison and B. R. Lawn, Acta Metall. **37**, 2659 (1989).

[231]J. W. Foulk, G. C. Johnson, P. A. Klein, and R. O. Ritchie, J. Mech. Phys. Solids **56**, 2381 (2008).

[232]D. A. LaVan, T. Tsuchiya, G. Coles, W. G. Knauss, I. Chasiotis, and D. T. Read, ASTM Spec. Tech. Publ. **1413**, 16 (2001).

[233]V. Tvergaard and J. W. Hutchinson, J. Am. Ceram. Soc. **71**, 157 (1988).

[234]P. V. Galptshyan, in *Polycrystalline Materials—Theoretical and Practical Aspects*, edited by Z. Zakhariev (InTech, Croatia, 2012).

[235]E. Reedy, J. Appl. Mech. **78**, 014502 (2011).

[236]R. Boroch, J. Wiaranowski, R. Mueller-Fiedler, M. Ebert, and J. Bagdahn, Fatigue Fract. Eng. Mater. Struct. **30**, 2 (2007).

[237]S. Kamiya, Y. Ikeda, J. Gaspar, and O. Paul, Sens. Actuators, A **170**, 187 (2011).

[238]S. Nakao, T. Ando, S. Arai, N. Saito, and K. Sato, "Microelectromechanical Systems - Materials and Devices" (Mater. Res. Soc. Symp. Proc., 2008), Vol. 1052, p. DD03-21.

[239]H. Kahn, R. Ballarini, and A. Heuer, Curr. Opin. Solid State Mater. Sci. **8**, 71 (2004).

[240]D. H. Alsem, R. Timmerman, B. L. Boyce, E. A. Stach, J. T. M. De Hosson, and R. O. Ritchie, J. Appl. Phys. **101**, 13515 (2007).

[241]O. N. Pierron and C. L. Muhlstein, J. Microelectromech. Syst. **16**, 1441 (2007).

[242]T. Tanemura, S. Yamashita, H. Wado, Y. Takeuchi, T. Tsuchiya, and O. Tabata, J. Micromech. Microeng. **23**, 035032 (2013).

[243]H. Kahn, A. Avishai, R. Ballarini, and A. H. Heuer, Scr. Mater. **59**, 912 (2008).

[244]V. Hatty, H. Kahn, and A. H. Heuer, J. Microelectromech. Syst. **17**, 943 (2008).

[245]T. A. Michalske and S. W. Freiman, J. Am. Ceram. Soc. **66**, 284 (1983).

[246]J. Tsuchiya, A. Inoue, and J. Sakata, Sens. Actuators, A **82**, 286 (2000).

[247]D. Alsem, E. Stach, C. Muhlstein, and R. Ritchie, Appl. Phys. Lett. **86**, 041914 (2005).

[248]M. Hon, F. W. DelRio, J. T. White, M. Kendig, C. Carraro, and R. Maboudian, Sens. Actuators, A **145**, 323 (2008).

[249]F. Liu, C. S. Roper, J. Chu, C. Carraro, and R. Maboudian, Sens. Actuators, A **166**, 201 (2011).

[250]L. Michelutti, N. Mathieu, A. Chovet, and A. Galerie, Miroelectron. Reliab. **40**, 179 (2000).

[251]A. Corigliano, F. Cacchione, A. Frangi, and S. Zerbini, Sens. Lett. **6**, 35 (2008).

[252]S. Mariani, A. Ghisi, A. Corigliano, and S. Zerbini, Sensors **9**, 556 (2009).

[253]V. T. Srikar and S. D. Senturia, J. Microelectromech. Syst. **11**, 206 (2002).

[254]A. Ghisi, S. Kalicinski, S. Mariani, I. De Wolf, and A. Corigliano, J. Micromech. Microeng. **19**, 035023 (2009).

[255]G. Li and F. Shemansky, Sens. Actuators, A **85**, 280 (2000).

[256]T. G. Brown, B. Davis, D. Hepner, J. Faust, C. Myers, C. Muller, T. Harkins, M. Holis, and B. Placzankis, IEEE Trans. Magn. **37**, 336 (2001).

[257]D. M. Tanner, J. A. Walraven, K. Helgesen, L. W. Irwin, F. Brown, N. F. Smith, and N. Masters, in *Proceedings of the IEEE International Reliability Physics* (2000), p. 129.

[258]J. A. Walraven, in *Proceedings of the IEEE International Test* (2003), p. 828.

[259]D. Alsem, E. Stach, M. Dugger, M. Enachescu, and R. Ritchie, Thin Solid Films **515**, 3259 (2007).

[260]G. T. A. Kovacs, *Micromachined Transducers Sourcebook* (WCB McGraw-Hill, Boston, 1998).

[261]B. L. Boyce, R. Ballarini, and I. Chasiotis, J. Micromech. Microeng. **18**, 117001 (2008).

[262]H. Kahn, N. Tayebi, R. Ballarini, R. L. Mullen, and A. H. Heuer, "Materials Science of Microelectromechanical Systems Devices II" (Mater. Res. Soc. Symp. Proc., 2000), Vol. 605, p. 25.

[263]J. J. Bellante, H. Kahn, R. Ballarini, C. A. Zorman, M. Mehregany, and A. H. Heuer, Appl. Phys. Lett. **86**, 071920 (2005).

[264]H. D. Espinosa, B. Peng, N. Moldovan, T. A. Friedmann, X. Xiao, D. C. Mancini, O. Auciello, J. Carlisle, C. A. Zorman, and M. Merhegany, Appl. Phys. Lett. **89**, 073111 (2006).

[265]M. S. Baker, R. A. Plass, T. J. Headley, and J. A. Walraven, Technical Report No. SAND2004-6635, Sandia National Laboratories, Albuquerque, NM, 2004.

[266]J. J. Wortman and R. A. Evans, J. Appl. Phys. **36**, 153 (1965).

[267]W. A. Brantley, J. Appl. Phys. **44**, 534 (1973).

[268]L. M. Zhang, D. Uttamchandani, B. Culshaw, and P. Dobson, Meas. Sci. Technol. **1**, 1343 (1990).

[269]L. M. Zhang, D. Uttamchandani, and B. Culshaw, Sens. Actuators, A **21**, 391 (1990).

[270]L. M. Zhang, D. Uttamchandani, and B. Culshaw, Sens. Actuators, A **29**, 79 (1991).

[271]P. M. Osterberg and S. D. Senturia, J. Microelectromech. Syst. **6**, 107 (1997).

[272]T. Namazu, T. Fujii, and M. Takahashi, J. Microelectromech. Syst. **22**, 625 (2013).

[273]Z. C. Ying, M. G. Reitsma, and R. S. Gates, Rev. Sci. Instrum. **78**, 063708 (2007).

[274]M. G. Reitsma, R. S. Gates, L. H. Friedman, and R. F. Cook, Rev. Sci. Instrum. **82**, 093706 (2011).

[275]K. Sato, T. Yoshioka, T. Ando, M. Shikida, and T. Kawabata, Sens. Actuators, A **70**, 148 (1998).

[276]R. Hill, Proc. Phys. Soc. A **65**, 349 (1952).

[277]Z. Hashin and S. Shtrikman, J. Mech. Phys. Solids **10**, 343 (1962).

[278]S. Cho, J. F. Cárdenas-García, and I. Chasiotis, Sens. Actuators, A **120**, 163 (2005).

[279]T. Namazu and S. Inoue, Fatigue Fract. Eng. Mater. **30**, 13 (2007).

[280]W. N. Sharpe, S. Brown, G. C. Johnson, and W. Knauss, in *Microelectromechanical Structures for Materials Research*, edited by S. Brown, J. Gilbert, H. Guckel, R. Howe, G. Johnson, P. Krulevitch, and C. Muhlstein (Materials Research Society, Warrendale, 1998), pp. 57–65.

[281]J. Gaspar, M. E. Schmidt, J. Held, and O. Paul, J. Microelectromech. Syst. **18**, 1062 (2009).

[282]J.-H. Kim, S.-C. Yeon, Y.-K. Jeon, J.-G. Kim, and Y.-H. Kim, Sens. Actuators, A **108**, 20 (2003).